

## THESIS / THÈSE

### DOCTOR OF SCIENCES

#### **Applications of the (3+1)-formalism of General Relativity to Cosmology A study of Hybrid Inflation and Spherical Collapse with quintessence**

Rekier, Jérémy

*Award date:*  
2015

*Awarding institution:*  
University of Namur

[Link to publication](#)

#### **General rights**

Copyright and moral rights for the publications made accessible in the public portal are retained by the authors and/or other copyright owners and it is a condition of accessing publications that users recognise and abide by the legal requirements associated with these rights.

- Users may download and print one copy of any publication from the public portal for the purpose of private study or research.
- You may not further distribute the material or use it for any profit-making activity or commercial gain
- You may freely distribute the URL identifying the publication in the public portal ?

#### **Take down policy**

If you believe that this document breaches copyright please contact us providing details, and we will remove access to the work immediately and investigate your claim.



UNIVERSITÉ DE NAMUR

FACULTÉ DES SCIENCES

DÉPARTEMENT DE MATHÉMATIQUE

# Applications of the $(3+1)$ -formalism of General Relativity to Cosmology

## A study of Hybrid Inflation and Spherical Collapse with Quintessence

Thèse présentée par  
**Jérémy Requier**  
pour l'obtention du grade  
de Docteur en Sciences

Composition du Jury:

André FÜZFA (Promoteur)  
Jean-Michel ALIMI  
Timoteo CARLETTI  
Sébastien CLESSE  
Isabel CORDERO CARRIÓN  
Eric GOURGOULHON

Septembre 2015

Graphisme de couverture : ©Presses universitaires de Namur

©Presses universitaires de Namur & Jérémy Requier  
Rempart de la Vierge, 13  
B-5000 Namur (Belgique)

Toute reproduction d'un extrait quelconque de ce livre,  
hors des limites restrictives prévues par la loi,  
par quelque procédé que ce soit, et notamment par photocopie ou scanner,  
est strictement interdite pour tous pays.

Imprimé en Belgique

ISBN : 978-2-87037-911-0  
Dépôt légal: D / 2015/ 1881/ 42

Université de Namur  
Faculté des Sciences  
rue de Bruxelles, 61, B-5000 Namur (Belgique)

**Applications du formalisme (3+1) de la relativité générale à la cosmologie**  
**Une étude de l'inflation hybride et de l'effondrement sphérique avec quintessence**  
par Jérémy Requier

**Résumé :** Ce travail traite de deux sujets de cosmologies physiques différents rassemblés par l'utilisation du formalisme (3+1) de la relativité générale et par la présence, dans les deux cas, d'un degré de liberté scalaire minimalement couplé. Dans la première partie, nous montrons comment le modèle original d'inflation hybride à large valeur du champ peut générer un large ratio des perturbations tensorielles et scalaires nous effectuons l'analyse statistique de l'espace des paramètres montrant le très bon accord possible avec les données observables. Dans la deuxième partie, nous étudions l'évolution d'un espace-temps décrivant les alentours d'une surdensité de matière sphérique et tendant asymptotiquement vers un Univers homogène et isotrope rempli d'un champ scalaire de quintessence. La méthode numérique proposée permet une étude ab initio complète du processus d'effondrement sphérique et de l'implication de la quintessence sur la formation des amas de galaxies.

**Applications of the (3+1)-formalism of General Relativity to Cosmology**  
**A study of Hybrid Inflation and Spherical Collapse with Quintessence**  
by Jérémy Requier

**Abstract:** This work deals with two different subjects of physical cosmology joined together by the usage of the (3+1) formalism of General Relativity and the presence of a minimally coupled scalar degree of freedom. In the first part, we show how the original Hybrid Inflation model in the large field regime can generate a large value of the tensor to scalar perturbations ratio and we perform the statistical analysis of the parameter space demonstrating the very good possible agreement with observable data. In the second part, we study the evolution of space-time in the surroundings of a spherical over-density of matter that asymptotically corresponds to the homogeneous and isotropic Universe filled with a quintessence scalar field. The numerical method proposed allows the complete ab initio study of the spherical collapse process and the study of the implication of quintessence on the formation of galaxy clusters.

Thèse de doctorat en Sciences Physiques (Ph.D. thesis in Physical Sciences)

Date: 17/09/2015

Département de Mathématique

Promoteur (Advisor): Pr. A. FÜZFA



# Remerciements

Je tiens à remercier mon directeur de thèse, le Pr. André Füzfa pour ce qu'il m'a appris et pour l'opportunité qu'il m'a offerte d'entreprendre cette première expérience académique.

Merci à mes collaborateurs d'avoir contribué à la qualité de ce travail et aux membres du jury pour avoir accepté de juger de sa validité.

De façon plus générale, je remercie tous les amis et les étudiants que j'ai croisés au département de mathématiques et qui ont contribué à rendre ces quatre années parmi eux souvent amusantes et toujours instructives.

Je profite de l'occasion pour adresser un énorme merci à mes parents et à la fratrie pour tout ce qu'ils sont. J'ai beaucoup de chance de les avoir eus comme équipe de soutien pendant ces années passées à l'Université.



# Contents

<b>Introduction</b>	<b>1</b>
<b>1 Review of Space-time, General Relativity and Cosmology</b>	<b>5</b>
1.1 Space-time . . . . .	5
1.2 Special Theory of Relativity . . . . .	6
1.3 General Theory of Relativity . . . . .	8
1.4 Cosmology . . . . .	9
1.5 Precision Cosmology . . . . .	11
1.6 Inflation . . . . .	12
1.7 Structure formation . . . . .	14
<b>2 (3+1) Formulation of General Relativity</b>	<b>17</b>
2.1 Splitting of space-time . . . . .	17
2.2 Dynamics of space-time . . . . .	20
2.3 Energy and momentum conservation . . . . .	22
2.4 The Friedmann equations . . . . .	23
2.5 Accelerated expansion . . . . .	24
2.6 Cosmological scalar field . . . . .	25
2.7 Acceleration with a scalar field . . . . .	26
2.8 Numerical treatment . . . . .	27
2.9 The BSSN formulation . . . . .	28
<b>3 Large Field Hybrid Inflation</b>	<b>31</b>
3.1 Inflationary perturbation . . . . .	31
3.1.1 ADM action . . . . .	32
3.1.2 Constraint equations . . . . .	32
3.1.3 Fixing a gauge . . . . .	33
3.1.4 Perturbative action . . . . .	33
3.1.5 Scalar perturbations . . . . .	34
3.1.6 Tensor Perturbations . . . . .	40
3.2 Large Field Hybrid Inflation . . . . .	41
3.3 Reheating parametrisation . . . . .	43
3.4 The regimes of large field inflation . . . . .	44
3.4.1 Chaotic-like inflation: $\phi_c < \mu \ll \phi_*$ and $\mu < M_{pl}$ . . . . .	45

3.4.2	Transitory: $\phi_c < \mu \sim \phi_*$ and $\mu \sim M_{pl}$ . . . . .	47
3.4.3	Large Critical Field Value: $\mu < \phi_c < \phi_*$ . . . . .	48
3.5	The $(\phi_c, \mu)$ parameter space . . . . .	48
3.6	Statistical Analysis . . . . .	52
3.7	Conclusion . . . . .	54
<b>4</b>	<b>Cosmological Spherical Collapse</b> . . . . .	<b>59</b>
4.1	The top-hat model . . . . .	59
4.1.1	The top-hat model from Newtonian physics . . . . .	60
4.1.2	The top-hat model from General Relativity . . . . .	62
4.2	Fully Relativistic solution for spherical collapse . . . . .	67
4.2.1	General Formalism . . . . .	68
4.2.2	Boundary conditions . . . . .	70
4.2.3	Implementation . . . . .	71
4.2.4	Evolution on a de Sitter background . . . . .	72
4.2.5	Spherical collapse of dust matter . . . . .	75
4.2.6	Initial data . . . . .	79
4.2.7	Comparison with LTB . . . . .	81
4.2.8	Long time evolution . . . . .	81
4.2.9	Spherical Collapse of a scalar field . . . . .	84
4.3	Spherical collapse of matter overdensities with quintessence . . . . .	97
4.3.1	Background evolution . . . . .	97
4.3.2	The top-hat model with a scalar field . . . . .	100
4.3.3	Comparison with the top-hat . . . . .	101
4.3.4	Beyond the top-hat model . . . . .	107
4.4	Conclusion . . . . .	112
	<b>Conclusion</b> . . . . .	<b>115</b>
	<b>List of Tables</b> . . . . .	<b>118</b>
	<b>List of Figures</b> . . . . .	<b>120</b>
	<b>Appendix</b> . . . . .	<b>127</b>
	<b>A Natural units</b> . . . . .	<b>127</b>
	<b>B Operator Splitting for PIRK</b> . . . . .	<b>129</b>
	<b>C The code</b> . . . . .	<b>131</b>
	C.1 Introduction . . . . .	131
	C.2 Downloading and compiling . . . . .	131
	C.3 First run . . . . .	131
	C.4 Directory listing . . . . .	133
	C.5 Simplified project structure . . . . .	133

*CONTENTS*

C.6 Running and input parameters . . . . . 134  
C.7 Output format . . . . . 135  
C.8 Scripts and tools . . . . . 135  
C.9 Files structure . . . . . 136

**Bibliography** . . . . . **143**



# Introduction

“Gravity on me  
Never let me down  
Gently”

---

— Stuart “2D” Pot

One hundred years ago, Albert Einstein published a series of papers that would completely change our understanding of many laws of nature. His theory of general relativity would later be the framework to the study of modern cosmology with the insane-sounding project to understand our Universe as a whole. This idea first came from the very simple question of finding the adequate boundary conditions in a problem of gravitation.

Cosmology has come a long way since these times and evolved into a precision science. A great many of its prominent researchers have invented ingenious mechanisms to explain a number of loopholes in the original theory. Some are now being put to the test. Among these are the mechanisms of inflation and Dark Energy.

Simultaneously, great technical progress have been made in the task of solving Einstein equations. The evolution of numerical techniques and methods have allowed to consider physically complex solutions beyond the reach of analytical treatments. These methods are all based on a of (3+1)-splitting formalism of the 4 dimensional space-time and, while these have proved to be very efficient in a great many applications, these are most of the time employed on problems at the astrophysical scales, much smaller than the scales of cosmology.

Four years ago, we set forth to provide our own contribution to the field with the original project to study the formation of large-scale structures in various Dark Energy models hoping to eventually move on to the study of modified theories of gravity. It turned out that the flow of this project was not to evolve smoothly but was rather to take unexpected turns.

We wanted to perform structure formation in a fully relativistic way. This is not usual as most studies are performed through Newtonian perturbations around a cosmological solution. The tools we needed were still to be figured out.

One of the first ideas that we had was to investigate the way a spherically symmetric collapsing space-time can be embedded within the expanding (spa-

tially flat) cosmological background. We tried to pursue this idea by examining the kind of junction conditions valid between the Lemaître-Tolman-Bondi and Friedmann-Lemaître solutions planning to later generalise to more complex solutions for the inner space-time in order to accommodate for matter with pressure in the future. We were aiming for a way to write the dynamics of the boundary between both solutions in order to track down its evolution. This was to be a fresh new approach to the collapse problem. A couple of unforeseen difficulties arose in this research leading us to reconsider the problem from a different point of view before we could have garnered enough findings to be included in a scientific communication.

We moved on instead to consider space-time as a whole inhomogeneous cosmological solution. In presence of pressure-less matter only, the solution is the analytical Lemaître-Tolman-Bondi and the will to generalise this solution in presence of a quintessence scalar field led us to use tools of numerical relativity. The initial idea was to use our new results in conjunction with the results on the embedding of space-time into the cosmological solution. However, we moved to a complete (3+1)-decomposition along the way until we finally decided to leave the embedding problem aside for another project.

With the intention to provide only material brought to completion in this manuscript, we focus on the description of the (3+1)-approach.

The use of Numerical Relativity techniques (applied to cosmology) is ancient. Yet, the application of these in the treatment of quintessence remains seldom. In the 80's, Piran studied the impact of scalar field inhomogeneities on inflation in order to investigate whether a sufficient amount of inhomogeneities could prevent it to occur. Those studies were performed using Regge calculus (Piran 1986), then the ADM formalism (Goldwirth and Piran 1989). One early application of the BSSN formalism<sup>(1)</sup> in spherical symmetry in cosmology was studied by Shibata et al. in the context of primordial Black Holes formation (Shibata and Sasaki 1999*a*). Our personal contribution lies among the more recent works focusing on the applications of these techniques to the late-time dynamics of the Universe when matter, and subsequently quintessence dominates. Early works in this context include the study made by Llinares et al. (Llinares and Mota 2013) in which the complete dynamics of the symmetron scalar-tensor theory is studied and applied in N-Body simulations. As we were deep within our own study, another team applied the BSSN formalism to the growth of matter and scalar field perturbations on an expanding background where the scalar field is subjected to a simple massive potential (Alcubierre, de la Macorra, Diez-Tejedor and Torres 2015). This team used a method different to ours and we feel that our works are complementary.

A large part of the work performed was dedicated to the development of the numerical tools we needed. The method we used was inspired from existing works by Alcubierre (Alcubierre and Mendez 2011) and Montero & Cordero-Carrión (Montero and Cordero-Carrión 2012). The actual code used however

---

<sup>(1)</sup>A detailed account of the ADM and BSSN formalisms is given in chapter 2.

had to be written from the ground up by the author. The outcome is a very general computational framework which can serve as the stepping stone for many studies of gravitation on cosmological scales. This is written in FORTRAN90 and is intentionally made easy to use through a simplified method to process inputs and outputs. The numerical method as been described and studied in a scientific publication also featuring an application to the collapse of dust matter (Rekier, Cordero-Carrión and Füzfa 2015). The following article describing our results on the collapse in presence of quintessence is currently in preparation. The use of FORTRAN90 over other possible languages was primarily justified by our previous good experience in using this language. We have stucked with it for the core of the code while choosing PYTHON for the design of scripts for the visualisation of outputs. The code has been made public and a complete description of it is given in Appendix (?)

Our personal belief is that the (3+1) decomposition formalism has not yet shown the full extent of its interest regarding cosmology. This thesis seeks to contribute to remedy to this.

The success obtained by N-body simulations to reproduce the statistical distribution of matter observed today do preach in favour of the validity of this method, yet the exact relativistic process of the collapse of matter in the dynamical Universe is not yet understood very clearly. The analytical cosmological solutions are few outside of the class of homogeneous Friedmann-Lemaître space-times. For this reason, and most probably for its formal simplicity, the most widely employed model of gravitational collapse is the so-called “top-hat” model in which the whole space-time remains piecewise homogeneous and isotropic along the physical radius of coordinates. This has the merit to maintain a lot of intuition from Newtonian physics but lacks those of a complete relativistic treatment and is flawed by many formal inconsistencies.

When we mention the “top-hat”, we understand a certain type of model in which the energy density profile remains a step function throughout the whole evolution. The whole space-time consists only in two parts at all time and not only initially as is sometimes implied. Many works have demonstrated the simplicity and advantages of the top-hat model in the description of the formation of large structures in the matter dominated era (Gunn and Gott 1972, Peebles 1980, Padmanabhan 1993, Peacock 1999). More recent studies have attempted to apply it to the collapse in presence of a cosmological Dark Energy component (Wang and Steinhardt 1998, Voit 2005, Horellou and Berge 2005, Abramo, Batista, Liberato and Rosenfeld 2009, Fernandes, de Carvalho, Kamenshchik, Moschella and da Silva 2012, Li and Xu 2014). Some of these investigated the case where the quintessence component is a real scalar field (Mota and van de Bruck 2004, Nunes and Mota 2006, Wintergerst and Pettorino 2010). In the present work, we provide a comparison between the results of the top-hat model with quintessence to those obtained with our fully relativistic method.

Cosmology is naturally suited to use (3+1) decomposition as it deals with the time evolution of energy and gravitational field distributions. We hope that our approach will contribute to reduce the gap between the fields of numerical

relativity and cosmology.

In the making of this thesis and in parallel to the work performed on spherical collapse, we also collaborated on a project on the hybrid model of cosmological inflation. In March 2014, there was a commotion around the detection of primordial gravitational waves in the polarisation of the cosmic microwave background. While this detection has recently been strongly disfavoured by a joint analysis of BICEP2/Keck Array and Planck data (Ade et al. 2015) it revived the interest in models of inflation producing a large tensor to scalar power spectra ratio.

The work that we did in collaboration with S. Clesse led to scientific results that already found their place in one scientific publication (Clesse and Requier 2014). We feel these should also be featured in the present manuscript. However, as much as spherical collapse and inflation are both highly interesting topics of their own, it is not obvious how these could be put in a unique work without throwing a bridge between the two fields otherwise all too little linked. This missing link comes, again, from the use of the (3+1)-formalism.

In the study of cosmological perturbations during inflation, it is necessary to parametrise the perturbed metric in order to identify the relevant degrees of freedom. A formalism based on the (3+1)-decomposition was developed by Maldacena (Maldacena 2003) to achieve this purpose. In the present manuscript, we use his formalism to derive the quantities useful to our analysis of the hybrid inflation model.

The present manuscript is organised as follows. Chapter 1 is intended as a brief review of the basic concepts of this space-time and cosmology. This is voluntarily kept short as a proper detailed introduction to each of these concepts cannot be possibly provided in a thesis manuscript the principal focus of which ought to remain on its main topics. However, we feel that giving no introduction to these would be missing an enjoyable opportunity to provide our own attempt at explaining the brilliant ideas that got us interested in the field the first place. Chapter 2 is intended as a toolbox featuring all the mathematical apparatus used throughout this thesis. This includes the introduction to the (3+1)-formalism of general relativity and its implications on the cosmological solutions. Armed with these tools, we can move on to the study of the two objects of this thesis, namely large field hybrid inflation and spherical collapse. These are respectively described in chapters 3 and 4 which can be read independently of one another. The chapter on spherical collapse is by far the largest of all.

# Chapter 1

## Review of Space-time, General Relativity and Cosmology

There exists a great many good books dedicated to the subjects of space-time and relativity and we do not intent to compete with those with a mere introductory chapter. However, this work is produced under the benevolent attention of a department of applied mathematics and we feel it is natural to expose the result of our research in such a way that a person well skilled in applied mathematics yet not daily immersed in General Relativity should be able to appreciate it without having to go through all the literature.

This chapter seeks to provide the basic material needed to serve this purpose. We trust that the mathematician shall excuse us for the lack of mathematical rigour dismissed in favour of brevity.

### 1.1 Space-time

Space-time as the idea of the physical 3-dimensional *space* to which one adds an extra *time* dimension can be employed already in the context of Newtonian Dynamics. However, it takes the theory of Relativity to understand how space and time are really aspects of a more fundamental object called space-time.

The trajectory of a point particle moving along a line can be sketched on a two dimensional diagramme with one coordinate representing space and the other representing time. On such diagramme, the trajectory of a ray of light makes a 45 degrees in the units in which it travels one unit of space in one unit of time (in these units, its speed is  $c = 1$ ).

According to the Galilean invariance principle, all the frames moving at a constant velocity relative to one another are equally well suited frames of ref-

erence. These are called *inertial frames*. The relation between any two frames of reference is sketched graphically on a 2 dimensional space-time diagramme by leaving the time axis as it is and operating a rotation of the space axis by an angle

$$\tan \theta = v . \quad (1.1)$$

Such transformation implies that the speed of light is not constant in all frames and is contrary to the results of all attempts to measure a variation of the speed of light in vacuum.

## 1.2 Special Theory of Relativity

In reality, light always travels at the same speed. This must be taken as a fundamental law of nature that holds in any frame of reference and leads to the special theory of relativity.

In order to visualise the impact of this on the dynamics of moving objects on a space-time diagramme, the moving frame must be pictured by operating a rotation of the time axis equal in magnitude and opposite in sign to the rotation imposed on the space axis.

Such transformation is equivalent to operating a rotation on both axes by an imaginary angle and Eq. (1.1) is replaced by

$$\tanh \eta = v . \quad (1.2)$$

where  $\eta$  is the imaginary part of the rotation angle. The complete transformation law is

$$\begin{aligned} x &= x' \cosh \eta + t' \sinh \eta , \\ t &= x' \sinh \eta + t' \cosh \eta . \end{aligned} \quad (1.3)$$

In terms of the velocity of the moving frame, these become

$$x = \frac{x' + vt'}{\sqrt{1 - v^2}} , \quad t = \frac{t' + vx'}{\sqrt{1 - v^2}} . \quad (1.4)$$

These are known as the *Lorentz Transformations*.

Space-time is naturally equipped with a constant pseudo-Riemannian metric the components of which are deduced by inspection of the line element

$$ds^2 = -dt^2 + dl^2 , \quad (1.5)$$

where  $ds^2$  and  $dl^2$  are the squared line-element of space-time and space respectively. The latter is equivalent to the square of a small displacement within an euclidian space. The space-time line-element is invariant under the Lorentz transformations.

A point on a space-time diagramme defines a location in space at a moment in time and is called an *event*. The trajectory of a moving particle is a line

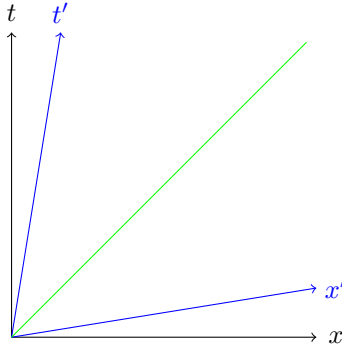


Figure 1.1 – The action of the Lorentz transformation is pictured on a space-time diagramme by a rotation by an imaginary angle with  $\tanh \eta = v$

flowing along the time direction. Such line is called a *world-line* and its shape can be inferred from its boundary events by means of a variational principle.

One of the consequences of the Lorentz transformations is that a time interval measured by a clock at rest  $d\tau$  is always inferior to the interval measured by any moving observer  $dt$ .

$$d\tau = dt\sqrt{1 - v^2} . \quad (1.6)$$

$\tau$  is called the *proper time*. As a resting frame is equivalent to a frame moving with constant velocity, the principle of least action of Lagrangian dynamics is generalised by demanding the quantity

$$\int_a^b d\tau = - \int_a^b ds , \quad (1.7)$$

to be maximal along the real path of the particle. The time  $\tau$  is called the proper “time”.

The relativistic version of the principle of least action states that the path followed between two events is the one that maximises the proper time. This can be reconciled with the principle valid in Newtonian dynamics by defining the action as

$$S = -m \int d\tau , \quad (1.8)$$

To an arbitrary observer this becomes

$$S = -m \int dt\sqrt{1 - v^2} , \quad (1.9)$$

where  $t$  and  $v$  are respectively the coordinate time for the observer and the velocity of the particle. The momentum is defined as  $\vec{p} := \frac{\partial L}{\partial \vec{v}}$  which here gives

$$\vec{p} = \frac{m\vec{v}}{\sqrt{1 - v^2}} , \quad (1.10)$$

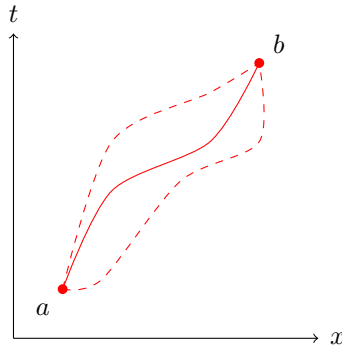


Figure 1.2 – The actual path between two events is the one that maximises the proper time of the moving object.

and the energy is defined as the conserved quantity  $E := \vec{p} \cdot \vec{v} - L$ . This yields

$$E = \frac{m}{\sqrt{1 - v^2}}. \quad (1.11)$$

Upon reinserting  $c$  and expanding in powers of  $v \ll c$ , one finds

$$E = mc^2 \left( 1 + \frac{v^2}{2c^2} + \dots \right). \quad (1.12)$$

This is the Newtonian expression for the energy of a free particle with an extra contribution proportional to its mass. The fact that the mass of a particle is just an aspect of its energy is one of the important lessons of Special Relativity.

### 1.3 General Theory of Relativity

General Relativity pursues Galileo’s observation that all masses fall with the same acceleration by prescribing that all forms of energy are equally affected by gravity. This is natural in a theory in which mass is but an aspect of energy. The immediate consequence is that there should be no experimental way to distinguish the effect of gravity from an acceleration of the whole laboratory. This is known as the *Equivalence principle*.<sup>(1)</sup> Gravity is embedded in the geometry of space-time itself. When dealing with general relativity, it is customary to work in *natural units* in which the Newton constant and the speed of light are both equal to one ( $G = c = 1$ ). For details on the choice of units, see Appendix A.

---

<sup>(1)</sup>To be precise, one should distinguish between the so called *strong* and *Einstein* equivalence principles. The latter states that the nature of the acceleration of the laboratory can be determined solely by means of gravitational local experiment. For a review and comparison with experiments, see (Will 2014).

The action of a point particle can be generalised to the case of a space-time with metric components  $g_{\mu\nu}$  as

$$S \sim \int ds = \int \sqrt{g_{\mu\nu} dx^\mu dx^\nu} , \quad (1.13)$$

where the integral is taken between two events that serve as boundary conditions.

General Relativity is a geometric theory of space-time without torsion in which the effects of gravitation are entirely contained in the curvature of space-time. The metric is not given *a priori* but depends on the space-time energy content. Its dynamics is given by Einstein field equations:

$$R_{\mu\nu} - \frac{1}{2}g_{\mu\nu}R = 8\pi T_{\mu\nu} , \quad (1.14)$$

where  $R_{\mu\nu}$  is the *Ricci tensor* (the trace of the Riemann curvature tensor),  $R$  is its trace known as the *Ricci Scalar* and  $T_{\mu\nu}$  is the *stress-energy tensor*. These equations involve up to second order derivatives of the metric, are highly nonlinear and can be derived from the least action principle applied to the Einstein-Hilbert action

$$S = \frac{1}{16\pi} \int d^4x \sqrt{-g} R + S_{\text{matter}} . \quad (1.15)$$

where the extremisation of  $S_{\text{matter}}$  gives the equations of motion of the energy content alone. The stress energy tensor is then defined from the lagrangian density of matter  $S_{\text{matter}} := \int d^4x \sqrt{-g} \mathcal{L}_{\text{matter}}$  through

$$T_{\mu\nu} := \frac{-2}{\sqrt{-g}} \frac{\partial(\sqrt{-g} \mathcal{L}_{\text{matter}})}{\partial g^{\mu\nu}} . \quad (1.16)$$

The Einstein equations are, in general, very complex to solve and the solution is analytical only in some very specific cases.

## 1.4 Cosmology

The equations of General Relativity can be used to solve local gravitational problems such as the orbit of a planet around a star or the computation of the trajectories of light rays in the vicinity of large masses. In any case, it is always necessary to prescribe boundary conditions. As far as one is concerned with astrophysical problems, it is all very good to ask the metric to be Minkowski<sup>(2)</sup> far from any energy source. However, this cannot be a valid approximation on larger scales where the average energy density and pressure are non-zero. This consideration leads to physical cosmology.

---

<sup>(2)</sup>*i.e.* that of Special Relativity.

Georges Lemaître suggested the idea that the spatial part of the Universe might be expanding in time (Lemaître 1927). The solution he proposed had the merit to reconcile the individual successes of previous solutions of both Einstein and de Sitter. In the former (Einstein 1917), the Universe is static which, at the time, was already in contradictions with the early results from Hubble's measurements on the redshifts of distant galaxies (Hubble 1926). The de Sitter solution (de Sitter 1917) was consistent with these measurements but described a Universe empty of matter. Similar work to Lemaître's had previously been done independently by Friedmann (Friedmann 1922). The prediction of an expanding Universe was later consolidated by Hubble (Hubble 1929).

Lemaître's Universe is dynamical and predicts a geometrical singularity of infinite energy density called the *Big Bang* that occurs at a finite time in the past. Modern estimations set this around 13.7 billion years ago. Regardless of what exactly happens at this time, the theory predicts the emission of the *Cosmic Microwave Background* (CMB) when the Universe is still very young.

When the mean energy density of the Universe exceeds the value needed to ionise the hydrogen atom, the Universe is filled with a gas of ionised matter that is opaque to light due to the large amount of scattering in the electrostatic medium. The trapped light is released when the energy density of the Universe drops below this threshold value. The time it happens is usually referred to as the *time of last scattering*. The emitted light is in thermal equilibrium and is responsible for the CMB signal detected today as a black body radiation (Mather et al. 1994). Observations of the temperature anisotropies in the signal reveal that the Universe at the time of last scattering is isotropic to  $\Delta T/T \sim 10^{-5}$ . The detailed study of the CMB anisotropies (Bennett et al. 2003, Ade et al. 2014b) is an invaluable tool for the study of small perturbations in the early Universe. We discuss this in more details later in the next section. For the time being, we regard the Universe as really close to being isotropic.

The shape of the Universe as prescribed by Lemaître can be expressed in the language of modern cosmology. We illustrate the mathematics involved by considering the case of an isotropic 2-dimensional space which is straightforwardly generalised to the 3-dimensional case.

Without loss of generality, the isotropic 2-dimensional space squared line-element can be written as

$$dl^2 = f(r)dr^2 + r^2d\theta^2, \quad (1.17)$$

with the constraint  $f(r) > 0 \forall r$ . The Ricci scalar being the quantity representing the mean curvature of space-time, it must be a constant on cosmological scales. This leads to the constraint

$$R = \frac{f'}{rf^2} = 2k, \quad (1.18)$$

with  $f' := \frac{df}{dr}$ . The solution of this gives the line element

$$dl^2 = \frac{dr^2}{1 - kr^2} + r^2d\theta^2. \quad (1.19)$$

The parameter  $k$  can further be normalised by rescaling the radial coordinate.

Following the same steps for the 3 dimensional spatial part of the Universe while allowing its radius to grow in size gives

$$ds^2 = -dt^2 + a^2(t) \left( \frac{dr^2}{1 - kr^2} + r^2 d\Omega^2 \right), \quad (1.20)$$

where  $d\Omega$  is the infinitesimal element of solid angle. The function  $a(t)$  is the *scale factor* relating the size of any space-like distance at different times. The expansion rate is measured by means of the Hubble parameter  $H := \frac{\dot{a}}{a}$ . As all physical distances grow in time, the ratio of the wavelength of a photon at the time of its emission to its wavelength at the time of observation is

$$\frac{\lambda_e}{\lambda_o} = \frac{a_e}{a_o}. \quad (1.21)$$

The photon is therefore redshifted as the Universe expands. The redshift parameter is defined as  $z := \frac{\lambda_o - \lambda_e}{\lambda_e}$ . If one fixes the present day value of the scale factor to unity as is customary, there is a one-to-one correspondence between the scale factor and the redshift. The redshift though is model-independent which makes it a very appreciated quantity. As a one-to-one correspondence also exists between the scale factor and time coordinate, the cosmological evolution can be described in terms of any of  $a$ ,  $z$  or  $t$ . The time coordinate of Eq. (1.20) is the proper time of an observer that sees the distribution of energy in the Universe as a constant in space. This is called the *synchronous time*.

The geometry described by the line-element (1.20) was analysed by Robertson and Walker during the decade following Lemaître's work. For this reason, this model of Universe is usually referred to as *Friedmann-Lemaître-Robertson-Walker* (FLRW). We investigate the dynamics of this solution in the next chapter once we are in possession of all the tools we need.

## 1.5 Precision Cosmology

The development of modern observation techniques has allowed cosmology to enter an age of high precision measurements. Observations of remote supernovae have shown that the distant regions of the Universe recede at a growing velocity (Riess, Schmidt et al. 1998, Perlmutter and Supernova Cosmology Project 1999). This fact points towards a Universe in a phase of accelerated expansion.

The nature of the energy causing this acceleration is not known. This could be due to a positive cosmological constant, the vacuum energy of the Universe or a new unknown degree of freedom. These possibilities are grouped under the name *Dark Energy*. It is customary to define the density parameters for the components of the Universe as the ratio to the total energy density. The dark energy density parameter is then  $\Omega_\Lambda := \rho_\Lambda / \rho_c$ . A similar definition also holds for matter and radiation. The quantity  $\rho_c$  is the value of the total energy

density of a Universe with Hubble parameter  $H$  and zero spatial curvature. Formally,

$$1 - \frac{8\pi\rho_c}{3H^2} = -\frac{k}{a^2H^2} = 0. \quad (1.22)$$

For models similar to the standard model, one has  $\Omega_\Lambda \sim 0.7$ . The remainder is mostly due to *Cold Dark Matter* (CDM)<sup>(3)</sup>. These parameters can be estimated via high precision observations of supernovae and the CMB spectrum. The result is that today's value of the total energy density is very closed to the critical value. The standard model of Universe with CDM and a cosmological constant is named  $\Lambda$ CDM.

Photons of the CMB gravitationally interact with large scales structures. When these encounter an over-dense region, these gain energy by falling in the potential well. As the dense region gets even denser in time, the photon needs more energy to escape the gravitational well than it gained by falling in. This appears as a redshifted region on the CMB map. If the region is instead under-dense, the photon is blue-shifted. This effect is known as the *integrated Sachs-Wolfe effect*. As the dynamics of the Universe influences the growth of large scales structures, this phenomenon can be used to set bounds on the cosmological parameters.

The fact that the present day values of the dust energy and dark energy densities should be so close to one another comes as a striking coincidence that many cosmological models seek to explain. But the study of the CMB reveals more cosmic puzzles.

## 1.6 Inflation

Inflation is a phase of exponential expansion that is believed to take place soon after the Big Bang singularity. This is usually assumed to solve the three problems of *Flatness*, *Horizon* and the absence of *Topological defects* (Weinberg 2008).

As physical distances measured in the Universe are rescaled by expansion, it is useful to use the comoving distance defined at all time as the ratio of the physical distance and the scale factor.<sup>(4)</sup> The comoving distance to an emitting region of the sky is a constant that can be expressed either as an integral over the coordinate time or the cosmological redshift.

$$d = \int_{t_e}^{t_o} \frac{dt}{a(t)} = \int_{z_o}^{z_e} \frac{dz}{H(z)}, \quad (1.23)$$

where  $t_e$  and  $t_o$  are the time of the emission and observation respectively. The *particle horizon* of an observer is defined as the maximal distance within which

<sup>(3)</sup>The problem of Dark Matter is not an issue we wish to address in this work. For more information, see d'Amico et al. (D'Amico, Kamionkowski and Sigurdson 2009). We shall be happy with simply classifying Dark Matter as dust.

<sup>(4)</sup>For a detailed synthesis of the various definitions of distance in cosmology, see Hogg et al. (Hogg 1999)

all the events are in causal contact. Fixing  $t = 0$  as the time of the Big Bang, the comoving distance to the particle horizon at time  $t$  corresponding to a redshift  $z$  reads

$$d_{\text{H}} = \int_0^t \frac{dt'}{a(t')} = \int_z^{+\infty} \frac{dz}{H(z)}. \quad (1.24)$$

Calculations of the probability of photon-electron collisions as a function of the ionisation of the primordial gas fixes the redshift of the emission of the CMB around  $z \sim 1090$  (Weinberg 2008). Under the assumption that the Universe is adequately described by the simple  $\Lambda$ CDM without inflation, the comoving distance to the particle horizon is finite and comes out as  $d_{\text{H}} \sim 0.46\text{Mpc}$ . At last scattering, the size of today's observable Universe is  $d_{\text{LS}} \sim 14\,189\text{Mpc}$  (Serjeant 2010). This distance is usually referred to as the distance to the *surface of last scattering*. The associated angular diameter distance is  $d_{\text{LS}}^{\text{A}} = d_{\text{LS}}/(1+z) \sim 13\text{Mpc}$ . This means that the angle that subtends the particle horizon on the CMB sky is  $0.46/13$  radians. That is,  $\sim 2^\circ$ .

As regions of the CMB sky that lie more than  $2^\circ$  apart are not in causal contact at the time of recombination it comes as a striking coincidence that the overall temperature of the CMB should be so homogeneous. That is the argument pointing toward the Horizon problem.

The theory of inflation solves this by assuming that the observable Universe today is well within the size of the particle horizon before recombination and then undergoes a period of exponential expansion sending its size well beyond the particle horizon. Inflation then stops and the Universe resorts to a slower expansion bringing larger scales back into the particle horizon. The growth of the scale factor needed to bring all the CMB scales within the horizon on the onset of inflation depends on the details of the model but lies always within the range  $10^{17}$  to  $10^{27}$ .

The so called flatness problem is not unrelated to the issue of fine-tuning of the present day cosmological parameters. It comes as another coincidence that the sum of today's cosmological density parameters should be very close to unity. If the expansion of the Universe proceeds in a monotonous power-law in time, so does the curvature density parameter  $\Omega_k := k/a^2 H^2$ . This means that the absolute value of the curvature parameter is even smaller at earlier time. There is no contradiction in this but it is nonetheless puzzling. As  $a \sim e^{Ht}$  and  $H \sim cst$  during inflation, the curvature density parameter decreases exponentially which naturally explains why it is very small at present day while alleviating the initial condition coincidence problem.

The last puzzle comes from considerations of High Energy physics. Certain theories explore the possibility for the overall symmetry of the standard model of particle physics to be the remainder of a larger spontaneously broken group of symmetry. Such theories predict the production of many scalar field amongst other particles resulting from spontaneous symmetry breaking. If there is no inflation, there are many regions with uncorrelated classical values of the field that are not in causal contact. This results in the production of topological defects such as *monopoles* that should be as abundant as the nucleons today.

The lack of detection of any monopole as of the writing of this thesis sets tight bounds on the ratio of monopoles per nucleons (Weinberg 2008). As the particle horizon is bigger than the observable Universe at the end of inflation, the values of the various scalar fields are the same in all regions of our observed Universe and there is few to no monopole.

The dynamics of any consistent theory of inflation must explain why it does not last forever, as far as the observable Universe is concerned, and provide a mechanism for the transition to the radiation era. The most accomplished model to meet these requirements is that where inflation is driven by the dynamics of one or more scalar fields.

Many successful models of Dark Energy (DE) are built with the same material. Due to their similarities with the early model of de Sitter empty Universe, the phases of exponential expansions generated by these models are called de Sitter phases.

## 1.7 Structure formation

A very natural question that comes to mind when considering the Universe is “how did the smooth Universe left after inflation evolved into the Universe that we observe today” ? Indeed, even though it is very close to homogeneity on very large scales, there are regions of the Universe empty of matter on smaller scales whereas other regions are the surroundings of large matter structures. The study of the processes responsible for this distribution of matter is a fascinating field of its own.

At the end of inflation, the distribution of structures is very close to be independent of their scale (a fact that we discuss in Chapter 3). One says that the power spectrum of cosmological perturbations is (close to being) scale-invariant:

$$\mathcal{P}(k) \sim k^0 , \tag{1.25}$$

where  $k$  is the Fourier mode of a fluctuations of scale  $\sim 1/k$ . The computation of correlation functions between primordial fluctuations further allows to check their probability distribution. The power spectrum contains all the information about the probability distribution of density fluctuation in the case where it is simply gaussian.

Knowing the distribution of structures just after inflation, one wishes to compute it at later time and this evolution is related to that of the Universe in the aftermath of inflation.

Once inflation has ended, the Universe rapidly enters an age of milder expansion in which the dominant part of its energy density is due to relativistic particles that travel at, or close to, the speed of light. As the Universe grows older, these radiations lose energy as their wavelengths get redshifted by expansion. This causes the Universe to enter another phase dominated by cold matter of which the loss of energy through cosmological redshift is negligible.

During that era, the expansion is sufficiently mild to allow fluctuations in the matter energy density distribution to draw closer and closer to one another leading to the formation of the structures that we observe today.

In the last decades, the evolution of computational capacities and methods have allowed to achieve tremendous advances in structure formation simulations (Springel et al. 2005, Alimi et al. 2012, Bouillot et al. 2015). These methods consist in solving for the evolution of the distribution of matter within very large computational domains and rely on N-body simulations of the dynamics within a gravitational Newtonian potential. This potential is what results from the evolution of what it is at the end of inflation after horizon crossing and the transition from radiation to matter dominated eras. The subsequent evolution being due to the expansion during the matter dominated era (Dodelson 2003). The evolution of the gravitational potential can be tracked down to the matter inhomogeneities by means of a Poisson equation. In order to provide the correct feedback of gravity on the structure distribution, it is therefore mandatory to have an accurate model of the growth of these at one's disposal. Such model is expected to go beyond the cosmological perturbations formalism in order to find accurate results beyond the linear order. The large inhomogeneities thus studied are halos of galaxies and allow to get a lot of insight about the cosmological evolution of the Universe and its content as the formation of those depend on the homogeneous model used.

The most well-known model of non-linear evolution of over-densities is the so called *top-hat* model in which the Universe is piecewise homogeneous and isotropic and remains so during the whole collapse process. The Universe is then effectively described as a two-regions space-time with one region serving as background, the other being the overdense region. The discussion of this model and its comparison to our proposed fully relativistic substitute is the object of Chapter 4.

In the next chapter, we present a mathematical formalism used to describe the cosmological evolution based on the (3+1)-decomposition of space-time.



## Chapter 2

# (3+1) Formulation of General Relativity

The fundamental object of General Relativity is space-time to which time and space are just aspects. On many occasions, it is desirable to study the time evolution of some quantities on the dynamical space-time. This is especially true in cosmology. One should therefore seek for a way to split the description of space-time that consistent with the principles of General Relativity. This issue is even more crucial when one wishes to solve Einstein equations on a computer.

General Relativity as a geometric theory must be independent of the choice of coordinates. However, fixing coordinates is mandatory for practical computations. The so-called (3+1)-formalism allows to split space-time while keeping track of physical degrees of freedom as well as those that are purely due to the choice of coordinates.

### 2.1 Splitting of space-time

Following the conventions of Poisson's lecture (Poisson 2002), let  $t(x^\mu)$  be a curve on a 4-dimensional space-time with coordinates  $\{x^\mu\}$ . The implicit equation  $\Phi := t_0 - t(x^\mu) = 0$ , defines a collection of hypersurfaces labelled with a constant parameter  $t_0$  which we denote by  $\Sigma_{t_0}$ . The unit normal vector to all hypersurfaces is  $n_\mu = -\alpha \frac{\partial t}{\partial x^\mu}$ .  $\alpha$  is the norm of  $n^\mu$ .

Let  $\{y^i\}$  be a set of coordinates on the hypersurface  $\Sigma_t$ . Any event is identified by the set of numbers  $\{t, y^i\}$ . The choice of coordinates on one hypersurface is independent of the choice on the others.

The pullback between space-time and  $\Sigma_t$  is  $e_i^\mu = \left( \frac{\partial x^\mu}{\partial y^i} \right)_t$ . The time curve  $t(x^\mu)$  needs not be normal to the hypersurface. Its tangent vector  $t^\mu = \frac{dx^\mu}{dt}$

can be decomposed as

$$t^\mu = \alpha n^\mu + \beta^i e_i^\mu . \quad (2.1)$$

The three numbers  $\beta^i$  are the coefficients of the projection of the tangent vector on the hypersurface.

The choice of the function  $\alpha$  defines a *foliation of space-time*. The *lapse*  $\alpha$  is the interval of proper time measured by an observer moving along a worldline normal to all hypersurface. Such an observer is called an *Eulerian observer*. The  $\beta^i$  functions are the *shifts* and denote the relative velocity between the Eulerian observer and the events of constant spatial coordinate.<sup>(1)</sup>

The relation  $x^\mu = x^\mu(t, y^i)$  defines a coordinate transformation. Differentiation yields

$$dx^\mu = t^\mu dt + e_i^\mu dy^i . \quad (2.2)$$

The line element in the coordinates  $\{t, y^i\}$  is then

$$ds^2 = -\alpha^2 dt^2 + \gamma_{ij}(dy^i + \beta^i dt)(dy^j + \beta^j dt) , \quad (2.3)$$

with  $\gamma_{ij} := g_{\mu\nu} e_i^\mu e_j^\nu$ , the three metric induced on the hypersurface. The inverse relation is

$$g^{\mu\nu} = \gamma^{ij} e_i^\mu e_j^\nu - n^\mu n^\nu . \quad (2.4)$$

From these, one directly identifies the metric tensor and its inverse

$$g_{\mu\nu} = \begin{pmatrix} -\alpha^2 + \beta_i \beta^i & \beta_i \\ \beta_i & \gamma_{ij} \end{pmatrix} , \quad g^{\mu\nu} = \frac{1}{\alpha^2} \begin{pmatrix} -1 & \beta^i \\ \beta^i & \gamma^{ij} \alpha^2 - \beta^i \beta^j \end{pmatrix} . \quad (2.5)$$

Equation (2.4) can be rearranged as

$$\gamma^{ij} e_i^\mu e_j^\nu = g^{\mu\nu} + n^\mu n^\nu . \quad (2.6)$$

The quantity so defined is used to project any tensor onto the hypersurface. It is standard to dispose of the  $e_i^\mu$  symbols and to write simply

$$\gamma^{\mu\nu} := \gamma^{ij} e_i^\mu e_j^\nu . \quad (2.7)$$

The extrinsic curvature of a hypersurface is a measure of how it is bent within its surrounding space-time. One way to access this information is by considering the parallel transport of the normal vector along curves within the hypersurface. In that sense, a flat hypersurface would have a constant normal vector. Following this idea, one defines the extrinsic curvature tensor as the projection

$$\begin{aligned} K_{\mu\nu} &:= -\gamma_\mu^\sigma \nabla_\sigma n_\nu \\ &= -(\nabla_\mu n_\nu + n_\mu n^\sigma \nabla_\sigma n_\nu) . \end{aligned} \quad (2.8)$$

---

<sup>(1)</sup>This velocity is geometrical and needs not be smaller than the speed of light.

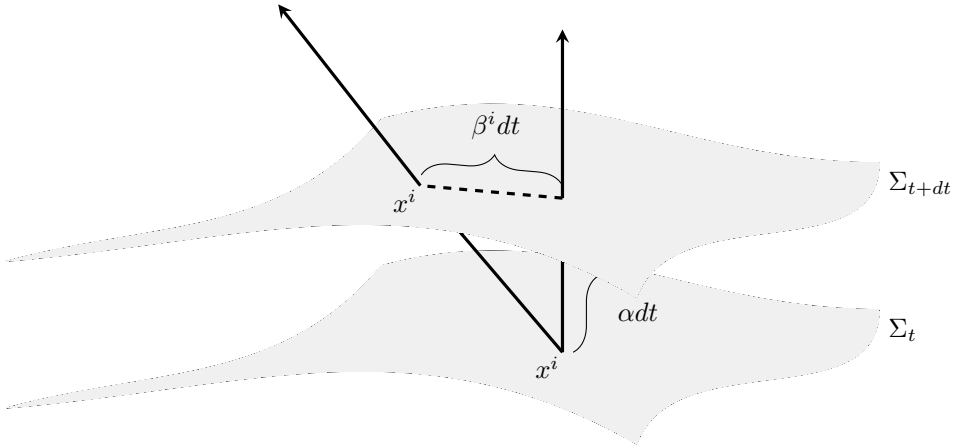


Figure 2.1 – Foliation of space-time in the (3+1)-formalism.  $\alpha dt$  is the lapse of proper time measured by an Eulerian observer.  $\beta^i$  is the shift displacement between this observer and the point of constant spatial coordinates  $x^i$

This defines the extrinsic curvature as a tangent tensor so that  $n^\mu K_{\mu\nu} = 0$ <sup>(2)</sup>. It is remarkable to note that this tensor can be expressed as the Lie derivative of the 3-metric along the normal vector  $n^\mu$ ,

$$\begin{aligned}
 \mathcal{L}_n \gamma_{\mu\nu} &= n^\alpha \nabla_\alpha \gamma_{\mu\nu} + \gamma_{\mu\alpha} \nabla_\nu n^\alpha + \gamma_{\alpha\nu} \nabla_\mu n^\alpha \\
 &= n^\alpha \nabla_\alpha (n_\mu n_\nu) + g_{\mu\alpha} \nabla_\nu n^\alpha + g_{\alpha\nu} \nabla_\mu n^\alpha \\
 &= n^\alpha n_\mu (\nabla_\alpha n_\nu) + n^\alpha n_\nu (\nabla_\alpha n_\mu) + \nabla_\nu n_\mu + \nabla_\mu n_\nu \\
 &= \gamma_\mu^\alpha \nabla_\alpha n_\nu + \gamma_\nu^\alpha \nabla_\alpha n_\mu \\
 &= -2K_{\mu\nu} .
 \end{aligned} \tag{2.9}$$

Given a tangent vector  $v_\nu$ , it can be proved that one recovers the Levi-Civita connection denoted by the operator  $D_\mu$  on the hypersurface through

$$\begin{aligned}
 D_\mu v^\nu &:= \gamma_\mu^\alpha \gamma_\beta^\nu \nabla_\alpha v^\beta \\
 &= \gamma_\mu^\alpha \nabla_\alpha v^\nu - \gamma_\mu^\alpha n^\nu v^\beta \nabla_\alpha n_\beta \\
 &= \gamma_\mu^\alpha \nabla_\alpha v^\nu + \gamma_\mu^\alpha n^\nu v^\beta K_{\alpha\beta} ,
 \end{aligned} \tag{2.10}$$

using the definition of  $K_{\mu\nu}$  and  $n_\mu K_{\mu\nu} = 0$ . The last term of Eq. (2.10) is the component of the gradient along the normal vector. One thus has that when  $K_{\mu\nu} = 0$ , the gradient of a tangent vector is also tangent.

<sup>(2)</sup>From now on, we refer to tensors tangent to the hypersurfaces simply as *tangents* when no confusion is possible.

In his introductory book (Gourgoulhon 2012), E. Gourgoulhon derives the very helpful formula

$$n^\mu \nabla_\mu n_\nu = \frac{1}{\alpha} D_\nu \alpha . \quad (2.11)$$

This allows to write the covariant derivative of  $n_\mu$  as

$$\begin{aligned} \nabla_\nu n_\mu &= -K_{\mu\nu} - (n^\sigma \nabla_\sigma n_\mu) n_\nu \\ &= -K_{\mu\nu} - \frac{1}{\alpha} (D_\mu \alpha) n_\nu , \end{aligned} \quad (2.12)$$

and also provides another useful relation between the divergences of tangent tensors. E.g. , for a vector

$$\begin{aligned} D_\mu v^\mu &= \gamma_\mu^\lambda \gamma_\sigma^\mu \nabla_\lambda v^\sigma \\ &= \nabla_\mu v^\mu - v^\mu n^\sigma \nabla_\sigma n_\mu \\ &= \nabla_\mu v^\mu - \frac{1}{\alpha} v^\mu D_\mu \alpha . \end{aligned} \quad (2.13)$$

A similar expression holds for tensors of any ranks.

The choice of foliation through  $\alpha$  and  $\beta^i$  is equivalent to a choice of gauge. Once these are fixed the dynamics of space-time is found by studying the evolution of the geometry of the hypersurfaces. Both the evolution equations and the initial data must be compatible with the Einstein equations. In the next section, we rewrite these in a form suited to the (3+1)-formalism.

## 2.2 Dynamics of space-time

From the linearity of the Lie derivative and the definition of the extrinsic curvature, one has

$$\begin{aligned} -2K_{\mu\nu} &= \mathcal{L}_n \gamma_{\mu\nu} \\ &= \mathcal{L}_{\left(\frac{t}{\alpha} - \frac{\beta}{\alpha}\right)} \gamma_{\mu\nu} \\ &= \frac{1}{\alpha} (\mathcal{L}_t \gamma_{\mu\nu} - \mathcal{L}_\beta \gamma_{\mu\nu}) \\ &= \frac{1}{\alpha} (\partial_t \gamma_{\mu\nu} - D_\mu \beta_\nu - D_\nu \beta_\mu) . \end{aligned} \quad (2.14)$$

The first set of dynamical equations is then

$$\partial_t \gamma_{\mu\nu} = -2\alpha K_{\mu\nu} + D_\mu \beta_\nu + D_\nu \beta_\mu . \quad (2.15)$$

The equations for the evolution of the extrinsic curvature are found from the Einstein equations in the form

$$R_{\mu\nu} = 8\pi \left( T_{\mu\nu} - \frac{1}{2} g_{\mu\nu} T \right) . \quad (2.16)$$

The projections of the stress-energy tensor are

$$\begin{aligned} E &:= n_\alpha n_\beta T^{\alpha\beta} , \\ j_\mu &:= -\gamma_{\mu\alpha} n_\beta T^{\alpha\beta} , \\ S_{\mu\nu} &:= \gamma_{\alpha\mu} \gamma_{\beta\nu} T^{\alpha\beta} , \end{aligned} \quad (2.17)$$

where  $E$  and  $j_\mu$  are respectively the *energy* and *momentum* densities. The last quantity gives the *stress* tensor of matter. The projection of the Riemann tensor onto the hypersurface gives the *Gauss-Codazzi* equations (Alcubierre 2008):

$$\gamma_\alpha^\mu \gamma_\beta^\nu \gamma_\gamma^\lambda \gamma_\delta^\sigma R_{\mu\nu\lambda\sigma} = {}^{(3)}R_{\alpha\beta\gamma\delta} + K_{\alpha\gamma} K_{\beta\delta} - K_{\alpha\delta} K_{\beta\gamma} , \quad (2.18)$$

where  ${}^{(3)}R_{\mu\nu\lambda\sigma}$  is the curvature tensor of the hypersurface. Another useful projection gives the *Gauss-Mainardi* equations:

$$\gamma_\mu^\alpha \gamma_\nu^\beta n^\gamma n^\delta R_{\alpha\beta\gamma\delta} = \mathcal{L}_n K_{\mu\nu} + K_{\mu\lambda} K_\nu^\lambda + \frac{1}{\alpha} D_\mu D_\nu \alpha . \quad (2.19)$$

Combining Eq. (2.18) and Eq. (2.19) together with Einstein equations gives

$$\begin{aligned} \partial_t K_{\mu\nu} - \mathcal{L}_\beta K_{\mu\nu} &= -D_\mu D_\nu \alpha + \alpha \left[ {}^{(3)}R_{\mu\nu} + K K_{\mu\nu} - 2K_{\mu\lambda} K_\nu^\lambda \right] \\ &\quad + 4\pi\alpha [\gamma_{\mu\nu}(S - E) - 2S_{\mu\nu}] . \end{aligned} \quad (2.20)$$

Eq. (2.15) and Eq. (2.20) fully describe the evolution of space-time. The remaining projections of the Einstein equations give constraints on this evolution.

$$2n^\mu n^\nu G_{\mu\nu} = {}^{(3)}R + K^2 - K_{\mu\nu} K^{\mu\nu} , \quad (2.21)$$

$$\gamma_\mu^\alpha n^\beta G_{\alpha\beta} = D_\nu K_\mu^\nu - D_\mu K . \quad (2.22)$$

Which yield

$${}^{(3)}R + K^2 - K_{\mu\nu} K^{\mu\nu} = 16\pi E \quad (2.23)$$

$$D_\mu K_\mu^\nu - D_\mu K = 8\pi j_\mu . \quad (2.24)$$

This set of equations is colloquially referred to as the ADM equations although they differ slightly to their original form (Arnowitt, Deser and Misner 1962). This formalism is to traditional Einstein theory what Hamiltonian equations are to Lagrange formalism. It can be shown that the  $K_{\mu\nu}$  are linked to the conjugate quantities of the 3-metric components in the same way momentum is related to position. The ADM formalism is well-suited to many analytical cases. We apply it to homogeneous cosmology within this chapter and to cosmological perturbations in chapter 3. The numerical treatment of the equations of space-time requires special additional care that we sketch out later in this chapter.

## 2.3 Energy and momentum conservation

The conservation of energy in general relativity is expressed as

$$\nabla_\mu T_\nu^\mu = 0 . \quad (2.25)$$

This can be written in a way more suited to the (3+1)-formalism. In this section, we intend to do this followingourgoulhon's book (Gourgoulhon 2012).

The stress-energy tensor can be decomposed in terms of its projections listed in Eq. (2.17):

$$T_\nu^\mu = S_\nu^\mu + n^\mu j_\nu + j^\mu n_\nu + E n^\mu n_\nu . \quad (2.26)$$

Equation (2.25) then reads

$$\begin{aligned} \nabla_\mu S_\nu^\mu + (\nabla_\mu n^\mu) j_\nu + n^\mu (\nabla_\mu j_\nu) + (\nabla_\mu j^\mu) n_\nu + j^\mu (\nabla_\mu n_\nu) \\ + (\nabla_\mu E) n^\mu n_\nu + E (\nabla_\mu n^\mu) n_\nu + E n^\mu (\nabla_\mu n_\nu) = 0 . \end{aligned} \quad (2.27)$$

Using Eq. (2.11) and the fact that  $j_\mu$ ,  $K_{\mu\nu}$  and  $D_\mu$  are all tangent, this gets rewritten as

$$\begin{aligned} \nabla_\mu S_\nu^\mu - K j_\nu + n^\mu (\nabla_\mu j_\nu) + (\nabla_\mu j^\mu) n_\nu - K_{\mu\nu} j^\mu \\ + (\nabla_\mu E) n^\mu n_\nu - K E n_\nu - \frac{1}{\alpha} E (D_\mu \alpha) = 0 . \end{aligned} \quad (2.28)$$

Projection onto the normal vector leaves

$$n^\nu \nabla_\mu S_\nu^\mu + n^\mu n^\nu (\nabla_\mu j_\nu) - (\nabla_\mu j^\mu) - (\nabla_\mu E) n^\mu + K E = 0 . \quad (2.29)$$

Now, since  $n^\nu S_\nu^\mu = n^\nu j_\nu = 0$ , this becomes

$$K_{\mu\nu} S^{\mu\nu} - \frac{1}{\alpha} j_\nu (D^\nu \alpha) - (\nabla_\mu j^\mu) - (\nabla_\mu E) n^\mu + K E = 0 . \quad (2.30)$$

Finally, using Eq. (2.13) and the fact that,  $E$  being a scalar,  $(\nabla_\mu E) n^\mu = \mathcal{L}_n E$  one finds the equation for the conservation of energy

$$\mathcal{L}_n E + D_\mu j^\mu + \frac{2}{\alpha} j_\mu (D^\mu \alpha) - K E - K_{\mu\nu} S^{\mu\nu} = 0 . \quad (2.31)$$

Similarly, projection of Eq. (2.28) onto the hypersurface leaves

$$\gamma_\sigma^\nu \nabla_\mu S_\nu^\mu - K j_\sigma + \gamma_\sigma^\nu n^\mu (\nabla_\mu j_\nu) - K_{\mu\sigma} j^\mu + \frac{1}{\alpha} E (D_\sigma \alpha) = 0 . \quad (2.32)$$

Now, from the definition of the Lie derivative and the extrinsic curvature

$$\begin{aligned} \mathcal{L}_n j_\nu &= n^\mu \nabla_\mu j_\nu + j_\mu K_\nu^\mu \\ &= n^\mu \nabla_\mu j_\nu - j_\mu (\nabla_\nu n^\mu) . \end{aligned} \quad (2.33)$$

Upon rewriting the divergence of  $S_\nu^\mu$  in terms of  $D_\mu$ , one arrives to the expression for the conservation of momentum

$$\mathcal{L}_{\bar{n}} j_\sigma + D_\mu S_\sigma^\mu + S_\sigma^\mu \frac{D_\mu \alpha}{\alpha} - K j_\sigma + E \frac{D_\sigma \alpha}{\alpha} = 0 . \quad (2.34)$$

We now put to use the various expressions of the previous sections and derive the Friedmann equations governing the dynamics of the FLRW Universe.

## 2.4 The Friedmann equations

Because the FLRW space-time is homogeneous, there is no need for the set of coordinates to depart from the normal and we simply set the shift to zero ( $\beta = 0$ ). However, keeping the lapse as an arbitrary function of time is often helpful. The ansatz we use from now on is

$$ds^2 = -\alpha^2(t)dt^2 + a^2(t) \left( \frac{dr^2}{1 - kr^2} + r^2 d\Omega^2 \right). \quad (2.35)$$

The curvature parameter  $k$  can be normalised so that 3 cases need to be considered i)  $k=+1$  gives the spatial geometry of the *3-sphere*, ii)  $k=-1$  gives the *3 dimensional hyperbolic space* and iii)  $k=0$  sets the spatial part of space-time to the Euclidian space. The latter is the most likely to describe the observable Universe even though the discussion on the shape of our Universe is not closed<sup>(3)</sup>.

With this gauge choice, each hypersurface is an Einstein manifold. Such manifolds have isotropic curvature. In our case,

$${}^{(3)}R_{ij} = 2 \frac{k}{a^2} \gamma_{ij}. \quad (2.36)$$

The extrinsic curvature is found to be traceless from its definition

$$K_{ij} = \frac{1}{3} K \gamma_{ij} = -\frac{a\dot{a}}{\alpha} \delta_{ij}. \quad (2.37)$$

The Hamiltonian constraint thus reads

$$\frac{1}{\alpha^2} \left( \frac{\dot{a}}{a} \right)^2 - \frac{k}{a^2} = \frac{8\pi}{3} E. \quad (2.38)$$

This is the *Friedmann equation*. This can be used, in principle, to integrate for  $a(t)$  in a way very similar to computing the motion of a particle from the constraint on its total energy.

As we show later, the stress-energy tensor of the distribution of matter in a homogeneous Universe is diagonal. The momentum density is equal to zero ( $j_\mu = 0$ ) and the stress tensor is simply proportional to the metric ( $S_{\mu\nu} = S\gamma_{\mu\nu}$ ). The evolution equation then gives

$$\begin{aligned} & \frac{2}{3} \frac{\dot{a}}{a} \left( -\frac{3}{\alpha} \frac{\dot{a}}{a} \right) \gamma_{ij} + \frac{1}{3} \partial_t \left( -\frac{3}{\alpha} \frac{\dot{a}}{a} \right) \gamma_{ij} + 2 \frac{k}{a^2} \gamma_{ij} \\ & = \alpha \left( \frac{1}{9} \gamma_{ij} K^2 - \frac{2}{3} \gamma_{ik} \delta_j^k \frac{1}{3} K \right) + 4\pi\alpha \left( -E + \frac{1}{3} S \right) \gamma_{ij}. \end{aligned}$$

---

<sup>(3)</sup>For a very good lay-person introduction, consult the NASA website (*NASA Will the Universe expand forever?* n.d.)

Plugging in the Hamiltonian constraint yields

$$-\frac{1}{\alpha^2} \frac{\ddot{a}}{a} + \frac{1}{\alpha^2} \frac{\dot{\alpha}}{\alpha} \frac{\dot{a}}{a} = \frac{4\pi}{6} (E + S) . \quad (2.39)$$

We refer to this as the *acceleration equation*. However, we often refer to both Eq. (2.38) and Eq. (2.39) as the *Friedmann equations* or simply FLRW equations.

## 2.5 Accelerated expansion

On very large scales, it is customary to model the energy content of the Universe as a collection of fluids. The general form of the stress-energy tensor of a fluid with 4-velocity  $u^\mu$  is (Ellis and van Elst 1998)

$$T_{\mu\nu} = \rho u_\mu u_\nu + q_\mu u_\nu + q_\nu u_\mu + p \gamma_{\mu\nu} + \pi_{\mu\nu} , \quad (2.40)$$

where  $\rho$  is the *energy density*,  $q_\mu$  the *momentum density*,  $p$  the *pressure* and  $\pi_{\mu\nu}$  the *anisotropic pressure as observed in the fluid's rest frame*. These are in general different, though related, to their counterparts, the source terms of the ADM equations, which are given in the Eulerian frame of reference.

Under the isotropy hypothesis, all the cosmological fluids must be perfect imposing  $q_\mu = \pi_{\mu\nu} = 0$ . In order to close the system, an equation of state relating the remaining fluids degrees of freedom is needed. Such equation for a fluid of relativistic particles is  $p = \frac{1}{3}\rho$ . It is customary to describe the cosmological properties of the radiation in the Universe using that equation of state. For a fluid of pressure-less matter (dust) it is simply  $p = 0$ .

The isotropy of the Universe also constrains all cosmological fluids to share the same rest frame. This is not true in the general case as we shall see when we deal with the spherical collapse. In homogeneous cosmology, it is helpful to work in a gauge in which the velocity of the Eulerian observer (the vector normal to every spatial hypersurface) is identical to the 4-velocity vector of all the fluids. In this particular case, it is allowed to write

$$\begin{aligned} E &= \rho , \\ S_{ij} &= p \gamma_{ij} . \end{aligned} \quad (2.41)$$

In order for the growth of the scale factor to be accelerated, one must have

$$(\rho + 3p) < 0 . \quad (2.42)$$

This is sometimes called a violation of the strong energy condition. Dust matter and radiation are thus not sufficient. Perhaps the easiest way to explain acceleration is to include a cosmological constant  $\Lambda$  in the Einstein equations. This is mathematically equivalent to including a fluid with stress-energy tensor  $T_{\mu\nu} = \Lambda g_{\mu\nu}$ . This has negative pressure satisfying the equation of state

$$p = -\rho . \quad (2.43)$$

The cosmological constant is sometimes understood as the result of the vacuum energy of the physical fields spread throughout space-time. However, it is well-known that a naive estimate of this vacuum energy density leads to a tremendous discrepancy compared with the value inferred from observation.

The alternative known as the *quintessence* scenario assumes that the missing energy is due to a new field with its own dynamics and is the object of the next section.

## 2.6 Cosmological scalar field

The simplest action for a scalar field minimally coupled to gravity is

$$S = - \int d^4x \sqrt{-g} \left( \frac{1}{2} (\nabla\phi)^2 + V(\phi) \right) . \quad (2.44)$$

The corresponding stress-energy tensor is

$$T_{\mu\nu} = \nabla_\mu\phi\nabla_\nu\phi - \frac{g_{\mu\nu}}{2} (\nabla_\alpha\phi\nabla^\alpha\phi + 2V(\phi)) . \quad (2.45)$$

The associated energy density and stress tensor read, using the general ADM metric

$$E = \frac{\dot{\phi}^2}{\alpha^2} + \frac{1}{2} (g^{\mu\nu} (\partial_\mu\phi)(\partial_\nu\phi) + 2V(\phi)) , \quad (2.46)$$

$$S_{\mu\nu} = D_\mu\phi D_\nu\phi - \frac{\gamma_{\mu\nu}}{2} (\nabla_\alpha\phi\nabla^\alpha\phi + 2V(\phi)) , \quad (2.47)$$

and the momentum density is

$$j_\mu = -\frac{\dot{\phi}}{\alpha} (\partial_\mu\phi) - n_\mu \frac{\dot{\phi}^2}{\alpha^2} . \quad (2.48)$$

We make use of the above expressions in the zero shift gauge ( $\beta_\mu = 0$ ) when we study the spherical collapse. For the time being, if we limit to the homogeneous case, the source terms greatly simplify and the complete system of coupled space-time dynamics with a scalar field gets written as

$$\frac{1}{\alpha^2} \frac{\dot{a}^2}{a^2} - \frac{k}{a^2} = \frac{8\pi}{3} \left( \frac{\dot{\phi}^2}{2\alpha^2} + V(\phi) \right) \quad (2.49)$$

$$-\frac{1}{\alpha^2} \frac{\ddot{a}}{a} + \frac{1}{\alpha^2} \frac{\dot{\alpha}}{\alpha} \frac{\dot{a}}{a} = \frac{8\pi}{3} \left( \frac{\dot{\phi}^2}{\alpha^2} - V(\phi) \right) . \quad (2.50)$$

The equation for the dynamics of  $\phi$  can either be obtained by combination of the two above equations and their derivatives or equivalently by directly varying the action of Eq. (2.44) with respect to  $\phi$ . The result is

$$\ddot{\phi} + 3\frac{\dot{a}}{a}\dot{\phi} - \frac{\dot{\alpha}}{\alpha}\dot{\phi} + \alpha^2 \frac{dV}{d\phi} = 0 . \quad (2.51)$$

This is usually referred to as the *Klein-Gordon equation*.

## 2.7 Acceleration with a scalar field

The condition of Eq. (2.42) gets translated, in terms of scalar fields, to  $V(\phi) > \dot{\phi}^2/\alpha^2$ . This is the *slow-roll condition*. In order to produce acceleration, the potential must have a flat region corresponding to an energy greater than its vacuum. The dynamics of the scalar field is then similar to that of a marble rolling down a gutter. As it goes down its potential, it loses energy due to the presence of the coupling terms proportional to  $\sim \dot{\phi}$  in Eq. (2.51). When the potential is nearly constant and dominates over the kinetic energy, its value acts as a cosmological constant driving de Sitter-like expansion. The slow-roll condition can be written more precisely without explicitly mentioning the scalar field.

In the study of de Sitter-like solutions, it is often useful to rewrite the value of the scale factor as  $a := a_i e^N$  where  $a_i$  is some initial value and  $N$  is the *number of e-fold* produced during expansion. There is a one-to-one correspondence between  $N$  and  $t$  defined through  $\frac{dN}{dt} = \frac{\dot{a}}{a} = H(t)$ .

The distance to the particle horizon is roughly given by the Hubble distance  $d_H = \frac{1}{H}$ . One defines the set of *Hubble Flow Parameters* as

$$\epsilon_0 := \frac{d_H}{d_H^i}, \quad \epsilon_{n+1} := \frac{d \ln |\epsilon_n|}{dN}, \quad (2.52)$$

where the  $d_H^i$  is some initial value of the Hubble distance. Exponential expansion is realised when

$$\epsilon_n \ll 1, \quad \forall n. \quad (2.53)$$

This implies our previous condition of the slow-roll condition. One sees this by considering the first two Hubble flow parameters

$$\epsilon_1 = -\frac{\dot{H}}{H^2}, \quad (2.54)$$

$$\epsilon_2 = \frac{1}{H} \frac{\ddot{H}}{\dot{H}} - 2 \frac{\dot{H}}{H^2}. \quad (2.55)$$

Without loss of generality, we set the lapse  $\alpha = 1$  (synchronous gauge). Equation (2.54) then gives,

$$\begin{aligned} -\dot{H} &\ll H^2 \\ 16\pi \frac{\dot{\phi}^2}{2} &\ll \frac{16\pi}{3} \left( \frac{\dot{\phi}^2}{2} + V(\phi) \right) \\ \dot{\phi}^2 &\ll V(\phi). \end{aligned} \quad (2.56)$$

Thus  $H^2 \sim \frac{8\pi}{3} V(\phi)$ . Equation (2.55) gives

$$\frac{\ddot{\phi}}{\dot{\phi}} \frac{1}{H} \ll 1. \quad (2.57)$$

Plugging this in the evolution equation for the scalar field yields

$$\dot{\phi} \sim -\frac{1}{3H} \frac{dV}{d\phi}. \quad (2.58)$$

This can be used to express the first two Hubble flow parameters as

$$\epsilon_1 \sim \frac{1}{16\pi} \frac{V_{,\phi}^2}{V(\phi)^2} \quad (2.59a)$$

$$\epsilon_2 \sim \frac{4}{16\pi} \left( \frac{V_{,\phi\phi}}{V(\phi)} - \frac{V_{,\phi}^2}{V(\phi)^2} \right) \quad (2.59b)$$

with  $V_{,\phi} := \frac{dV}{d\phi}$  and  $V_{,\phi\phi} := \frac{d^2V}{d\phi^2}$ . The above definitions are usually invoked in the context of inflation yet these are also helpful in the study of Dark Energy in the context of late-time expansion. We postpone a more detailed study of inflation. And now turn to the problem of solving the dynamics of space-time numerically.

## 2.8 Numerical treatment

The ADM equations are not the unique equations suited to the study of the dynamics of space-time. There are a number of possible schemes all analytically equivalent yet each with specific mathematical properties appealing to the “numerist”. It is customary to classify these schemes as *constrained* and *unconstrained* based upon whether these make use of the constraint equations explicitly in the evolution equations. The ADM formulation is a kind of unconstrained scheme. The constraint equations are simply used to monitor the numerical error throughout the integration. However how useful this formalism is for analytical studies, it suffers from numerical instability issues that lead the numerist to favour other formalisms.

Arguably the most important properties of a numerical scheme are those of *well-posedness* and *hyperbolicity*<sup>(4)</sup>. We now provide a necessarily short introduction to these properties. More information will be found in the textbooks by Alcubierre (Alcubierre 2008) and Baumgarte & Shapiro (Baumgarte and Shapiro 2010).

Consider a first order system of the form

$$\partial_t \vec{u} + M^i \partial_i \vec{u} = \vec{s}, \quad (2.60)$$

it is said to be well-posed if there exist a norm  $\|\cdot\|$  and real parameters  $\alpha$  and  $k$  **independent of the initial data** such that

$$\|\vec{u}(t, x^i)\| \leq k e^{\alpha t} \|\vec{u}(0, x^i)\|. \quad (2.61)$$

---

<sup>(4)</sup>The term *hyperbolicity* is employed here to express that the system of equations behaves as a generalised wave equation. The word is used in a context different yet intuitively related to its use in the classification of second-order partial differential equations.

Depending on the shape and values of  $M^i$ , the system can be *strongly*, *weakly* or *symmetric hyperbolic*, the latter implying the former. The ADM system is only weakly hyperbolic except on very special exceptions which makes it less stable than a strongly hyperbolic one. The alternative preferred by many authors is the formalism known as *BSSN* (Nakamura, Oohara and Kojima 1987, Shibata 1995, Baumgarte and Shapiro 1998).

This is another unconstrained evolution scheme which we use for numerical evolutions in the present work. The general description that we give in the next section is later adapted to spherical symmetry in the next chapter.

## 2.9 The BSSN formulation

One defines the conformal metric as

$$\tilde{\gamma}_{ij} := \psi^{-4} \gamma_{ij}, \quad (2.62)$$

with  $\tilde{\gamma} := \det(\gamma_{\mu\nu}) = 1$ . The evolution equation for the determinant of the metric  $\gamma$  then implies

$$\partial_t \psi = -\frac{1}{6} \psi (\alpha K - \partial_i \beta^i) + \beta^i \partial_i \psi. \quad (2.63)$$

The extrinsic curvature is split into its trace and traceless parts.

$$K_{ij} = \frac{1}{3} \gamma_{ij} K + A_{ij}. \quad (2.64)$$

One defines  $\tilde{A}_{ij} := \psi^{-4} A_{ij}$ . The constraint equations become

$$\mathcal{H} := R^{(3)} - \tilde{A}_{ij} \tilde{A}^{ij} + \frac{2}{3} K^2 - 16\pi E = 0 \quad (2.65)$$

$$\mathcal{M} := \partial_j \tilde{A}^{ij} + \tilde{\Gamma}_{jk}^i \tilde{A}^{jk} + 6\tilde{A}^{ij} \frac{\partial_j \psi}{\psi} - \frac{2}{3} \tilde{\gamma}^{ij} \partial_j K - 8\pi \tilde{j}^i = 0 \quad (2.66)$$

The crucial change in the BSSN formulation compared to ADM lies in the addition of the conformal connection which is evolved as an independent variable.

$$\tilde{\Gamma}^i := \tilde{\gamma}^{jk} \tilde{\Gamma}_{jk}^i = -\partial_j \tilde{\gamma}^{ij}, \quad (2.67)$$

the evolution equation for this quantity being

$$\partial_t \tilde{\Gamma}^i - \mathcal{L}_\beta \tilde{\Gamma}^i = \tilde{\gamma}^{jk} \partial_j \partial_k \beta^i + \frac{1}{3} \tilde{\gamma}^{ij} \partial_j \partial_k \beta^k - 2 \left( \alpha \partial_j \tilde{A}^{ij} + \tilde{A}^{ij} \partial_j \alpha \right). \quad (2.68)$$

Including this in the set of evolution equations renders the system strongly unstable but it can be made strongly hyperbolic by adding a multiple of the momentum constraint (Alcubierre 2008, Baumgarte and Shapiro 2010):

$$\begin{aligned} \partial_t \tilde{\Gamma}^i - \mathcal{L}_\beta \tilde{\Gamma}^i &= \tilde{\gamma}^{jk} \partial_j \partial_k \beta^i + \frac{1}{3} \tilde{\gamma}^{ij} \partial_j \partial_k \beta^k - 2 \left( \alpha \partial_j \tilde{A}^{ij} + \tilde{A}^{ij} \partial_j \alpha \right) \\ &+ 2\alpha \xi \left[ \partial_j \tilde{A}^{ij} + \tilde{\Gamma}_{jk}^i \tilde{A}^{jk} + 6\tilde{A}^{ij} \frac{\partial_j \psi}{\psi} - \frac{2}{3} \tilde{\gamma}^{ij} \partial_j K - 8\pi \tilde{j}^i \right], \end{aligned} \quad (2.69)$$

with the requirement that  $\xi > \frac{1}{2}$ . The remaining evolution equations are derived from the ADM equations.

$$\partial_t \tilde{\gamma}_{ij} - \mathcal{L}_\beta \tilde{\gamma}_{ij} = -2\alpha \tilde{A}_{ij} \quad (2.70)$$

$$\begin{aligned} \partial_t \tilde{A}_{ij} - \mathcal{L}_\beta \tilde{A}_{ij} = \psi^{-4} \{ & -D_i D_j \alpha + \alpha R_{ij} + 4\pi\alpha [\gamma_{ij}(S - E) - 2S_{ij}] \}^{\text{TF}} \\ & \alpha (K \tilde{A}_{ij} - 2\tilde{A}_{ik} \tilde{A}_j^k) \end{aligned} \quad (2.71)$$

$$\partial_t K - \mathcal{L}_\beta K = -D_i D^i \alpha + \alpha \left( \tilde{A}_{ij} \tilde{A}^{ij} + \frac{1}{3} K^2 \right) + 4\pi\alpha (E + S), \quad (2.72)$$

where we have used the Hamiltonian constraint to eliminate the 3-Ricci scalar. The superscript “TF” denotes the *Trace-Free* part.

The great stability of the BSSN can be traced back to the evolution of the constraint on the numerical grid. It can be proved that the time derivative of the constraint equations  $\partial_t \mathcal{H}$  and  $\partial_t \mathcal{M}$  are non-zero and that the violation of the constraint is *swept* outside of the numerical domain (Baumgarte and Shapiro 2010). This is not the case in the ADM formalism where one has  $\partial_t \mathcal{H} = \partial_t \mathcal{M} = 0$ . The two systems are analytically equivalent.

In the following chapters, we make use of the ADM for the study of cosmological perturbations following inflation and we write the ADM and BSSN systems in spherical coordinates as we treat the problem of cosmological spherical collapse.



## Chapter 3

# Large Field Hybrid Inflation

The detailed study of the CMB anisotropies de-correlated from the foreground distortions due to the various effects happening after the time of recombination allows to draw important conclusions regarding the state of our Universe at the time of last scattering. The temperature anisotropies are produced by small perturbations in the metric of the primordial space-time, the spatial distribution of which depends on the physics of inflation and are studied mathematically as small departures from the de Sitter solution.

There is a number of ways to proceed with the analysis of cosmological perturbations. As we reckon it will contribute to join together the two subjects of this thesis otherwise relatively distant, we follow Maldacena (Maldacena 2003), and study the perturbations around the de Sitter spacetime in the ADM formalism. We then expose our contribution to the development of the model of Hybrid Inflation as we present how it can produce a large tensor to scalar ratio for large values of the field.

### 3.1 Inflationary perturbation

In presence of a single scalar field minimally coupled to gravity, the action is

$$S = \int d^4x \sqrt{-g} \left( \frac{R}{16\pi} - \frac{1}{2}(\nabla\phi)^2 - V(\phi) \right) . \quad (3.1)$$

We write the metric ansatz as

$$ds^2 = (-\alpha^2 + \beta^i \beta_i) dt^2 + 2\beta_i dt dx^i + \gamma_{ij} dx^i dx^j , \quad (3.2)$$

and proceed to write the action of Eq. (3.1) in the ADM formalism.

### 3.1.1 ADM action

The projection of the Einstein tensor onto the normal vector gives

$$n^\mu n^\nu G_{\mu\nu} = n^\mu n^\nu R_{\mu\nu} + \frac{1}{2}R. \quad (3.3)$$

Using the Gauss-Codazzi equation (2.18), one finds that the 4-Ricci scalar can be decomposed as

$$R = {}^{(3)}R + K_{\mu\nu}K^{\mu\nu} - K^2 - 2\nabla_\lambda(n^\nu\nabla_\nu n^\lambda - n^\lambda\nabla_\nu n^\nu). \quad (3.4)$$

We want to inject this back in Eq. (3.1). The exact value of the action does not concern us as we are merely interested in the result of its variation. Boundary terms such as produced after integration of gradient terms similar to the last of Eq. (3.4) can thus be discarded for our purpose. After rewriting the scalar part, Eq. (3.1) reads

$$S = \int dt \int d^3x \alpha \sqrt{\gamma} \left[ \frac{1}{16\pi} ({}^{(3)}R + K_{\mu\nu}K^{\mu\nu} - K^2) + \frac{1}{2\alpha^2} (\dot{\phi} - \beta^\mu(\partial_\mu\phi))^2 - \frac{\gamma^{\mu\nu}}{2} (\partial_\mu\phi)(\partial_\nu\phi) - V(\phi) \right]. \quad (3.5)$$

This includes no time derivative of the lapse and shift functions. This illustrates how the Einstein equations derived from the action (3.5) are really a set of constrained differential equations. The constraints are found by varying the action with respect to  $\alpha$  and  $\beta^i$  which act as Lagrange multipliers.

### 3.1.2 Constraint equations

The Hamiltonian constraint reads<sup>(1)</sup>

$$\begin{aligned} \frac{\delta S}{\delta \alpha} &= 0 \\ \Leftrightarrow \frac{1}{16\pi} ({}^{(3)}R - K_{\mu\nu}K^{\mu\nu} + K^2) - \frac{1}{2\alpha^2} (\dot{\phi} - \beta^i(\partial_i\phi))^2 - \frac{\gamma^{ij}}{2} (\partial_i\phi)(\partial_j\phi) - V(\phi) &= 0. \end{aligned} \quad (3.6)$$

In order to compute the momentum constraint, one needs

$$\begin{aligned} \frac{\partial}{\partial \beta^i} (K_{kj}K^{kj}) &= 2K_{kj} \frac{\partial}{\partial \beta^i} (K^{kj}), \\ \frac{\partial}{\partial \beta^i} (K^2) &= 2\gamma_{jk}K \frac{\partial}{\partial \beta^i} (K^{kj}). \end{aligned} \quad (3.7)$$

---

<sup>(1)</sup>Remembering that  $K_{\mu\nu}$  is proportional to  $\alpha^{-1}$ .

So that

$$\begin{aligned}
\frac{\partial}{\partial \beta^i} (K_{kj} K^{kj} - K^2) &= \frac{1}{\alpha} (K_{kj} - \gamma_{kj} K) \frac{\partial}{\partial \beta^i} (D^k \beta^j + D^j \beta^k) \\
&= \frac{2}{\alpha} (K_{kj} - \gamma_{kj} K) D^k \left( \frac{\partial}{\partial \beta^i} \beta^j \right) \\
&\text{“} = \text{”} \frac{2}{\alpha} D^j (K_{ij} - \gamma_{ij} K) ,
\end{aligned} \tag{3.8}$$

where we have neglected a total derivative in the last step. The Momentum constraint then reads

$$\begin{aligned}
\frac{\delta S}{\delta \beta^i} &= 0 \\
\leftrightarrow D^j (K_{ij} - \gamma_{ij} K) &= \frac{8\pi}{\alpha} (\dot{\phi} - \beta^i (\partial_i \phi)) (\partial_i \phi) .
\end{aligned} \tag{3.9}$$

The freedom of choice of coordinates on the perturbed manifold leads to an ambiguity in the identification of its events with those of the unperturbed manifold.

### 3.1.3 Fixing a gauge

Consider a general linearised coordinate transformation :

$$x^\mu \rightarrow x^\mu + \xi^\mu, \tag{3.10}$$

with  $\xi^\mu = (\xi^0, D^i L + L_T^i)$  and  $D_i L_T^i = 0$ . Aside from the intrinsic two tensorial graviton degrees of freedom, the action in general coordinates has two scalar and two vector degrees of freedom. These are excited when gravity is coupled to other energy fields. Fixing a gauge suppresses the remaining unphysical degrees of freedom.

As we are considering inflation driven by one scalar field only, the action Eq. (3.5) has 2 tensorial and 1 scalar physical degrees of freedom.

In the following section, we work in the gauge of coordinates comoving with the scalar field perturbations, that is  $\delta\phi = 0$ . We parametrise the perturbed 3-metric as

$$\gamma_{ij} \sim a^2 [(1 + 2\zeta)\delta_{ij} + h_{ij}] . \tag{3.11}$$

Requiring  $\partial_i h_{ij} = 0$  and  $h_{ii} = 0$  separates the scalar and tensorial degrees of freedom and ensures that the gravitational part of the action remains transverse.

### 3.1.4 Perturbative action

The derivation of the inflationary perturbations proceeds by expanding Eq. (3.5) in powers of the perturbation parameters  $\zeta$  and  $h_{ij}$ . One then solves for  $\alpha$  and

$\beta^i$  by evaluating the constraints Eq. (3.6) and Eq. (3.9) perturbatively in powers of  $\zeta$  and  $h_{ij}$ .

In order to write the action up to third order in the perturbations, one only needs to solve for the lapse and shift to first order (Maldacena 2003). A complete proof of this is given in Chen et al. (Chen, Huang, Kachru and Shiu 2007). We write the lapse and shift as

$$\alpha := \alpha^{(0)} + \alpha^{(1)} + \alpha^{(2)} + \dots \quad (3.12)$$

$$\beta_i := \beta_i^{(0)} + \beta_i^{(1)} + \beta_i^{(2)} + \dots \quad (3.13)$$

$$\text{with } \beta_i^{(n)} = \partial_i \psi^{(n)} + \beta_i^{\text{T}(n)} \text{ and } \partial_i \beta_{\text{T}}^i{}^{(n)} = 0 .$$

The quantities  $\alpha^{(n)}$  and  $\beta_i^{(n)}$  are  $n^{\text{th}}$ -order in the perturbation parameters. To zeroth order, the Universe is the unperturbed de Sitter space-time which satisfies  ${}^{(3)}R = 0$ . One has  $\alpha^{(0)} = 1$  and  $\beta_i^{(0)} = 0$ . The momentum constraint is identical to zero and the Hamiltonian constraint turns out to be the Friedmann equation:

$$\frac{6}{16\pi} \left( \frac{\dot{a}}{a} \right)^2 = \frac{1}{2} \dot{\phi}^2 + V(\phi) . \quad (3.14)$$

At all orders, the scalar, vector and tensor perturbations decouple as a result of the decomposition theorem (Dodelson 2003). We treat the scalar perturbations in details. The similar treatment for tensor perturbations can be found sketched out in Maldacena (Maldacena 2003). We merely quote the results given therein

### 3.1.5 Scalar perturbations

The connection coefficients of the 3-metric for scalar perturbations read

$$\Gamma_{ij}^k = \delta^{kl} (\partial_j \zeta \delta_{il} + \partial_i \zeta \delta_{jl} - \partial_l \zeta \delta_{ij}) . \quad (3.15)$$

This is used to compute the 3-Ricci scalar

$$\begin{aligned} {}^{(3)}R &:= \gamma^{ij} (\partial_k \Gamma_{ij}^k - \partial_j \Gamma_{ik}^k + \Gamma_{ij}^l \Gamma_{kl}^k - \Gamma_{ik}^l \Gamma_{jl}^k) \\ &= -2a^{-2} e^{-2\zeta} \delta^{ij} (2\partial_i \partial_j \zeta + (\partial_i \zeta)^2) , \end{aligned} \quad (3.16)$$

and the extrinsic curvature

$$\begin{aligned} \alpha K_{ij} &= -a^2 e^{2\zeta} (H + \dot{\zeta}) \delta_{ij} + \frac{1}{2} (D_i \beta_j + D_j \beta_i) \\ &= -a^2 e^{2\zeta} (H + \dot{\zeta}) \delta_{ij} + \frac{1}{2} (\partial_i \beta_j + \partial_j \beta_i) - ((\partial_j \zeta) \beta_i + (\partial_i \zeta) \beta_j - (\partial_k \zeta) \beta_k \delta_{ij}) . \end{aligned} \quad (3.17)$$

The trace of the extrinsic curvature reads

$$\alpha K = -3(H + \dot{\zeta}) + a^{-2} e^{-2\zeta} (\partial_i \beta_i + (\partial_i \zeta) \beta_i) . \quad (3.18)$$

Using this, the combination in the second term of the action reads

$$\begin{aligned} & \alpha^2(K_{ij}K^{ij} - K^2) = -6(H + \dot{\zeta})^2 + 4a^{-2}e^{-2\zeta}(H + \dot{\zeta})(\partial_i\beta_i + (\partial_i)\beta_i) \\ & + a^{-4}e^{-4\zeta} \left[ -(\partial_i\beta_i)^2 - 2(\partial_i\dot{\zeta})^2\beta_i^2 + \left( \frac{1}{2}(\partial_i\beta_j + \partial_j\beta_i) - ((\partial_j\dot{\zeta})\beta_i + (\partial_i\dot{\zeta})\beta_j) \right)^2 \right]. \end{aligned} \quad (3.19)$$

The solution for the lapse and shift are computed by solving the constraints after injection of the previous results. To first order, the momentum constraint reads

$$\begin{aligned} & D_j(K_i^j - \gamma_i^j K) = 0 \\ & \leftrightarrow D_j \left( \frac{1}{\alpha} \left( 2(H + \dot{\zeta})\delta_i^j + \frac{1}{2}a^{-2}(\partial_i\beta_k + \partial_k\beta_i)\delta^{kj} - a^{-2}(\partial_k\beta_k)\delta_i^j \right) \right) = 0 \\ & \leftrightarrow D_j \left( \frac{2}{\alpha}(H + \dot{\zeta}) \right) = 0, \end{aligned} \quad (3.20)$$

the solution of which is

$$\alpha^{(1)} = \frac{\dot{\zeta}}{H}. \quad (3.21)$$

The first order Hamiltonian constraint is equivalent to

$$\begin{aligned} & -2a^{-2}e^{-2\zeta} (2\partial_i\partial_i\dot{\zeta} + (\partial_i\dot{\zeta})^2) + \frac{6}{\alpha^2}(H + \dot{\zeta}) \\ & - \frac{4}{\alpha^2}a^{-2}e^{-2\zeta}(H + \dot{\zeta})\partial_i\beta_i = 16\pi \left( \frac{\dot{\phi}^2}{2\alpha^2} + V(\phi) \right). \end{aligned} \quad (3.22)$$

Using Eq. (3.21) as well as the zeroth order constraint (Friedmann equation) one has

$$4a^{-2}(\partial\partial_i\dot{\zeta}) + 4a^{-2}H\partial_i\beta_i = -16\pi\frac{\dot{\phi}^2\dot{\zeta}}{H^2}. \quad (3.23)$$

The solution for the shift is thus

$$\begin{aligned} \beta_i^{(1)} &= \partial_i\psi & \text{with } \psi &= -\frac{\zeta}{H} + \chi \\ & & \text{and } \partial_i\partial_i\chi &= 4\pi a^2 \frac{\dot{\phi}^2}{H^2} \dot{\zeta}. \end{aligned} \quad (3.24)$$

These can now be plugged in the expression of the action. Using Eq. (3.21) and Eq. (3.24) and disregarding a total derivative linear in  $\psi$ , Eq. (3.5) becomes

$$\begin{aligned} S &= \int d^4x \left[ \frac{ae^\zeta}{16\pi} \left( 1 + \frac{\dot{\zeta}}{H} \right) (-4\partial_i\partial_i\dot{\zeta} - 2(\partial_i\dot{\zeta})^2 - 16\pi V(\phi)a^2e^{2\zeta}) \right. \\ & \quad \left. + \frac{a^3e^{3\zeta}}{16\pi \left( 1 + \frac{\dot{\zeta}}{H} \right)} \left( -6(H + \dot{\zeta})^2 + 16\pi \frac{\dot{\phi}^2}{2} \right) \right]. \end{aligned} \quad (3.25)$$

Expanding the denominator and disregarding the terms higher than second order, one finds

$$\begin{aligned}
S = \int d^4x \left[ \frac{ae^\zeta}{16\pi} \left( 1 + \frac{\dot{\zeta}}{H} \right) (-4\partial_i\partial_i\zeta - 2(\partial_i\zeta)^2) + a^3 e^{3\zeta} \left( \frac{\dot{\phi}^2}{2} - V(\phi) \right) \right. \\
\left. + a^3 e^{3\zeta} \frac{\dot{\zeta}^2}{H^2} \frac{\dot{\phi}^2}{2} - \frac{6}{16\pi} a^3 e^{3\zeta} H^2 - \frac{12}{16\pi} a^3 e^{3\zeta} H^2 \frac{\dot{\zeta}}{H} \right. \\
\left. - a^3 e^{3\zeta} \frac{\dot{\zeta}}{H} \left( \frac{\dot{\phi}^2}{2} + V(\phi) \right) + \frac{6}{16\pi} a^3 e^{3\zeta} H^2 \frac{\dot{\zeta}}{H} \right]. \quad (3.26)
\end{aligned}$$

The last two terms cancel by virtue of the Friedmann equation. Now,

$$\begin{aligned}
\frac{\dot{\phi}^2}{2} - V(\phi) &= \frac{6}{16\pi} H^2 - 2V(\phi) \\
\text{and } \frac{6}{16\pi} \left( \frac{2}{3} \dot{H} + 2H^2 \right) &= 2V(\phi). \quad (3.27)
\end{aligned}$$

This leaves us with

$$\begin{aligned}
S = \int d^4x \left[ \frac{ae^\zeta}{16\pi} \left( 1 + \frac{\dot{\zeta}}{H} \right) (-4\partial_i\partial_i\zeta - 2(\partial_i\zeta)^2) - \frac{12}{16\pi} a^3 e^{3\zeta} H^2 \right. \\
\left. - \frac{6}{16\pi} \frac{2}{3} \dot{H} a^3 e^{3\zeta} + a^3 e^{3\zeta} \frac{\dot{\phi}^2}{2} \frac{\dot{\zeta}^2}{H^2} - \frac{12}{16\pi} a^3 e^{3\zeta} H^2 \frac{\dot{\zeta}}{H} \right]. \quad (3.28)
\end{aligned}$$

One then uses

$$-\frac{6}{16\pi} \frac{2}{3} \dot{H} a^3 e^{3\zeta} = \frac{-6}{16\pi} \frac{2}{3} \frac{d}{dt} (H a^3 e^{3\zeta}) + \frac{12}{16\pi} H^2 a^3 e^{3\zeta} + \frac{12}{16\pi} H^2 \frac{\dot{\zeta}}{H} a^3 e^{3\zeta}, \quad (3.29)$$

to cancel two terms. Moreover,

$$\begin{aligned}
\frac{d}{dt} \left( \frac{ae^\zeta}{H} (-4\partial_i\partial_i\zeta) \right) &= \frac{\dot{\zeta}ae^\zeta}{H} (-4\partial_i\partial_i\zeta) - ae^\zeta \frac{\dot{H}}{H^2} (-4\partial_i\partial_i\zeta) \\
&\quad - 4 \frac{ae^\zeta}{H} (\partial_i\partial_i\zeta) - 4ae^\zeta (\partial_i\partial_i\zeta), \quad (3.30)
\end{aligned}$$

and

$$\begin{aligned}
\frac{d}{dt} \left( -2 \frac{ae^\zeta}{H} (\partial_i\zeta)^2 \right) &= -2 \frac{\dot{\zeta}ae^\zeta}{H} (\partial_i\zeta)^2 + 2 \frac{ae^\zeta \dot{H}}{H^2} (\partial_i\zeta)^2 \\
&\quad - 4 \frac{ae^\zeta}{H} (\partial_i\zeta) (\partial_i\dot{\zeta}) - 2ae^\zeta (\partial_i\zeta)^2. \quad (3.31)
\end{aligned}$$

Plugging all these in the action and disregarding the total time derivatives, one ends up with

$$S = \int d^4x \left[ \frac{ae^\zeta}{16\pi} \frac{\dot{H}}{H^2} (-4\partial_i\partial_i\zeta - 2(\partial_i\zeta)^2) + \frac{4}{16\pi} \frac{ae^\zeta}{H} \left( (\partial_i\partial_i\dot{\zeta}) + (\partial_i\zeta)(\partial_i\dot{\zeta}) \right) + a^3 e^{3\zeta} \frac{\dot{\zeta}^2}{H^2} \frac{\dot{\phi}^2}{2} \right]. \quad (3.32)$$

This can be expressed in the form

$$S = \int d^4x \left[ \frac{a}{16\pi} \frac{\dot{H}}{H^2} (-4\partial_i(e^\zeta\partial_i\zeta) + 2e^\zeta(\partial_i\zeta)^2) + \frac{4}{16\pi} \frac{a}{H} \partial_i(e^\zeta(\partial_i\dot{\zeta})) + a^3 e^{3\zeta} \frac{\dot{\zeta}^2}{H^2} \frac{\dot{\phi}^2}{2} \right]. \quad (3.33)$$

The first and third terms can be disregarded as total spatial derivatives. From the background equations, one has  $-\frac{\dot{H}}{H^2} = 8\pi \frac{\dot{\phi}^2}{2H^2}$  so that, up to second order,

$$S = \frac{1}{2} \int d^4x \frac{\dot{\phi}^2}{H^2} \left[ a^3 \dot{\zeta}^2 - a(\partial_i\zeta)^2 \right] = \frac{1}{8\pi} \int d^4x \epsilon_1 \left[ a^3 \dot{\zeta}^2 - a(\partial_i\zeta)^2 \right] \quad (3.34)$$

in agreement with Maldacena (Maldacena 2003). The action to second order in the perturbation is thus suppressed by a factor equal to the first Hubble flow parameter (see Sec. 2.7). In case the Universe is de Sitter, this factor is zero and the action for the perturbations vanishes.

It is believed that the structures observed today originated from quantum fluctuations in the early inflationary Universe. The action Eq. (3.34) serves as the starting point for the quantisation of the cosmological perturbations. The dynamics it describes is best understood in the conformal time coordinate  $\eta$  defined as  $dt = a d\eta$ . One has,

$$S = \frac{1}{8\pi} \int d\eta \int d^3x \epsilon_1 \left[ a^2 \zeta'^2 - a^2 (\partial_i\zeta)^2 \right], \quad (3.35)$$

with a primed quantity denoting its derivative with respect to the conformal time. It is customary to set  $v = -a\zeta\sqrt{2\epsilon_1} = -z\zeta$ . The action then reads, disregarding one total conformal time derivative,

$$S = \frac{1}{16\pi} \int d\eta \int d^3x \left( v'^2 - (\partial_i v)^2 + \frac{z''}{z} v^2 \right). \quad (3.36)$$

This is known as the *Mukhanov-Sasaki action* and is the action of a parametric oscillator. The equation of motion is best analysed in Fourier space after defining  $v = 1/(2\pi)^{3/2} \int d^3\vec{k} v_k(\eta) e^{i\vec{k}\cdot\vec{x}}$

$$v_k'' + \left(k^2 - \frac{z''}{z}\right) v_k = 0, \quad (3.37)$$

with  $\vec{k}$  labelling the Fourier modes in free-fall with inflation.<sup>(2)</sup> The frequency of each oscillator is identified as  $\omega_k^2 := \left(k^2 - \frac{z''}{z}\right)$ .

Quantisation proceeds by solving the equation of motion Eq. (3.37) for  $v_k$  and then promoting  $v$  to a quantum operator in the Heisenberg picture

$$\hat{v}(\vec{x}, \eta) = \frac{1}{(2\pi)^{3/2}} \int d^3\vec{k} \left( v_k e^{i\vec{k}\cdot\vec{x}} \hat{a}_k + v_k^\dagger e^{-i\vec{k}\cdot\vec{x}} \hat{a}_k^\dagger \right). \quad (3.38)$$

The operators  $\hat{a}_k^\dagger$  and  $\hat{a}_k$  are respectively the creation and annihilation operators satisfying

$$\begin{aligned} [\hat{a}_k, \hat{a}_{k'}] &= [\hat{a}_k^\dagger, \hat{a}_{k'}^\dagger] = 0 \\ [\hat{a}_k, \hat{a}_{k'}^\dagger] &= \delta^{(3)}(\vec{k} - \vec{k}'). \end{aligned} \quad (3.39)$$

The vacuum  $|0\rangle$  is a state defined by

$$\hat{a}_k |0\rangle = 0. \quad (3.40)$$

To leading order in the Hubble-flow parameters, one has

$$\frac{z''}{z} = 2a^2 H^2 (1 + \mathcal{O}(\epsilon)). \quad (3.41)$$

In the limit  $k \gg aH$ , that is, for modes of a scale much smaller than the horizon, the solution to (3.37) reads

$$\lim_{\frac{k}{aH} \rightarrow +\infty} v_k(\eta) = \frac{e^{-ik\eta}}{\sqrt{2k}}. \quad (3.42)$$

This defines the Bunch-Davies vacuum<sup>(3)</sup>. As all the physically observable modes are small on the onset of inflation, the above solution serves as initial conditions for the curvature perturbations in the primordial Universe.

<sup>(2)</sup>we do not use the vector notation  $\vec{k}$  when it appears as a subscript.

<sup>(3)</sup>The vacuum state of a curved space-time has no unique definition. This is related to the time-dependence of the mode frequencies and thus of the state of minimum energy. The Bunch Davies vacuum is time independent and corresponds to the vacuum in the far past ( $\eta \rightarrow -\infty$ ) at which time the modes are all deep within the horizon and the frequencies are all time-independent (Mukhanov and Winitzki 2007).

In the de Sitter limit, one has  $a(\eta) = -1/H\eta$  and, to first order in the slow-roll, Eq. (3.37) reads

$$v_k'' + \left(k^2 - \frac{2}{\eta^2}\right) v_k = 0. \quad (3.43)$$

This has the general solution

$$v_k = A \frac{e^{-ik\eta}}{\sqrt{2k}} \left(1 - \frac{i}{k\eta}\right) + B \frac{e^{-ik\eta}}{\sqrt{2k}} \left(1 + \frac{i}{k\eta}\right). \quad (3.44)$$

In order to reconcile this with the solution in the sub-horizon limit, one imposes  $A = 1$  and  $B = 0$ . Thus,

$$v_k = \frac{e^{-ik\eta}}{\sqrt{2k}} \left(1 - \frac{i}{k\eta}\right). \quad (3.45)$$

As a mode becomes bigger than the scale of the horizon, one has the limit solution

$$\lim_{\frac{k}{aH} \rightarrow 0} v_k = \frac{1}{i\sqrt{2k}} \frac{1}{k\eta}. \quad (3.46)$$

From this, and because  $v = -z\zeta$  the scalar perturbations associated to modes bigger than the horizon are constant:

$$\lim_{\frac{k}{aH} \rightarrow 0} \zeta = \text{cst}. \quad (3.47)$$

This makes  $\zeta$  a very interesting quantity. As it freezes out when leaving the Horizon, it retains useful informations about the primordial Universe which leave an imprint on the CMB picture as it goes back within the horizon after inflation.

The quantisation of the solution to second order action in the cosmological perturbations expressed as (3.36) allows to compute the two-point correlation function

$$\begin{aligned} \langle \hat{v}_k \hat{v}_{k'} \rangle &= \langle 0 | \hat{v}_k \hat{v}_{k'} | 0 \rangle \\ &= \langle 0 | (v_k(\eta) \hat{a}_k + v_{-k}^\dagger(\eta) \hat{a}_{-k}^\dagger) (v_{k'}(\eta) \hat{a}_{k'} + v_{-k'}(\eta)^\dagger \hat{a}_{-k'}^\dagger) | 0 \rangle \\ &= |v_k|^2 \langle 0 | [\hat{a}_k, \hat{a}_{-k'}] | 0 \rangle \\ &= |v_k|^2 \delta(\vec{k} + \vec{k}') \\ &:= P_v(k) \delta(\vec{k} + \vec{k}'). \end{aligned} \quad (3.48)$$

$P_v(k)$  is the *primordial power spectrum* of  $v_k$ . Comparison with the CMB data proceeds by choosing a pivot scale  $k_*$  and estimating the power spectrum for this scale when it leaves the horizon corresponding to  $k_* = a(\eta_*)H_*$ . This is known as the time of *horizon crossing*.

The exact solution to Eq. (3.37) can be expanded in power of the Hubble-Flow parameters around a pivot scale at the time of horizon crossing (Martin, Ringeval and Vennin 2013).

To zeroth order in the Hubble-flow parameters, Eq. (3.46) is valid as we are mostly interested in modes just entering the horizon. The power spectrum of the scalar curvature perturbations at the time of horizon crossing then reads

$$P_{\zeta_0}(k_*) = \frac{1}{z^2} P_{v_0} = \frac{1}{4k_*^3} \frac{H_*^2}{\epsilon_1^*}. \quad (3.49)$$

Note that, strictly speaking, the power spectrum in the de Sitter limit is exactly zero. The approximation used above is customarily referred to as the *quasi-de Sitter* limit. The dimension-less power spectrum defined as  $\mathcal{P}_\zeta(k) := k^3/2\pi^2 P_\zeta(k)$  reads

$$\mathcal{P}_{\zeta_0}(k_*) = \frac{H_*^2}{8\pi^2 \epsilon_{1*}}. \quad (3.50)$$

This can be expanded around the pivot scale as

$$\mathcal{P}_\zeta(k) = \mathcal{P}_{\zeta_0} \left[ a_0 + a_1 \ln \left( \frac{k}{k_*} \right) + \dots \right]. \quad (3.51)$$

To first order, the coefficients of the expansion read

$$a_0 = 1 - 2(C + 1)\epsilon_{1*} - C\epsilon_{2*} + \mathcal{O}(\epsilon^2) \quad (3.52)$$

$$a_1 = -2\epsilon_{1*} - \epsilon_{2*} + \mathcal{O}(\epsilon^2), \quad (3.53)$$

with  $C \equiv \gamma_E + \ln 2 - 2$  and  $\gamma_E$  is the Euler constant.

A Universe that is exactly de Sitter is scale invariant. That is, its power spectrum is proportional to  $\mathcal{P} \sim k^0$ . One measures the deviation from scale invariance using the scalar spectral index:

$$n_s - 1 := \frac{d \ln \mathcal{P}_\zeta(k)}{d \ln k}. \quad (3.54)$$

To first order in the slow-roll parameters, the scalar spectral index reads

$$n_s \sim 1 - 2\epsilon_{1*} - \epsilon_{2*}. \quad (3.55)$$

The most recent measurements of the spectral index favour values around  $n_s \sim 0.96$  (Ade et al. 2014b).

### 3.1.6 Tensor Perturbations

We now summarise the results on the tensor perturbations (Maldacena 2003). To second order in the perturbations, the action reads,

$$S = \frac{1}{16\pi} \int d\eta d^3x \frac{1}{4} \left[ a^3 (\dot{h}_{ij})^2 - a (\partial_k h_{ij})^2 \right]. \quad (3.56)$$

This is very similar, in shape, to Eq. (3.34), except that Eq. (3.56) is not suppressed by any Hubble-flow parameter. This is because the tensor modes of the unperturbed action Eq. (3.1) are responsible for the propagation of gravitational waves which are expected even without minimal coupling to any scalar field.

The quantisation proceeds in a similar way as for scalar perturbations by defining

$$h_{ij} = \frac{1}{(2\pi)^{3/2}} \int d^3k \sum_{s=\pm} \left( \epsilon_{ij}^s(k) h_k^s e^{i\vec{k}\cdot\vec{x}} \hat{a}_k + \epsilon_{ij}^{s*} h_k^{s\dagger} e^{-i\vec{k}\cdot\vec{x}} \hat{a}_k^\dagger \right), \quad (3.57)$$

with  $\hat{a}_k$  and  $\hat{a}_k^\dagger$  now being the annihilation and creation operators for the graviton. The sum runs over both polarisation of the gravitational field and the  $\epsilon_{ij}^s$  functions are orthonormal basis tensors satisfying  $\epsilon_{ii} = k^i \epsilon_{ij} = 0$  and  $\epsilon_{ij}^s(k) \epsilon_{ij}^{s'}(k) = 2\delta_{ss'}$ .

The dimensionless power spectrum to zeroth order reads

$$\mathcal{P}_{h_0} = \frac{2H_*^2}{\pi^2}. \quad (3.58)$$

The expansion around the pivot scale can be expressed in a way similar to Eq. (3.51) with

$$a_0 = 1 - 2(C+1)\epsilon_{1*} + \mathcal{O}(\epsilon^2) \quad (3.59)$$

$$a_1 = -2\epsilon_{1*} + \mathcal{O}(\epsilon^2), \quad (3.60)$$

Using this last result, one defines the tensor to scalar ratio

$$r := \frac{\mathcal{P}_{h_0}}{\mathcal{P}_{\zeta_0}}. \quad (3.61)$$

To first order, this reads

$$r \sim 16\epsilon_{1*}. \quad (3.62)$$

A direct measurement of the B-mode of polarisation of the CMB allows to infer the value of this last quantity and in turns the first Hubble-flow parameter (Seljak and Zaldarriaga 1997, Kamionkowski, Kosowsky and Stebbins 1997). This gives a direct indication on the shape of the inflationary potential.

The results of this section allow to relate the CMB observables directly to the dynamics of many models of inflation. In the remainder of this chapter, we apply these in the treatment of the Large Field Hybrid Model.

## 3.2 Large Field Hybrid Inflation

The aim of this part of the present work is to show how Hybrid Inflation at large values of the field can be reconciled with recent observations. In case the

signal recently measured by the BICEP2 (Ade et al. 2014a) experiment indeed turns out to be due to B-mode polarisation of the CMB<sup>(4)</sup>, it would favour the large field models of inflation as these naturally produce a large value of the tensor to scalar ratio.

Following the work presented previously in (Clesse and Requier 2014), we perform a statistical analysis of the Hybrid Inflation parameter space and confront it to both Planck data (Ade et al. 2014d, Ade et al. 2014c) and Planck+BICEP2 data. This is done by using a modified version of the COSMOMC package that we have coupled to our solving for the dynamics of the scalar field.

The hybrid inflation model can be embedded within many high energy frameworks such as supersymmetry (Binétruy and Dvali 1996, Clauwens and Jeannerot 2008, Kallosh and Linde 2003, Lazarides and Vamvasakis 2007) and supergravity (Halvø 1996, Binétruy, Dvali, Kallosh and Van Proeyen 2004), Grand-Unified-Theory (GUT) (Jeannerot, Rocher and Sakellariadou 2003, Rocher and Sakellariadou 2005), extra-dimensions (Fukuyama, Okada and Osaka 2008, Fairbairn, Lopez Honorez and Tytgat 2003) and string theory (Davis and Postma 2008, Brax et al. 2007). This makes it very-well motivated amongst the lot of inflation models. The description of these frameworks goes well beyond the scope of this work.

The original two-fields hybrid inflation potential reads

$$V(\phi, \psi) = \Lambda^4 \left[ \left(1 - \frac{\psi^2}{M^2}\right)^2 + \frac{\phi^2}{\mu^2} + \frac{2\phi^2\psi^2}{\phi_c^2 M^2} \right]. \quad (3.63)$$

The logarithm of this potential is shown on Fig. 3.1 for arbitrary values of the parameters. There is an almost flat valley in the direction  $\psi = 0$  which is an ideal region for slow-roll inflation. When  $\phi < \phi_c$ , the effective squared mass term of the  $\psi$  field is smaller than zero which leads to a fast decay of the solution toward either of the true minima of the potential  $(\phi, \psi) = (0, \pm M)$ . This is known as a *tachyonic instability*. The corresponding region of the potential is called the *waterfall phase*.

Along the valley, the effective one field potential is

$$V(\phi) = \Lambda^4 \left( 1 + \frac{\phi^2}{\mu^2} \right). \quad (3.64)$$

Inflation may occur in 3 different regions of the potential. i) For very large values of the field, the second term of Eq. (3.64) is dominant and the dynamics is similar to chaotic inflation with a simple massive potential. ii) For small values of  $\phi$ , the first term dominates and the potential is vacuum dominated. iii) It has been proved that the waterfall phase can be sufficiently mild to produce the necessary 60 e-folds of inflation (Clesse 2011). The observable predictions

---

<sup>(4)</sup>A recent joint analysis of the data from BICEP2, Keck Array and Planck has shown that the detection then claimed is strongly disfavoured as galactic dust seems to contribute more importantly to the signal than initially expected (Ade et al. 2015).

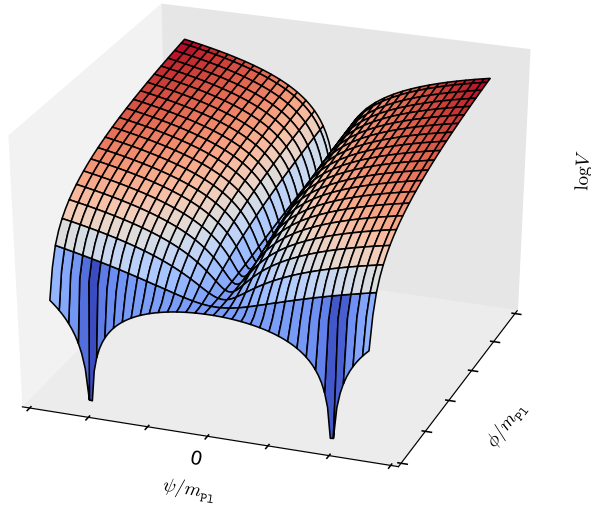


Figure 3.1 – Logarithm of the original two-fields hybrid potential. The almost flat valley lies in the direction  $\psi = 0$ .

are different in all three regions. We only consider the first two possibilities as the mild waterfall scenario produces a small value of the tensor to scalar ratio.

We work in natural units and reinsert the reduced Planck mass symbol  $M_{\text{pl}}$  explicitly in the equations.

### 3.3 Reheating parametrisation

The minimum number of e-folds produced during inflation depends both on the energy scale and the duration of the transition from inflationary to radiation dominated era called the *reheating phase*. Assuming that the Universe transits right into the radiation era requires that  $N_* = 60$ , this being the number of e-folds produced between the time of the horizon exit of the pivot scale and the end of inflation. This assumption can be softened by the following parametrisation.

The physical size of the pivot scale as it crosses the horizon is<sup>(5)</sup>

$$\begin{aligned} \frac{k_*}{a_*} &= \frac{k_*}{a_0} \frac{a_0}{a_{\text{end}}} \frac{a_{\text{end}}}{a_*} \\ &= \frac{k_*}{a_0} \left( \frac{\rho_{\text{end}}}{\rho_{\gamma 0}} \right)^{1/4} R_{\text{rad}}^{-1} e^{N_*} . \end{aligned} \quad (3.65)$$

<sup>(5)</sup>In what follows, the subscript “end” denotes the time of the end of inflation.

$R_{\text{rad}} = 1$  corresponds to instantaneous reheating. This parameter is part of the set due for statistical analysis.

Remark that the Reheating parameter,  $R_{\text{rad}}$  is related to the reheating energy density  $\rho_{\text{reh}}$  (Martin and Ringeval 2010) :

$$\ln R_{\text{rad}} = \frac{1 - 3\bar{w}_{\text{reh}}}{12(1 + w_{\text{reh}})} \ln \left( \frac{\rho_{\text{reh}}}{\rho_{\text{end}}} \right), \quad (3.66)$$

where  $w_{\text{reh}}$  is the mean equation of state of the reheating era. One then determines  $\rho_{\text{end}}$  by assuming  $w_{\text{reh}}$ . This is of limited use in this work as hybrid inflation proceeds in a phase of tachyonic reheating. The use of lattice simulation is required in order to approximate the equation of state parameter  $w_{\text{reh}}$  which goes well beyond the scope of this work.

### 3.4 The regimes of large field inflation

As we focus solely on regimes with a sharp waterfall phase, the slow-roll inflation parameters for the potential of Eq. (3.64) can be written

$$\epsilon_1^{\text{SR}} = \frac{2M_{\text{pl}}^2 \frac{\phi^2}{\mu^2}}{\mu^2 \left(1 + \frac{\phi^2}{\mu^2}\right)^2}, \quad (3.67a)$$

$$\epsilon_2^{\text{SR}} = \frac{4M_{\text{pl}}^2 \left(-1 + \frac{\phi^2}{\mu^2}\right)}{\mu^2 \left(1 + \frac{\phi^2}{\mu^2}\right)^2}. \quad (3.67b)$$

The best measured observable quantities at present are the amplitude and spectral index of the scalar perturbation spectrum. The former depends on both the scale of inflation  $\Lambda$  and on  $\mu$ . This fixes one parameter of the model while leaving complete freedom for the others. The spectral index  $n_s$  serves us to sort amongst the slow-roll regimes.

The Hubble-flow parameters are plotted on Fig. 3.2 and Fig. 3.3 for two values of  $\mu$ .  $\phi_c$  is kept very small so that it has no impact on the slow-roll evolution. A blue spectrum of scalar perturbations ( $n_s > 1$ ) is expected when inflation happens in the vacuum dominated regime since  $\epsilon_1 \ll 1$  and  $\epsilon_2 < 0$ . On the contrary, the spectrum is red ( $n_s < 1$ ) in the large field regime as  $\epsilon_1 \simeq 2M_{\text{pl}}^2/\phi^2$  and  $\epsilon_2 \simeq 4M_{\text{pl}}^2/\phi^2$ . This is similar to the case of a simple massive potential. For these reasons, the large field hybrid potential has long been regarded as an irrelevant candidate for inflation.

One would naively think that the vacuum dominated era always follows the large field regime leading to a blue spectrum not compatible with observation. As it turns out, for  $\mu \lesssim 1.6M_{\text{pl}}$ , the slow-roll conditions are violated at the end of the large field regime and the field acquires sufficient kinetic energy so that the vacuum dominated regime never occurs (Clesse and Rocher 2009). This leaves us with three possible regimes of inflation that produce a red spectrum which we now study in details.

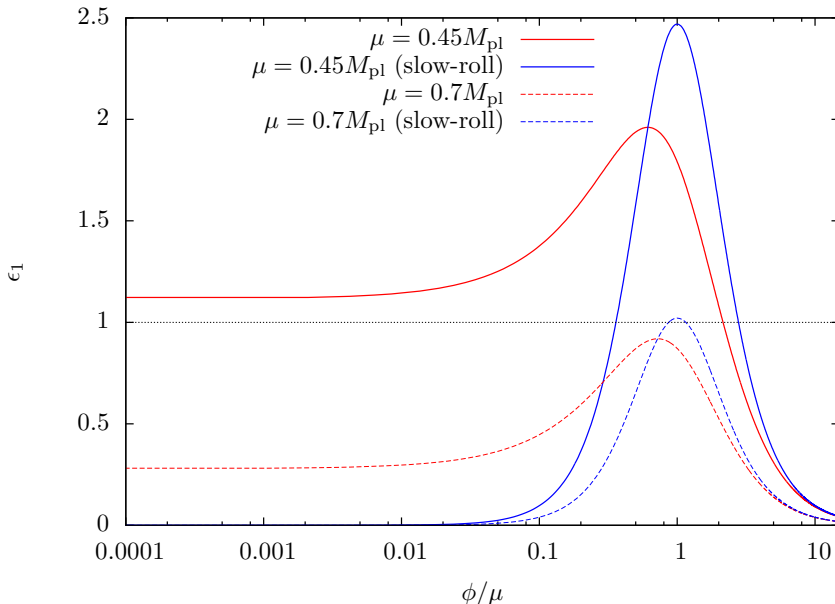


Figure 3.2 – Evolution of the first Hubble-flow parameter  $\epsilon_1$  as a function of  $\phi/\mu$ . The complete solution differs greatly from the slow-roll solution at small values of  $\mu$ .

### 3.4.1 Chaotic-like inflation: $\phi_c < \mu \ll \phi_*$ and $\mu < M_{pl}$

The first regime is similar to chaotic inflation with a quadratic massive potential. Inflation ends when the slow-roll conditions are strongly violated at the transition close to  $\phi = \mu$ , the trajectories do not reach back the slow-roll attractors at small field values. This is due to the velocity acquired by the trajectories at the end of the large field phase as the slow-roll conditions do seem to be satisfied ( $\epsilon_1^{\text{SR}} \ll 1$  and  $\epsilon_2^{\text{SR}} \ll 1$ ). This effect is only seeable by integration of the exact dynamics. Fig. 3.2 and Fig. 3.3 show the value of  $\epsilon_1$  and  $\epsilon_2$  as a function of  $\phi$ , for  $\mu = 0.4M_{pl}$  and  $\mu = 0.7M_{pl}$  in the slow-roll approximation and as computed for the complete dynamics.

The effect of  $\mu$  can be seen on Fig. 3.4. This shows the number of e-folds produced after reaching the value of the maximum of the first Hubble-flow parameter. There is a threshold  $\mu_{\text{thr}} \sim 1.6M_{pl}$  below which only a reduced number of e-folds are realised. For values of the order  $\mu \lesssim 0.8M_{pl}$ , only a very small amount of e-folds is produced and the small field phase has no influence on the observable predictions.

The slow-roll approximation can be used up to  $\epsilon_1 = 1$ . At this point inflation

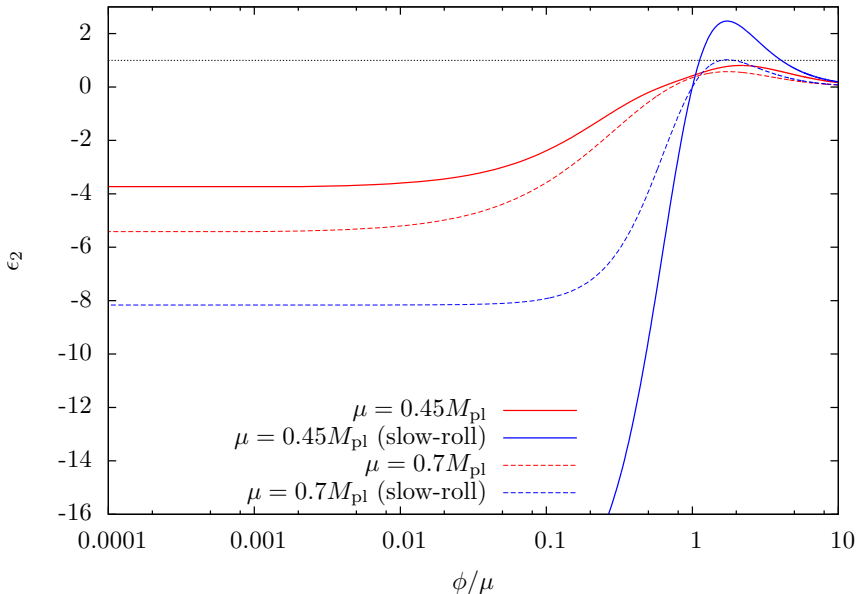


Figure 3.3 – Evolution of the second Hubble-flow parameter  $\epsilon_2$  as a function of  $\phi/\mu$ . As in Fig. 3.2 the complete solution differs from the slow-roll approximation for small values of  $\mu$ .

ends and the field has value

$$\phi_{\text{end}} \simeq \frac{\sqrt{2}}{2} M_{pl} \left( 1 + \sqrt{1 - \frac{\sqrt{2}\mu^2}{M_{pl}^2}} \right). \quad (3.68)$$

This is similar to the case of a quadratic potential in the limit  $\mu \ll M_{pl}$  where  $\phi_{\text{end}}$  is the value of the field at the end of inflation. Any difference in the exact value of the field compared to the slow-roll approximation has no significant effect on  $\phi_*$ . Integration of the slow-roll equation yields

$$\frac{\mu^2}{2M_{pl}^2} \left[ \ln \frac{\phi_{\text{end}}}{\phi_*} + \frac{1}{2\mu^2} (\phi_{\text{end}}^2 - \phi_*^2) \right] = N(\phi_*) - N_{\text{end}}. \quad (3.69)$$

The solution of this for  $\phi_*$  is given in terms of the principal branch of the Lambert function.

$$\phi_*^2 = \mu^2 W_0 \left( \frac{\phi_{\text{end}}^2}{\mu^2} e^{\frac{\phi_{\text{end}}^2 + 4N_*}{\mu^2}} \right). \quad (3.70)$$

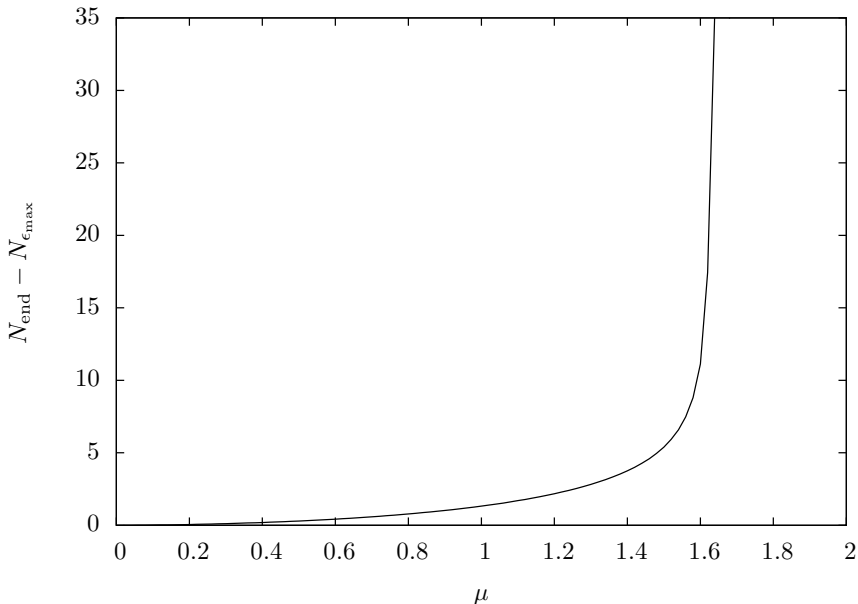


Figure 3.4 – Number of e-folds produced after reaching the maximum of  $\epsilon_1$  as a function of  $\mu$ . Below the threshold value  $\mu_{\text{thr}} \sim 1.6M_{pl}$ , only a few e-folds are realised at small field values in contradiction with slow-roll predictions.

In the limit  $\mu \ll M_{pl}$ , one has

$$\phi_* \simeq 2M_{pl} \sqrt{N_* + \frac{1}{2}} \simeq 15.5M_{pl} , \quad (3.71)$$

$$\epsilon_{1*} \simeq \frac{1}{2N_* + 1} \simeq 0.00826 , \quad \epsilon_{2*} \simeq 2\epsilon_{1*} \simeq 0.0165 , \quad (3.72)$$

$$n_s \simeq 1 - \frac{4}{2N_* + 1} \simeq 0.967 , \quad r \simeq \frac{16}{2N_* + 1} \simeq 0.132 , \quad (3.73)$$

assuming  $N_* = 60$ . These values are similar to the predictions of a massive quadratic potential and in agreement with both Planck and BICEP2 data.

### 3.4.2 Transitory: $\phi_c < \mu \sim \phi_*$ and $\mu \sim M_{pl}$

In this regime,  $\mu$  is close to the threshold value  $\mu_{\text{thr}}$ . A few e-folds are produced in the vacuum dominated regime but the observable scales exit the Horizon when the value of the field is large. As a result,  $\epsilon_{1*}$  and  $\epsilon_{2*}$  take larger values than in the chaotic-like regime. The scalar spectral index is lower and can accommodate the best fit of Planck at  $n_s = 0.961$  while the tensor to scalar

ratio is enhanced and can accommodate the central value of BICEP2  $r = 0.20$ . The CMB data thus favour this regime as opposed to the quadratic potential. However, both models lie within the  $2\sigma$  confidence level, assuming  $N_* = 60$ .

### 3.4.3 Large Critical Field Value: $\mu < \phi_c < \phi_*$

In the final regime considered, the critical instability point lies within the large field region of the potential. Thus,  $\mu < \phi_c$  and  $\phi_{\text{end}} = \phi_c > \sqrt{2}M_{pl}$ . The slow-roll approximation is valid prior to the critical field value. The solution of Eq. (3.69) in the limit  $\mu \ll \phi_c$  is

$$\phi_*^2 \simeq \phi_c^2 + 4N_*M_{pl}^2, \quad (3.74)$$

this gives values of the spectral index and tensor to scalar ratio independent of the parameter  $\mu$

$$n_s \simeq 1 - \frac{8M_{pl}^2}{\phi_c^2 + 4N_*M_{pl}^2} \quad r \simeq \frac{32M_{pl}^2}{\phi_c^2 + 4N_*M_{pl}^2}. \quad (3.75)$$

Fig. 3.5 shows the values of  $\phi_*$ ,  $n_s$  and  $r$  as functions of  $\phi_{\text{end}}$  for several values of  $\mu$  with  $N_* = 60$  s derived from the above formulae.

In the following section, we present a summary of the observable predictions of the regimes here described.

## 3.5 The $(\phi_c, \mu)$ parameter space

The synthesis of the observable predictions of Large Field regimes described above can be understood by inspection of Fig. 3.6 and Fig. 3.7. These have been plotted by numerically solving for the exact background dynamics of the field using the complete Klein-Gordon equation without the slow-roll approximation. It shows excellent consistency with the approximate analytical results.

The chaotic-like regime corresponds to the bottom left part of the parameter plane. This lies within the  $2\sigma$  region for both Planck and BICEP2 data. The large critical field value regime is found on the right-half of the plane. Very high values of the critical parameter ( $\phi_c \gtrsim 10M_{pl}$ ) are disfavoured by Planck data. The best agreement with the data from both Planck and BICEP2 lies within the transitory regime. For  $\phi_c \ll M_{pl}$ , the spectral index is close to the best fit of Planck when  $\mu \sim 2$  to  $3M_{pl}$ , as well as in a very thin band around  $\mu \simeq 4M_{pl}$ . Increasing  $\phi_c$  to  $\phi_c \sim \mu$ , the best fit is obtained around  $3M_{pl} < \mu < 5M_{pl}$ . This is expected since the increase of  $\phi_c$  reduces the number of e-folds produced during the vacuum dominated phase so that larger values of  $\mu$  are necessary.

The constraints on the model are studied by means of a *Markov-Chain-Monte-Carlo* (MCMC) Bayesian analysis. In a nutshell, one has that the pos-

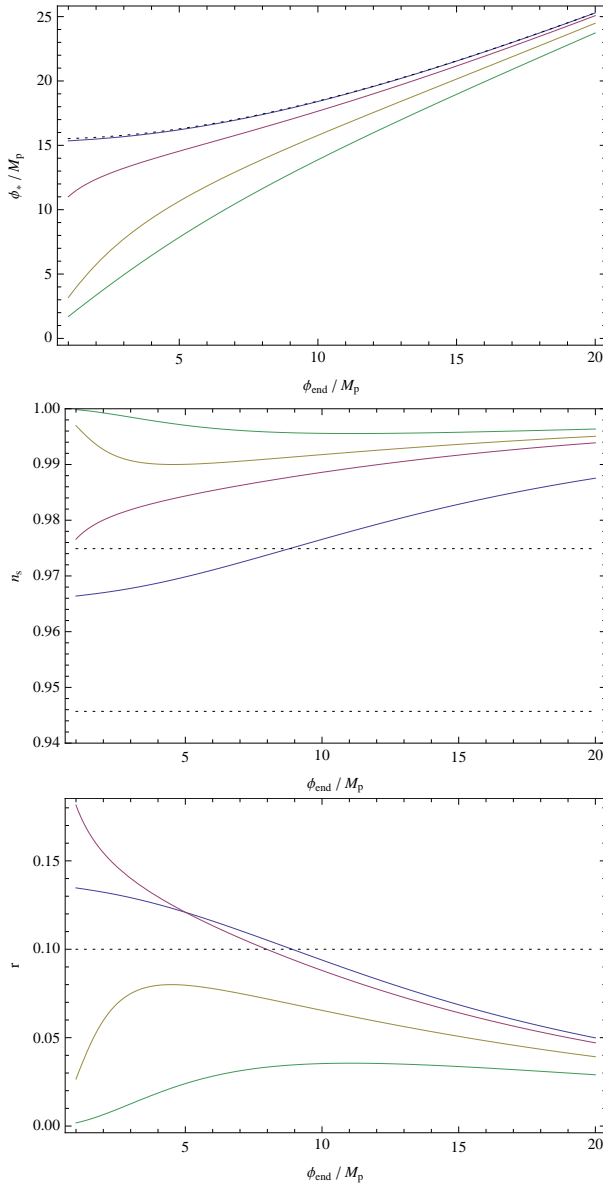


Figure 3.5 –  $\phi_*$  (top) and corresponding  $n_s$  (central) and  $r$  (bottom) plotted as a function of  $\phi_{\text{end}} = \phi_c$  using Eq. (3.70), for  $\mu = 1M_{pl}$  (blue),  $\mu = 5M_{pl}$  (red),  $\mu = 10M_{pl}$  (yellow) and  $\mu = 15M_{pl}$  (green), assuming  $N_* = 60$ . The horizontal dotted lines in the central and bottom panels represent respectively the  $2\sigma$  regions of Planck and BICEP2. The dotted line in the top panel is obtained by using the approximation of Eq. (3.74).

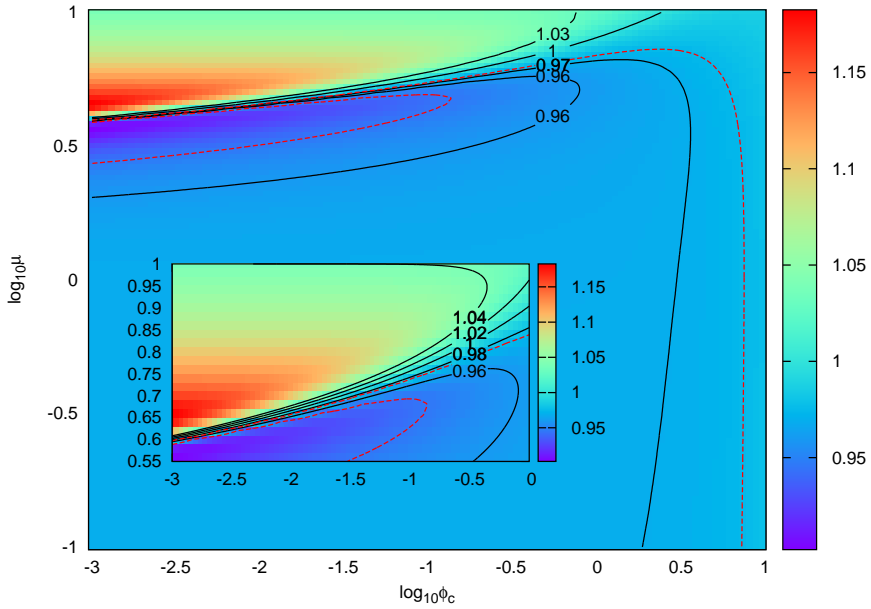


Figure 3.6 – Contour plot of the spectral index  $n_s$  in the plane  $(\log_{10} \phi_c, \log_{10} \mu)$ , using the exact background dynamics and assuming  $N_* = 60$ . The red dashed contours represent the  $2\sigma$  confidence interval for Planck.

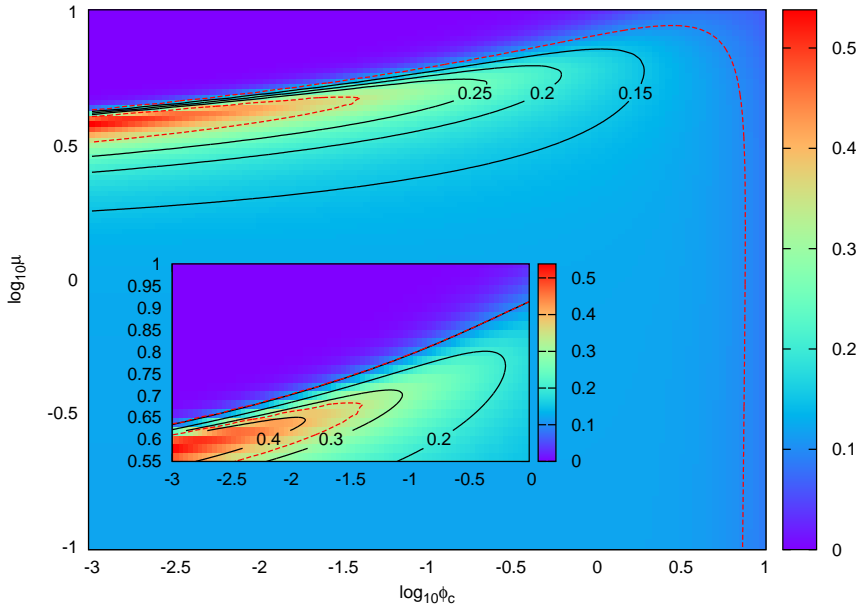


Figure 3.7 – Contour plot of the tensor to scalar ratio  $r$  in the plane  $(\log_{10} \phi_c, \log_{10} \mu)$ , using the exact background dynamics and assuming  $N_* = 60$ . The red dashed contours represent the  $2\sigma$  confidence interval for BICEP2.

terior probability distribution for a parameter  $\lambda_i$  given a set of data  $D$  is

$$p(\lambda_i|D) = \frac{p(D|\lambda_i)\pi(\lambda_i)}{\int d\lambda_i p(D|\lambda_i)\pi(\lambda_i)}, \quad (3.76)$$

where  $\pi(\lambda)$  is the prior probability distribution. The denominator is called the *Bayesian evidence* and is used for normalisation. It can be disregarded for the study of model constraints.

The analysis is performed by comparison with CMB data using a modified version of the `COSMOMC` package (Lewis and Bridle 2002). The exact field dynamics is computed numerically for each given value of the model parameters. The spectral index  $n_s$ , tensor to scalar ratio  $r$  and the end of inflation energy density  $\rho_{\text{end}}$ , are derived parameters.

### 3.6 Statistical Analysis

Disregarding the impact of transplanckian physics on inflation, there is no obvious high energy physics bounds on the values of the parameters  $\Lambda$ ,  $\mu$ ,  $\phi_c$  and  $R$ . Both  $\Lambda$  and  $\mu$  have an effect on the amplitude of spectral power spectrum. As they are strongly correlated, probing these parameters independently would not be very efficient in terms of computational time. Following Martin et al. (Martin, Ringeval, Trota and Vennin 2014), we replace the parameter  $\Lambda$  by directly varying  $A_s$ .  $\Lambda$  is then one further derived parameter. We use a uniform prior distribution on a logarithmic scale for all other parameters.

We set the prior for  $\log_{10} \mu$  as the interval  $(-2, 1.2)$ . There is no need to probe higher values as this would fall in the case of vacuum dominated regime leading to a blue spectrum strongly disfavoured by Planck data. Smaller values lead to predictions similar to those derived for a quadratic potential. The range prescribed allows to probe the whole transitory regime.

The prior for  $\log_{10} \phi_c$  is chosen as the interval  $(-8, 2)$ . Higher values lead to values of the spectral index too low to be acceptable. The lower bound is chosen arbitrarily. It has been checked that, for lower values, the predictions do not depend on  $\phi_c$ .

Following (Martin et al. 2014), the range of the reheating parameter is chosen as  $\ln R$  in the interval  $(-46, 15)$ . This includes all reheating histories with energy density higher than the energy density of the Big Bang Nucleosynthesis (BBN).

The remaining of the parameters priors, including  $A_s$  are set to the default bounds of `COSMOMC`. This includes the cosmological parameters  $\Omega_b h^2$ ,  $\Omega_c h^2$ ,  $\tau$  and  $\theta$  as well as 14 nuisance parameters of the Planck experiment.

Due to the large dimensionality of the parameter space, the simple Metropolis-Hastings algorithm would converge very slowly. To allow a quicker convergence, the code solves for the background dynamics only when one or more of the main four hybrid parameters are changed. Moreover, `COSMOMC` uses a fast dragging method to decorrelate some parameters by rotation of the sampling direction.

Parameter	Best-fit	Mean	$1\sigma$ range	$2\sigma$ range
$\log_{10} \mu$	-0.27	-0.18	[*, 0.045]	[* , *]
$\log_{10} \phi_c$	-2.9	-2.7	[-4.6, 1.4 ]	[* , 1.20 ]
$\ln R$	-8.4	-8.0	[-17, *]	[-32,*]
$\log_{10} \rho_{\text{end}}$	-10.5	-10	[-11, -9.5]	[-11, -8.3]
$n_s$	0.962	0.963	[0.949, 0.977]	[0.929, 0.995]
$r$	0.151	0.155	[0.09, 0.20]	[0.03, 0.30]
$\log_{10} \mu$	-0.24	-0.21	[*, 0.021]	[*, 0.72]
$\log_{10} \phi_c$	-3.2	-2.5	[-4.0, 1.5 ]	[*, 1.5 ]
$\ln R$	-5.00	-10	[-17, *]	[-34, *]
$\log_{10} \rho_{\text{end}}$	-10.5	-10	[-11, -8.9]	[-11, -8.4]
$n_s$	0.965	0.962	[0.950, 0.975]	[0.930, 0.991]
$r$	0.139	0.158	[0.10, 0.20]	[0.04, 0.29]

Table 3.1 – Best fit, mean likelihood and  $1\sigma$  and  $2\sigma$  intervals for hybrid model parameters (in units of reduced Planck mass), for Planck+BAO (upper part) and Planck+BAO+BICEP2 (lower part). A star denotes bounds outside of the prior limits.

It also makes a distinction between the fast and slow parameters depending on the computational cost to derive the likelihood when one of these is changed. The MCMC temperature has to be adjusted in order to optimise the sampling rate of the fast and slow parameters.

The Bayesian analysis has been conducted for Planck+BAO+BICEP2 data, as well as for Planck+BAO only. The  $1\sigma$  and  $2\sigma$  intervals are reported in Tab. 3.1. For Planck+BICEP2+BAO we find that  $\log_{10} \mu < 0.72$  at  $2\sigma$  level. Above this value, the hybrid model corresponds to the usual picture of inflation in the vacuum dominated phase with a blue spectrum. There is no lower bound on  $\phi_c$ . Interestingly when BICEP2 data are included, the reheating parameter is constrained to  $\ln R > -34$ . Simultaneously, the energy density at the end of inflation has a maximum likelihood at  $\rho_{\text{end}} \sim 6 \times 10^{15} \text{GeV}$ , close to the GUT scale. The energy scale of inflation lies within the range  $4.3 \times 10^{15} \text{GeV} < \rho_{\text{end}}^{1/4} < 1.8 \times 10^{16} \text{GeV}$  at  $2\sigma$  level.

The one-dimensional and two-dimensional marginalised posterior probability density distributions for parameters  $\log_{10} \mu$ ,  $\log_{10} \phi_c$ ,  $\ln A_s$  and  $\ln R$  are displayed on Fig. 3.8. Posterior probabilities for the standard cosmological parameters are identical to the Planck analysis of a  $\Lambda$ CDM model with  $n_s$ ,  $r$  and  $\ln A_s$  as primordial spectra parameters. This is expected given that our code derives  $n_s$  and  $r$  for each set of hybrid model parameters. The marginalised

probabilities for the derived parameters  $r$ ,  $n_s$  and  $\rho_{\text{end}}$  are displayed on Fig. 3.9

The marginalised probabilities in the plane  $(\log_{10} \mu, \log_{10} \phi_c)$  are consistent with expectations from Fig. 3.6 and Fig. 3.7. The likelihood is higher in the region corresponding to the transitory regime, and the best fit values of Tab. 3.1 lie in this region. For Planck+BICEP2+BAO data, the best fit corresponds to a  $\Delta\chi^2 \simeq 5.1$  in favour of hybrid inflation as opposed to the quadratic potential, with  $\mu = 0.54M_{pl}$ ,  $\phi_c = 6.4 \times 10^{-4}M_{pl}$ ,  $\ln R = -5$ . Note that the likelihood is reasonably flat in a rather wide region of the parameter space, which makes it difficult to identify the best fit value.

The chaotic regime remains within the  $1\sigma$  bound, whereas for the large critical field regime we find that  $\log_{10} \phi_c < 1.5$  at  $2\sigma$  confidence level. This bound is larger than what is expected from Fig. 3.5 with  $N_* = 60$ , but it is obtained after marginalisation over  $\ln R$ , which allows  $N_*$  (and correspondingly  $\phi_*$ ) to take lower values.

Finally we have displayed in Fig. 3.10 the spectral index and the tensor to scalar ratio in the plane  $(\log_{10} \mu, \log_{10} \phi_c)$  for 3000 points of the Markov chains. This figure illustrates how the spectral index is enhanced in the large critical field regime whereas the tensor to scalar ratio decreases. The density of points is proportional to the probability of the model. There are a few points at larger values of  $\mu$  corresponding to the small field regime that generates a spectral index larger than unity.

### 3.7 Conclusion

We have shown how the hybrid model of inflation can generate a red spectrum of scalar perturbations from its large field regime. This is due to a non-trivial effect of its dynamics which prevent the slow-roll conditions to be reached again in the small field regime. We have identified 3 sub-regimes. In the *Large critical instability point* regime, inflation stops with an instantaneous tachyonic instability for super-Planckian values of the field. This makes predictions on the scalar index and tensor to scalar ratio similar to those made in the case of a single field model with massive potential though the spectral index value is slightly closer to unity and the tensor to scalar ratio is slightly lower. The *Chaotic-like* regime predicts a violation of the slow-roll conditions as the field enters the vacuum dominated phase and these are never verified again subsequently. The observable length scales exit the horizon during the large field phase and the observable predictions are identical to those of the massive single field model. The last of these regimes is the *Transitory* regime in which a small amount of e-folds of inflation is realised in the vacuum dominated phase. This regime predicts a lower value of the spectral index and a bigger value of the tensor to scalar ratio.

The analysis shows that the Transitory regime is the one that shows the best agreement with the experimental data. The best-fit to Planck data corresponds to a value of  $\mu \sim 0.5M_{pl}$ . This corresponds to  $\Delta\chi^2 \simeq 5.0$  in favour of hybrid

inflation for the combined data from Planck and BICEP2 and  $\Delta\chi^2 \simeq 0.9$  for Planck data only. The Chaotic-like regime lies within the  $2\sigma$  confidence region of both datasets for  $\phi_c \lesssim 10$ .

This work shows how the hybrid model at large field values remains a inflation candidate yielding a value of the tensor to scalar ratio close to the central value of BICEP2 for parameters also predicting a spectral index close to Planck best fit. The recent joint analysis of data from BICEP2, Keck Array and Planck has set a new upper-bound on the value of the tensor to scalar ratio at  $r < 0.12$  arguing in favour of a large contribution to the signal from galactic dust (Ade et al. 2015). Admittedly, this has reduced the most direct interest in the work presented in this chapter. However, the value of this work in revealing seldom explored regimes of hybrid inflation leading a large value of  $r$  that will be possible to test in the near future still holds.

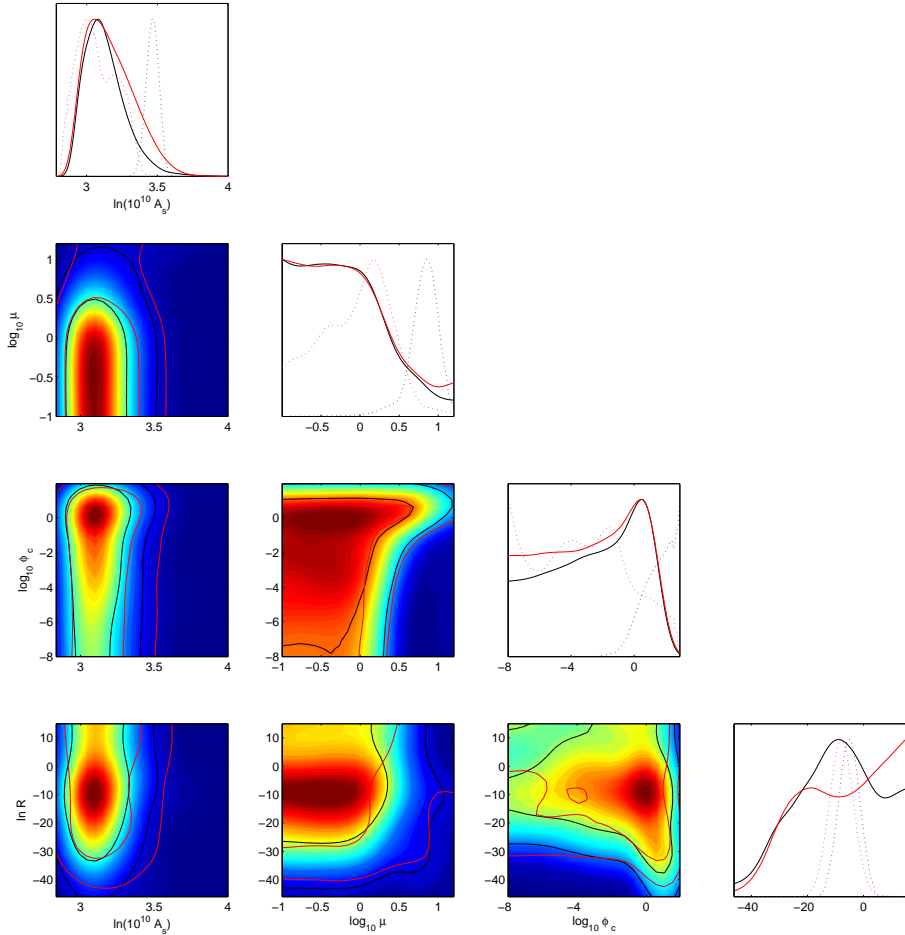


Figure 3.8 – Marginalised one-dimensional and two-dimensional posterior probabilities for the hybrid model parameters (in reduced Planck mass units) in the large field regime, for Planck+BICEP2. The red contours are the  $1\sigma$  and  $2\sigma$  regions of confidence. The black contours are the  $1\sigma$  and  $2\sigma$  regions for Planck only. In the 1D plots, the black/red solid lines show the marginalised posterior distributions of the parameters respectively for Planck and Planck+BICEP2. The dotted lines represent the mean likelihoods.

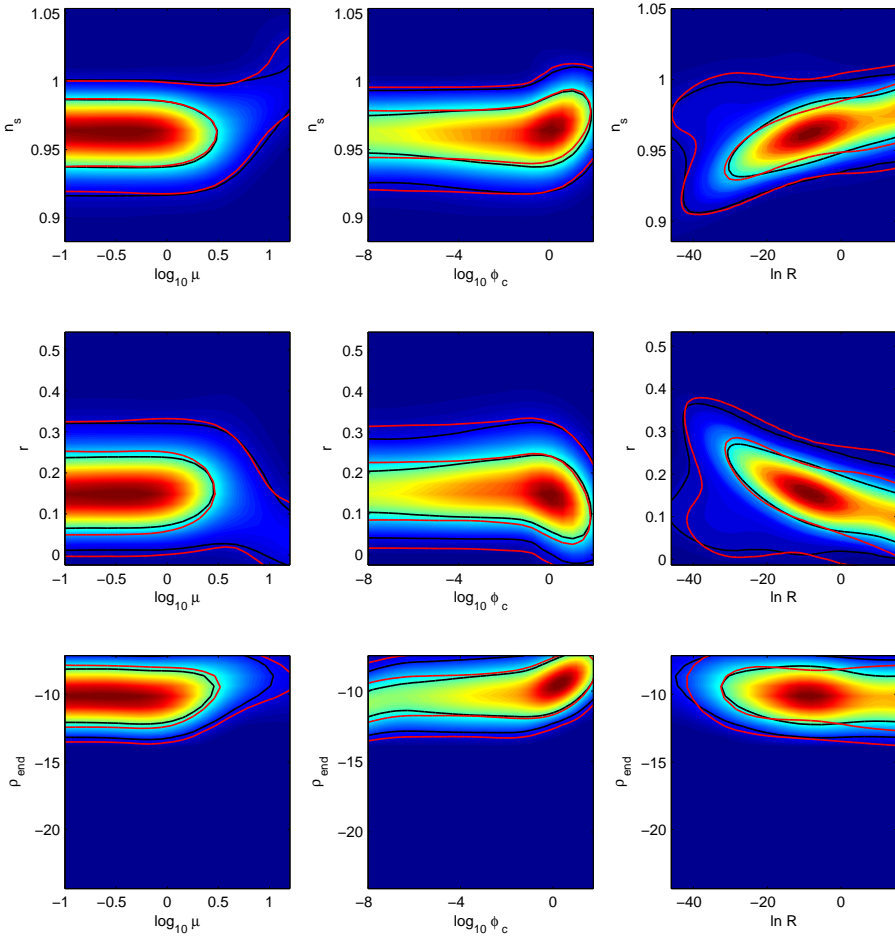


Figure 3.9 – Two-dimensional marginalised posterior probabilities for the hybrid model parameters (in reduced Planck mass units) as well as the derived parameters  $n_s$ ,  $r$  and  $\rho_{\text{end}}$  for Planck+BICEP2. The red contours are the  $1\sigma$  and  $2\sigma$  regions of confidence. The black contours are the  $1\sigma$  and  $2\sigma$  regions for Planck only.

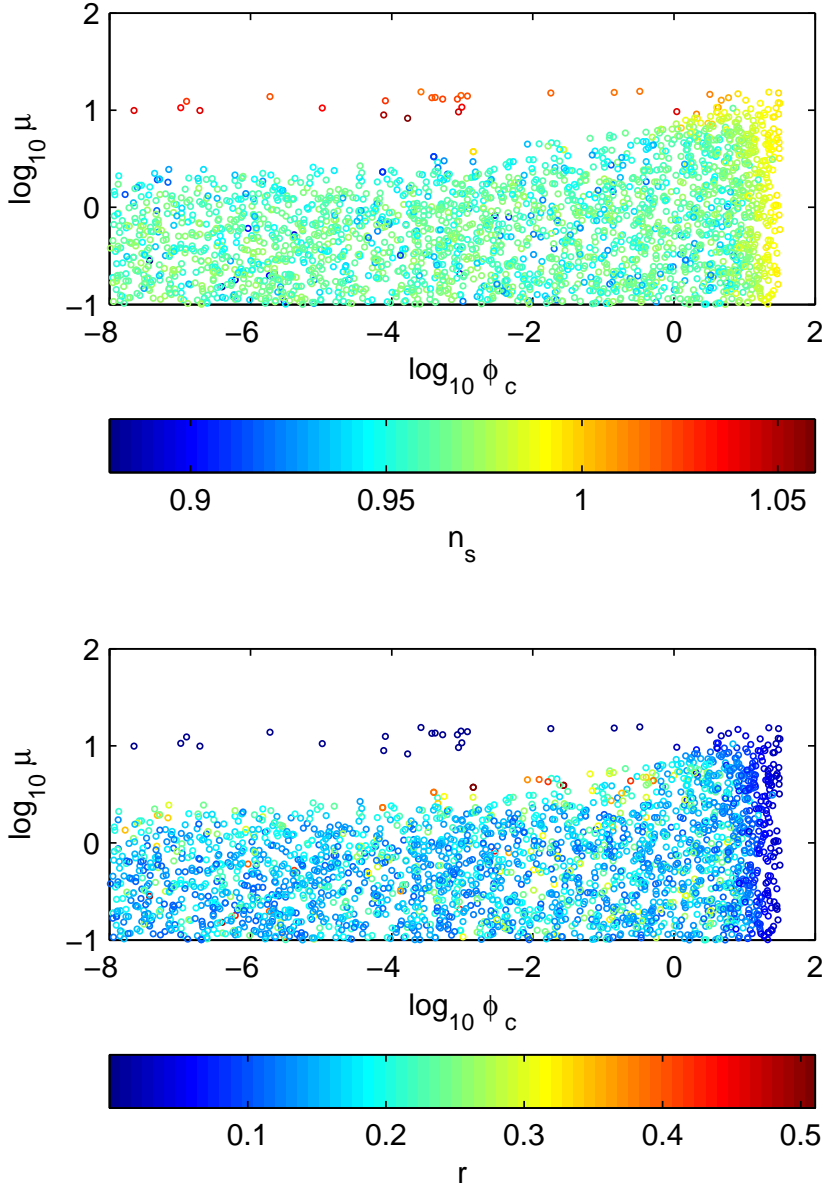


Figure 3.10 – Distribution of 3000 points within the Markov chains in the plane  $(\log_{10} \mu, \log_{10} \phi_c)$ . In the upper panel, the colour scale represents the corresponding spectral index value, in the lower panel it represents the corresponding tensor to scalar ratio.

## Chapter 4

# Cosmological Spherical Collapse

In this chapter, we address the problem of spherical collapse starting with a discussion on the top-hat model in which we show how this very simplistic model can originate from simplifying assumptions on the geometry of the cosmological spherically symmetric solution both of Newtonian dynamics and General Relativity. This allows us to put emphasis on the debatable hypotheses that we dismiss in favour of a fully relativistic treatment described in the sections that follow. These use the BSSN formalism to provide a numerical solution for the complete dynamics of the system. Tests of the numerical reliability of the code there used are provided in various cases before moving on to consider the collapse in presence of quintessence. We put our results in perspective with those of the top-hat model and analyse the differences in the physics that is involved in both formalisms.

### 4.1 The top-hat model

The most widely used model for the study of the cosmological collapse in presence of quintessence is the so-called *top-hat* model in which the spatial domain is divided in two parts following a radial step distribution of matter.

The usual treatment makes the hypothesis that the inner and outer regions of space-time should both assume the homogeneous and isotropic geometry of FLRW,  $a(t)$  and  $R(t)$  being respectively the scale factors outside and inside of the over-dense region. It is also assumed that both regions share the same synchronous time coordinate. The dynamics of the whole space-time dynamics

is then described by two separate Friedmann equations

$$\left(\frac{\dot{a}}{a}\right)^2 = \frac{8\pi}{3}\bar{\rho} \quad (4.1)$$

$$\left(\frac{\dot{R}}{R}\right)^2 = \frac{8\pi}{3}(\bar{\rho} + \Delta\rho) - \frac{k}{R^2} . \quad (4.2)$$

Here  $\bar{\rho}$  is the homogeneous energy density of the background Universe and  $\Delta\rho$  is the supplementary density within the over-dense region. It is customary to assume that the background Universe is spatially flat.  $k$  is the spatial curvature of the inner space-time.

Pressures and energy densities are considered homogeneous both in the inner and the outer space-time regions. The density components each follow a separate conservation equation

$$\frac{d}{dt}\bar{\rho} + 3\frac{\dot{a}}{a}(\bar{\rho} + \bar{p}) = 0 \quad (4.3)$$

$$\frac{d}{dt}(\bar{\rho} + \Delta\rho) + 3\frac{\dot{R}}{R}[(\bar{\rho} + \Delta\rho) + (\bar{p} + \Delta p)] = \Gamma . \quad (4.4)$$

The function  $\Gamma$  is an adjustable parameter, the form of which depends on the clustering properties of the considered species (Mota and van de Bruck 2004). We discuss this parameter later when we deal with quintessence.

In this section, we explain how the above equations can be somehow justified from Newtonian perturbations for pressure-less matter (Padmanabhan 1993). We then derive them again from the equations of General Relativity while taking special care in listing all the limiting assumptions involved.

### 4.1.1 The top-hat model from Newtonian physics

Let us write the density of matter at some fixed time  $t_i$  as

$$\rho(t_i, r) = \bar{\rho}(t_i)(1 + \delta_i(r)) , \quad (4.5)$$

with  $\delta_i(r)$  some “well-behaved” function called the *density contrast*. In the weak field regime and for perturbations much smaller than the horizon, it seems reasonable to write the gravitational potential as a combination of an homogeneous background component and one due to the over-dense region,

$$\Phi(t, r) = \bar{\Phi}(t) + \delta\Phi(t, r) . \quad (4.6)$$

The homogenous part is found by considering the Poisson equation  $\nabla^2\bar{\Phi} = 4\pi\bar{\rho}$ . Assuming spherical symmetry and regularity at the origin of coordinates, one finds

$$\bar{\Phi} = \frac{4\pi}{3}\bar{\rho}\frac{r^2}{2} . \quad (4.7)$$

Where the zero of energy has been chosen to cancel out the integration constant.

The motion of a thin shell placed at a radius  $r\vec{r}$  from the centre of coordinates is given by Newton's second law

$$\begin{aligned} \frac{d^2 r\vec{r}}{dt^2} &= -\vec{\nabla}\Phi \\ &= -\frac{4\pi}{3}\bar{\rho}r\vec{r} - \vec{\nabla}(\delta\Phi) . \end{aligned} \quad (4.8)$$

This can be written in terms of the mass within each shell

$$\frac{d^2 r\vec{r}}{dt^2} = -(\bar{M} + \delta M(t, r))\frac{r\vec{r}}{r^3} , \quad (4.9)$$

where  $\bar{M} := \frac{4\pi}{3}\bar{\rho}r^3$  is the mass obtained by integration of the homogeneous background density and

$$\delta M := 4\pi\bar{\rho}(t) \int_0^r x^2 \delta(t, x) dx , \quad (4.10)$$

is the supplementary mass within the over-dense region. This is constant as long as one assumes that the shells do not cross each other during their collapse.

One then writes

$$\frac{d^2 r}{dt^2} = -\frac{M}{r^2} , \quad (4.11)$$

where  $M(t) := \frac{4\pi}{3}\bar{\rho}(t)r_i^3(1 + \langle \delta_i \rangle)$  with

$$\langle \delta_i \rangle := \left( \frac{3}{4\pi} \frac{1}{r_i^3} \int_0^{r_i} x^2 \delta_i(x) dx \right) , \quad (4.12)$$

the spatial average of the initial density contrast  $\delta_i$ . Eq. (4.11) has a first integral

$$\frac{1}{2} \left( \frac{dr}{dt} \right)^2 = \frac{M}{r} - E , \quad (4.13)$$

where  $E$  is an integration constant. In the picture described here, the motion of each shell is independent of the motion of the others. This can be seen by realising that Eq. (4.13) is an ordinary differential equation and contains no spatial gradient that would couple the dynamics of each shell to its neighbours. This equation can be put in the shape of Eq. (4.2) when the energy density profile is a step function (hence the name ‘‘top-hat’’). In that case,  $\langle \delta_i \rangle = \delta_i$  and one has

$$\frac{1}{r^2} \left( \frac{dr}{dt} \right)^2 = \frac{8\pi}{3}\bar{\rho}(t)(1 + \delta(t)) - \frac{E}{r^2} . \quad (4.14)$$

The above argument in favour of the equations of the top-hat model are valid in a Newtonian context. We now present how this can be derived from a relativistic treatment.

### 4.1.2 The top-hat model from General Relativity

The most general line-element of a spherically symmetric relativistic space-time is

$$ds^2 = -(\alpha^2 - \beta^r \beta_r) dt^2 + 2\beta_r dt dr + \gamma_{rr} dr^2 + \gamma_{\theta\theta} r^2 d\Omega^2, \quad (4.15)$$

where  $\beta^r$  is the only non-zero component of the shift vector  $\beta_i = (\beta_r, 0, 0)$ . The metric and extrinsic curvature tensors are diagonal

$$\gamma_{ij} = \begin{pmatrix} \gamma_{rr} & & \\ & \gamma_{\theta\theta} & \\ & & \gamma_{\theta\theta} \end{pmatrix}, \quad K_{ij} = \begin{pmatrix} K_{rr} & & \\ & K_{\theta\theta} & \\ & & K_{\theta\theta} \end{pmatrix}. \quad (4.16)$$

The energy source terms are constrained to be functions of  $t$  and  $r$  only and of the form

$$S_{ij} = \begin{pmatrix} S_{rr} & & \\ & S_{\theta\theta} & \\ & & S_{\theta\theta} \end{pmatrix}, \quad j_i = (j_r(t, r), 0, 0). \quad (4.17)$$

The conservation of energy and momentum equations Eq. (2.31) and Eq. (2.34) respectively reduce to

$$\frac{1}{\alpha} (\partial_t - \mathcal{L}_\beta) E + \partial_r j^r + 2j^r \frac{\partial_r \alpha}{\alpha} - KE - (K_r^r S_r^r + 2K_\theta^\theta S_\theta^\theta) = 0 \quad (4.18)$$

$$\frac{1}{\alpha} (\partial_t - \mathcal{L}_\beta) j_r + D_r S_r^r + S_r^r \frac{\partial_r \alpha}{\alpha} - K j_r + E \frac{\partial_r \alpha}{\alpha} = 0 \quad (4.19)$$

In order to proceed, let us assume, for now, that the energy source is a **single perfect fluid**. We later examine the validity of the solution when this (strong) assumption is relaxed.

We follow the work of Lasky et al. (Lasky and Lun 2006) and choose the frame of the Eulerian observer as the rest frame of the fluid so that the fluid's four velocity is identified to the normal vector  $n_\mu$  and,

$$T_{\mu\nu} = (\rho + p)n_\mu n_\nu + pg_{\mu\nu}. \quad (4.20)$$

We further write the line-element as

$$ds^2 = -\alpha^2 dt^2 + \frac{1}{1+2E} (\beta dt + dr)^2 + r^2 d\Omega^2. \quad (4.21)$$

where  $\beta := \beta_r$  and  $E > -1/2$  which should not to be confused with the ADM function for the energy density which here is simply  $\rho$ . The energy and momentum conservation equations for a perfect fluid respectively reduce to

$$\frac{1}{\alpha} (\partial_t - \mathcal{L}_\beta) \rho = (\rho + p)K \quad (4.22)$$

$$\partial_r p = -(\rho + p) \frac{\partial_r \alpha}{\alpha}, \quad (4.23)$$

the latter being the relativistic version of the Euler equation (Landau and Lifshitz 1987). Lasky et al. perform the interesting observation that, in spherical symmetry, any traceless rank two tensor has but one non-zero eigenvalue and proceed to define

$$K_{ij} - \frac{1}{3}\gamma_{ij}K := a(t, r)P_{ij} , \quad (4.24)$$

$$R_{ij} - \frac{1}{3}\gamma_{ij}R := q(t, r)P_{ij} , \quad (4.25)$$

$$\frac{1}{\alpha}D_i D_j \alpha - \frac{1}{3\alpha}\gamma_{ij}D^k D_k \alpha := \epsilon(t, r)P_{ij} , \quad (4.26)$$

with  $P_j^i := \text{diag}(-2, 1, 1)$ . This allows to write the constraint and evolution equations respectively as

$$R + \frac{2}{3}K^2 - 6a^2 = 16\pi\rho , \quad (4.27)$$

$$\partial_r(ar^3) = -\frac{r^3}{3}\partial_r K , \quad (4.28)$$

$$2\mathcal{L}_n K - \frac{1}{2}R - K^2 - 9a^2 + \frac{2}{\alpha}D^k D_k \alpha = 24\pi p , \quad (4.29)$$

$$\mathcal{L}_n \alpha - \alpha K + \epsilon - q = 0 . \quad (4.30)$$

By writing the curvature variables explicitly in terms of the metric components, one arrives to (see the original work for details)

$$-2E = 2r(1 + 2E)\frac{\partial_r \alpha}{\alpha} - 8\pi p r^2 + 2r\mathcal{L}_n \frac{\beta}{\alpha} - \left(\frac{\beta}{\alpha}\right)^2 , \quad (4.31)$$

substituting this in the Hamiltonian constraint yields

$$4\pi\rho r^2 = \partial_r \left[ r^2(1 + 2E)\frac{\partial_r \alpha}{\alpha} + r^2\mathcal{L}_n \frac{\beta}{\alpha} - 4\pi p r^3 \right] . \quad (4.32)$$

The integration of this last expression along the radial coordinate has the dimensions of mass so we write

$$M(t, r) := 4\pi \int_0^r \rho x^2 dx . \quad (4.33)$$

Substituting in the Euler equation and using again Eq. (4.31) provides the elegant algebraic relation

$$2E + \frac{2M}{r} = \left(\frac{\beta}{\alpha}\right)^2 . \quad (4.34)$$

Solving for  $\beta$  allows to formulate the complete system in the following way:

$$ds^2 = -\alpha^2 dt^2 + \frac{(\alpha\sqrt{\frac{2M}{r} + 2E}dt + dr)^2}{1 + 2E} + r^2 d\Omega^2, \quad (4.35)$$

$$\partial_t M - \alpha\sqrt{\frac{2M}{r} + 2E}(\partial_r M + 4\pi pr^2) = 0, \quad (4.36)$$

$$\partial_t E - \alpha\sqrt{\frac{2M}{r} + 2E}\left(\partial_r E + 2\frac{1 + 2E}{\rho + p}\partial_r p\right) = 0. \quad (4.37)$$

The adjunction of the Euler equation and an equation of state for the fluid close the system.

The above expression for the metric is non-conventional. In order to recover a more traditional expression, one performs the change of variables  $(t, r) \rightarrow (T, \chi)$  defined through

$$\left(\frac{\partial r}{\partial T}\right)^2 = \alpha^2 \left(\frac{2M}{r} + 2E\right). \quad (4.38)$$

The system then becomes

$$ds^2 = -\alpha^2 dT^2 + \frac{(\partial_\chi r)^2}{1 + 2E} d\chi^2 + r^2 d\Omega^2, \quad (4.39)$$

$$\frac{\partial M}{\partial T} = 4\pi pr^2 \alpha \sqrt{\frac{2M}{r} + 2E}, \quad (4.40)$$

$$\frac{\partial r}{\partial \chi} \frac{\partial E}{\partial T} = 2\frac{1 + 2E}{\rho + p} \frac{\partial p}{\partial \chi} \alpha \sqrt{\frac{2M}{r} + 2E}. \quad (4.41)$$

The Euler equation remains unchanged except for the formal substitution  $r \rightarrow \chi$ .

The line-element of Eq. (4.39) describes what is known as the *Lemaître-Tolman* metric. It was originally derived for pressure-less matter in which case

$$\frac{\partial M}{\partial T} = \frac{\partial E}{\partial T} = 0. \quad (4.42)$$

The Euler equation then imposes  $\alpha = \alpha(t)$  which can always be normalised to  $\alpha = 1$ . One then recognises Eq. (4.38) as the analog to Eq. (4.13) for the Newtonian motion of a thin shell of pressure-less matter. The collapse model described above for dust is known as the *Lemaître-Tolman-Bondi* (LTB) model. The function  $r(T, \chi)$  is the area radius so that the area of a sphere encircling the origin is  $4\pi r^2$  at all times. This gets rescaled in time in a way that generalises the behaviour of physical distances in the FLRW Universe.

From now on, we shall change notations and rewrite  $T$  as  $t$ . The derivation by Lasky et al. clearly shows how the decoupling of the dynamics of each shell is only possible for pressure-less matter. In such case, the energy density is

$$\rho(t, \chi) = \frac{M'}{4\pi r' r^2}, \quad (4.43)$$

which is singular when  $r = 0$  and  $r' = 0$ . The first singularity corresponds to the shell being at the centre of coordinates. The second corresponds to *shell-crossing* which happens when two shells have the same radial coordinate  $\chi$ . The presence of pressure prevents this to occur. Recall that in the Newtonian treatment, the fact that the mass within each shell could be considered a constant was precisely based on the assumption that the shells do not cross.

The top-hat model is a special case of LTB space-time with only two shells with decoupled dynamics. The energy density assumes a step-function profile. In spite of the obvious fact that the LTB space-time is non-isotropic, the top-hat picture further assumes that *the scaling of physical distances is isotropic and homogeneous both inside and outside of the over-dense region*. It however admits the possibility that the isotropic scale factor can take different values inside and outside of the over-dense region. One thus has the step-function representation

$$r(t) = \begin{cases} R(t)\chi & : \chi \leq \chi_\delta(t) \\ a(t)\chi & : \chi > \chi_\delta(t) \end{cases},$$

with  $\chi_\delta$  being the radius of the over-dense region. This drastically simplifies the resolution of the conservation equation providing the well-known relation for the rescaling of dust energy densities.

$$\rho(t_i)R^3(t_i) = \rho(t)R^3(t) \quad (4.44)$$

$$\rho(t_i)a^3(t_i) = \rho(t)a^3(t). \quad (4.45)$$

An analytical expression for the mass function  $M$  can be found from its definition. For  $\chi \leq \chi_\delta$ :

$$M(\chi) = 4\pi \int_0^\chi \bar{\rho}(1 + \delta(x))x^2 r'(x)r^2(x)dx \quad (4.46)$$

$$= \frac{4\pi}{3}\bar{\rho}_i(1 + \delta_i)R(t_i)^3\chi^3. \quad (4.47)$$

Upon reinsertion into Eq.(4.38), one recovers a Friedmann-like equation for the inner region

$$\left(\frac{\dot{R}}{R}\right)^2 = \frac{8\pi}{3}\bar{\rho}(1 + \delta) + \frac{2E}{R^2\chi^2}. \quad (4.48)$$

For the outer region ( $\chi > \chi_\delta$ ):

$$\begin{aligned} M(\chi) &= 4\pi \int_0^{\chi_\delta} \bar{\rho}_i(1 + \delta_i)x^2 R_i^3 dx + 4\pi \int_{\chi_\delta}^{\chi} \bar{\rho}_i x^2 a_i^3 dx \\ &= 4\pi \bar{\rho}_i(1 + \delta_i) \frac{\chi_\delta^3}{3} R_i^3 + 4\pi \bar{\rho}_i a_i^3 \frac{(\chi^3 - \chi_\delta^3)}{3} . \end{aligned} \quad (4.49)$$

In the study of the spherical collapse, it is customary to assume that *the expansion factor in the outer and inner regions are initially identical* so that

$$a(t_i) = R(t_i) . \quad (4.50)$$

Equation (4.49) then simplifies to

$$M(\chi) = \frac{4\pi \bar{\rho}_i a_i^3}{3} \chi^3 \left( 1 + \delta_i \frac{\chi_\delta^3}{\chi^3} \right) . \quad (4.51)$$

The first term of these comes from the contribution of the background density. The second is due to the over-density at the centre of coordinates. Reinsertion into Eq.(4.38) yields

$$\left( \frac{\dot{a}}{a} \right)^2 = \frac{8\pi}{3} \bar{\rho} \left( 1 + \delta \frac{\chi_\delta^3}{\chi^3} \right) + \frac{2E}{a^2 \chi^2} . \quad (4.52)$$

The left-hand-side of Eq.(4.52) does not depend on  $\chi$  whereas, the right-hand-side manifestly does. This appears as a contradiction as there is no obvious way to compensate this dependency. To solve the problem, the equation here provided is *always considered in the limit*  $\chi \gg \chi_\delta$ . The major contribution to the mass function then comes from the background and not the over-density. The fact that this limit has to be taken to “save” the top-hat model points out that the intermediary region between the background and the over-density needs more care than can be provided by the model. Once the limit is taken, one arrives to the curious conclusion that the size of the over-dense region plays no part in the collapse process.

In the light of the above we can enumerate the hypothesis involved in the derivation of the top-hat model in a general relativistic context. These are

1. the momentum transfer is null
2. the matter is pressure-less
3. space-time is isotropic both inside and outside of the over-dense region
4. the values of the interior and exterior scale factors are initially equal
5. the exterior Friedmann equations are only valid in the limit of large radii.

Once these assumptions are relaxed, the top-hat cannot be considered as a satisfactory model from a relativistic point of view. The simplicity of the top-hat makes it the most widely used model in studies of the cosmological spherical collapse. In spite of the successes these have obtained, these often fail to provide a clear statement of the above list of hypotheses and sometimes apply the top-hat model in contexts where most of the above assumptions are not met.

In the remainder of the present chapter, we wish to provide our own attempt at solving the cosmological spherical collapse in a way completely consistent with General Relativity and to compare it with the top-hat model.

## 4.2 Fully Relativistic solution for spherical collapse

The top-hat model as a limit case of LTB suffers from many inconsistencies. These are even more serious when the distribution of energy is not due to a single perfect fluid in which case, even the LTB solution breaks down as its derivation relies heavily on the hypothesis that  $j_\mu = 0$ . This cannot be in general assumed when space-time is filled with more than one fluid. In homogeneous cosmology, radiation is modelled as another fluid independent of dust matter. In case there are two fluids, it cannot be assumed that these share the same rest frame. Supposing that the Eulerian observer is comoving with respect to the first fluid, then the momentum transfer reads (Rezzolla and Zanotti 2013)

$$j_\mu = \rho h W v_\mu , \quad (4.53)$$

where  $v_\mu$ ,  $\rho$  and  $h$  are respectively the spatial velocity, energy density and enthalpy of the second fluid and  $W := (1 - v_\mu v^\mu)^{-1/2}$  is the Lorentz factor. In presence of a scalar field, the momentum transfer is given by Eq. (2.48). Any of these situations feature non-zero momentum transfer and pressure terms so that the use of the top-hat model makes even less sense.

The fully consistent relativistic treatment calls for numerical methods. Lasky et al. have made a step toward the generalisation of the LTB solution by formulating the problem as an initial value problem (Lasky and Lun 2007). We follow another approach based on the many successes of Numerical Relativity.

The application of the BSSN formalism to cosmology has already been applied by Shibata et al. to the study of primordial black holes formation (Shibata and Sasaki 1999b). We want to extend the range of application of this formalism to consider the formation of structures through spherical collapse during the matter and Dark Energy dominated era. the code that we have built and used is described in some details in Appendix C.

### 4.2.1 General Formalism

We start off by writing the line-element in spherical symmetry as

$$ds^2 = -(\alpha^2 - \beta^2)dt^2 + 2\beta dt dr + \psi^4 a^2(t)(\hat{a}dr^2 + \hat{b}r^2 d\Omega^2). \quad (4.54)$$

$\alpha(t, r)$  is the lapse,  $\beta(t, r)$  is the radial component of the shift  $\beta_\mu$ ,  $\hat{a}$  and  $\hat{b}$  are the non-zero components of the diagonal conformal 3-metric.  $\psi^2\sqrt{a}$  is the conformal factor. Following Shibata et al. (Shibata and Sasaki 1999b), we have factored out the cosmological scale factor  $a(t)$ . The latter follows its own dynamics which serves as background. The extrinsic curvature is split into its trace  $K$  and its conformally-scaled trace-free part  $\hat{A}_{ij}$ ,

$$K_{\mu\nu} = \frac{1}{3}\gamma_{\mu\nu}K + \psi^4 a^2 \hat{A}_{\mu\nu}. \quad (4.55)$$

Due to spherical symmetry,  $\hat{A}_{\mu\nu}$  has only two non-zero components  $A_a := \hat{A}_r^r$  and  $A_b := \hat{A}_\theta^\theta$ . As  $\hat{A}_{\mu\nu}$  is traceless, one further has  $A_a + 2A_b = 0$ . The auxiliary 3-vector of the BSSN formalism, previously written as  $\hat{\Gamma}^i$  only has one non-zero component (Alcubierre and Mendez 2011),

$$\Delta^r = \frac{1}{\hat{a}} \left[ \frac{\partial_r \hat{a}}{2\hat{a}} - \frac{\partial_r \hat{b}}{\hat{b}} - \frac{2}{r} \left( 1 - \frac{\hat{a}}{\hat{b}} \right) \right]. \quad (4.56)$$

The BSSN formalism ensures that  $\det(\gamma_{\mu\nu}) = 1$  at all time which here translates to  $\hat{a}\hat{b}^2 = 1$ .

For our purpose, we shall limit ourselves to the zero-shift gauge  $\beta = 0$ . There is no formal difficulty in choosing a different gauge. This one however allows us to perform comparisons between cosmological models more straightforwardly.

The expressions of the energy source terms are similar to what we have given in the derivation of the LTB solution. The dynamics of space-time is given by the following set of evolution equations derived in Alcubierre et al. (Alcubierre

and Mendez 2011)<sup>(1)</sup>.

$$\partial_t \hat{a} = -2\alpha \hat{a} A_a, \quad (4.57)$$

$$\partial_t \hat{b} = -2\alpha \hat{b} A_b, \quad (4.58)$$

$$\partial_t \psi = -\frac{1}{6}\alpha \psi K - \frac{1}{2} \frac{\dot{a}}{a} \psi, \quad (4.59)$$

$$\partial_t K = -D^2 \alpha + \alpha (A_a^2 + 2A_b^2 + \frac{1}{3} K^2) + 4\pi \alpha (E + S_a + 2S_b), \quad (4.60)$$

$$\partial_t A_a = -\left(D^r D_r \alpha - \frac{1}{3} D^2 \alpha\right) + \alpha \left(R_r^r - \frac{1}{3} R\right) + \alpha K A_a - \frac{16\pi}{3} \alpha (S_a - S_b), \quad (4.61)$$

$$\begin{aligned} \partial_t \hat{\Delta}^r = & -\frac{2}{\hat{a}} (A_a \partial_r \alpha + \alpha \partial_r A_a) + 2\alpha \left(A_a \hat{\Delta}^r - \frac{2}{r \hat{b}} (A_a - A_b)\right) \\ & + \frac{\xi \alpha}{\hat{a}} \left[ \partial_r A_a - \frac{2}{3} \partial_r K + 6A_a \frac{\partial_r \psi}{\psi} + (A_a - A_b) \left(\frac{2}{r} + \frac{\partial_r \hat{b}}{\hat{b}}\right) - 8\pi j_r \right]. \end{aligned} \quad (4.62)$$

We fix  $\xi = 2$  as this is the standard BSSN optimal choice and guarantees strong hyperbolicity. The above equations feature the quantities  $R_r^r$ ,  $R$ ,  $D^r D_r \alpha$  and  $D^2 \alpha$  which are all combinations of the metric variables

$$\begin{aligned} R_r^r = & -\frac{1}{a \hat{a} \psi} \left[ \frac{\partial_r^2 \hat{a}}{2\hat{a}} - \hat{a} \partial_r \hat{\Delta}^r - \frac{3}{4} \left(\frac{\partial_r \hat{a}}{\hat{a}}\right)^2 + \frac{1}{2} \left(\frac{\partial_r \hat{b}}{\hat{b}}\right)^2 \right. \\ & - \frac{1}{2} \hat{\Delta}^r \partial_r \hat{a} + \frac{\partial_r \hat{a}}{r \hat{b}} + \frac{2}{r^2} \left(1 - \frac{\hat{a}}{\hat{b}}\right) \left(1 + \frac{r \partial_r \hat{b}}{\hat{b}}\right) \\ & \left. + 4 \frac{\partial_r^2 \psi}{\psi} - 4 \left(\frac{\partial_r \psi}{\psi}\right)^2 - 2 \left(\frac{\partial_r \psi}{\psi}\right) \left(\frac{\partial_r \hat{a}}{\hat{a}} - \frac{\partial_r \hat{b}}{\hat{b}} - \frac{2}{r}\right) \right]. \end{aligned} \quad (4.63)$$

$$\begin{aligned} R = & -\frac{1}{a \hat{a} \psi} \left[ \frac{\partial_r^2 \hat{a}}{2\hat{a}} + \frac{\partial_r^2 \hat{b}}{\hat{b}} - \hat{a} \partial_r \hat{\Delta}^r - \left(\frac{\partial_r \hat{a}}{\hat{a}}\right)^2 \right. \\ & + \frac{1}{2} \left(\frac{\partial_r \hat{b}}{\hat{b}}\right)^2 + \frac{2 \partial_r \hat{b}}{r \hat{b}} \left(3 - \frac{\hat{a}}{\hat{b}}\right) + \frac{4}{r^2} \left(1 - \frac{\hat{a}}{\hat{b}}\right) \\ & \left. + 8 \frac{\partial_r^2 \psi}{\psi} - 8 \left(\frac{\partial_r \psi}{\psi}\right) \left(\frac{\partial_r \hat{a}}{2\hat{a}} - \frac{\partial_r \hat{b}}{\hat{b}} - \frac{2}{r}\right) \right]. \end{aligned} \quad (4.64)$$

$$D^2 \alpha = \frac{1}{a \hat{a} \psi} \left[ \partial_r^2 \alpha - \partial_r \alpha \left(\frac{\partial_r \hat{a}}{2\hat{a}} - \frac{\partial_r \hat{b}}{\hat{b}} - 2 \frac{\partial_r \psi}{\psi} - \frac{2}{r}\right) \right]. \quad (4.65)$$

---

<sup>(1)</sup>We would like to point out a typo in the published version of the original article in which the factor of  $16\pi$  in Eq. (4.61) has been replaced by  $8\pi$

$$D^r D_r \alpha = \frac{1}{a \hat{a} \psi} \left[ \partial_r^2 \alpha - \partial_r \alpha \left( \frac{\partial_r \hat{a}}{2 \hat{a}} + 2 \frac{\partial_r \psi}{\psi} \right) \right]. \quad (4.66)$$

The evolution of the background space-time is given by the Friedmann equations

$$\frac{1}{\alpha_{\text{bkg}}^2} \left( \frac{\dot{a}}{a} \right)^2 = \frac{8\pi}{3} \rho_{\text{bkg}}, \quad (4.67)$$

$$\frac{1}{\alpha_{\text{bkg}}^2} \frac{\ddot{a}}{a} - \frac{\dot{a}}{a} \frac{\dot{\alpha}_{\text{bkg}}}{\alpha_{\text{bkg}}^3} = -\frac{8\pi}{6} (\rho_{\text{bkg}} + 3p_{\text{bkg}}), \quad (4.68)$$

where  $\rho_{\text{bkg}}$  and  $p_{\text{bkg}}$  are the homogeneous background energy density and pressure.

Solving the complete dynamics proceeds in two steps. A solution for the background is first found and then used to solve the local problem. The convergence and reliability of the method is monitored by means of the Hamiltonian and momentum constraints :

$$\mathcal{H} \equiv R - (A_a^2 + 2A_b^2) + \frac{2}{3} K^2 - 16\pi E = 0, \quad (4.69)$$

$$\mathcal{M}^r \equiv \partial_r A_a - \frac{2}{3} \partial_r K + 6A_a \frac{\partial_r \psi}{\psi} + (A_a - A_b) \left( \frac{2}{r} + \frac{\partial_r \hat{b}}{\hat{b}} \right) - 8\pi j_r = 0. \quad (4.70)$$

## 4.2.2 Boundary conditions

The space-time models under consideration are not asymptotically flat but rather go to the dynamical FLRW Universe at spatial infinity. The conditions imposed on the dynamical variables at the boundary of the computational domain must be specified accordingly. Arguably, the most efficient and straightforward way of imposing such boundary conditions is to constrain the inhomogeneous variables to behave like outward travelling spherical waves for large values of the radius. Mathematically,

$$f(t, r) = f_0(t) + \frac{h(r - vt)}{r}, \quad (4.71)$$

where  $f(t, r)$  represents any inhomogeneous field,  $f_0(t)$  is its homogeneous limit at spatial infinity and  $h(r - vt)$  is a plane wave scalar function. This is solution to

$$\partial_t f = \partial_t f_0 - v \partial_r f - \frac{v}{r} (f - f_0), \quad (4.72)$$

where  $v$  is the characteristic velocity of the field on the spatial domain. It is obtained by examining the characteristics of the dynamical equation for each field and corresponds to the speed of light for most of the space-time variables. In our numerical treatment, we replace the dynamical equation of every variables by one of the shape of Eq. (4.72) for the few outermost points of the computational grid. This ensures that any signal reaching the outer

boundary of the grid will simply decay and will not get reflected into the computational domain.

The asymptotical values of each variables are

$$\hat{a}(t, r), \hat{b}(t, r), \psi(t, r) \rightarrow 1, \quad (4.73)$$

$$\alpha(t, r) \rightarrow \alpha_{\text{bkg}}(t), \quad (4.74)$$

$$A_a(t, r), A_b(t, r), \hat{\Delta}^r(t, r) \rightarrow 0, \quad (4.75)$$

$$K(t, r) \rightarrow -3 \frac{1}{\alpha_{\text{bkg}}} \frac{\dot{a}}{a}. \quad (4.76)$$

### 4.2.3 Implementation

The radial dimension is discretised as a uniform cell-centred grid. Radial derivatives are computed with fourth-order finite difference methods. Spherical symmetry simplifies the problem as one needs only consider a single spatial dimension. However, it also brings out terms of the form  $1/r^p$  within the dynamical equations. These ought to be taken care of carefully as these could lead to numerical instabilities. In the present work, these terms are treated by using a *Partially Implicit Runge-Kutta Method* evolution scheme (PIRK) (Cordero-Carrión and Cerdá-Durán 2014). This evolution method can be used whenever the set of dynamical equations can be split into two groups

$$\begin{aligned} \partial_t u &= \mathcal{L}_1(u, v) \\ \partial_t v &= \mathcal{L}_2(u) + \mathcal{L}_3(u, v). \end{aligned} \quad (4.77)$$

The variables grouped under the common label “ $u$ ” are first evolved explicitly. The result is then used to evolve the group labelled “ $v$ ” using a partially implicit scheme. The discretised version of Eqs. (4.77), used in this work is second order. From  $(u^n, v^n)$ , the values of the functions  $u$  and  $v$  at time-step  $t_n$ , one computes an approximate solution at time step  $t_{n+1}$  denoted by  $(u^{(1)}, v^{(1)})$ . A corrected solution  $(u^{n+1}, v^{n+1})$  is then obtained. The scheme reads :

$$u^{(1)} = u^n + \Delta t L_1(u^n, v^n), \quad (4.78)$$

$$v^{(1)} = v^n + \Delta t \left[ \frac{1}{2} L_2(u^n) + \frac{1}{2} L_2(u^{(1)}) + L_3(u^n, v^n) \right], \quad (4.79)$$

$$u^{n+1} = \frac{1}{2} \left[ u^n + u^{(1)} + \Delta t L_1(u^{(1)}, v^{(1)}) \right], \quad (4.80)$$

$$v^{n+1} = v^n + \frac{\Delta t}{2} \left[ L_2(u^n) + L_2(u^{n+1}) + L_3(u^n, v^n) + L_3(u^{(1)}, v^{(1)}) \right]. \quad (4.81)$$

The PIRK scheme has already been applied to the BSSN formalism in spherical symmetry for a non-dynamical background (Montero and Cordero-Carrión 2012). The cosmological variables  $a$  and  $\alpha_{\text{bkg}}$  are first evolved explicitly along

with  $\hat{a}$ ,  $\hat{b}$  and  $\psi$ . The updated values are then used to obtain  $\dot{a}$ ,  $K$  and  $A_a$ . Finally all the updated values are used to obtain  $\hat{\Delta}^r$ .

A few virtual points of negative radius are added to the numerical grid to compute the radial derivatives close to the origin. Specifying the correct parity of the fields across the origin contributes to the stability of the numerical variables. We use 4<sup>th</sup> order Kreiss-Oliger dissipation. Details on the operator splitting used in our analysis are given in Appendix B.

#### 4.2.4 Evolution on a de Sitter background

Before actually coming to consider the spherical collapse of matter, we wish to test our method on a simpler case where the Universe is filled with a constant homogeneous vacuum energy density satisfying  $p_{\text{bkg}} = -\rho_{\text{bkg}}$ . This is equivalent to the empty de Sitter Universe with a cosmological constant  $\Lambda = 8\pi\rho_{\text{bkg}}$ . Keeping the Universe homogeneous, we study the dynamics of an initially gaussian gauge pulse, generalising the approach of Alcubierre et al. (Alcubierre and Mendez 2011) to dynamical backgrounds. The shape of the initial pulse is

$$\alpha(t = 0, r) = \alpha_{\text{bkg}}^i + \frac{\alpha_0 r^2}{1 + r^2} \left[ e^{-\frac{(r-r_i)^2}{\sigma^2}} + e^{-\frac{(r+r_i)^2}{\sigma^2}} \right], \quad (4.82)$$

where  $\alpha_{\text{bkg}}^i = \alpha_{\text{bkg}}(t = 0)$  and  $\alpha_0$  is a constant setting the amplitude of the initial pulse. Fixing  $\alpha_{\text{bkg}}^i = 1$  allows to write the initial Hubble factor as  $H_i := \frac{\dot{a}_i}{a_i}$ . Since the energy density remains constant throughout the integration, by virtue of the Friedmann equation, so does the Hubble factor:

$$\frac{1}{\alpha_{\text{bkg}}} \frac{\dot{a}}{a} = H_i, \quad \forall t. \quad (4.83)$$

The energy density is equal to

$$E = \rho_{\text{bkg}} = \frac{3}{8\pi} H_i^2. \quad (4.84)$$

Assuming spatial homogeneity at initial time, we set

$$\hat{a}(t = 0) = \hat{b}(t = 0) = \psi(t = 0) = 1. \quad (4.85)$$

This reduces the constraint equations to (upon remembering that  $A_b = -A_a/2$ ).

$$\frac{3}{2} A_a^2 + \frac{2}{3} K^2 - 6 H_i^2 = 0, \quad (4.86)$$

$$\partial_r A_a - \frac{2}{3} \partial_r K + 3 \frac{A_a}{r} = 0. \quad (4.87)$$

Intrestingly, upon setting  $x = 3A_a$ ,  $y = 2K$ , these get rewritten as

$$x^2 + y^2 = 36 H_i^2, \quad (4.88)$$

$$\partial_r x - \partial_r y + 3 \frac{x}{r} = 0, \quad (4.89)$$

the former of which is the implicit equation of a circle of radius  $6H_0$ . By writing  $x = 6H_i \cos \theta$ ,  $y = 6H_i \sin \theta$ , the solution to Eq. (4.89) can be written as

$$-e^\theta \cos \theta = Cr^3 , \quad (4.90)$$

With  $C$ , some integration constant. The general solution of this for  $C \neq 0$  allows  $r$  to take only discrete values. One thus sets  $C = 0$  so that  $\cos \theta = 0$  and

$$K = \pm 3H_i, \quad A_a = 0. \quad (4.91)$$

The minus sign corresponds to an expanding background, the plus sign to a contracting background. We are only interested in the expanding solution.

The gauge dynamics study is performed in the Bona-Masso slicing in which the equation for the lapse is

$$\partial_t \alpha = -\alpha^2 f(\alpha) K . \quad (4.92)$$

Torres et al. (Torres, Alcubierre, Diez-Tejedor and Núñez 2014) have argued that imposing  $f \leq 1/3$  ensures that the coordinate speed of light remains finite and thus the scheme remains stable. The line-element for a ray of light moving radially is

$$ds^2 = 0 = -\alpha^2 dt^2 + a^2 dr^2 . \quad (4.93)$$

The module of the coordinate speed of light is then

$$v_c := \frac{dr}{dt} = \frac{\alpha}{a} , \quad (4.94)$$

the variation of which is

$$\frac{dv_c}{dt} = \frac{\dot{\alpha}}{a} - \alpha \frac{\dot{a}}{a^2} . \quad (4.95)$$

Imposing the Bona-Masso slicing then gives, assuming expansion so that  $K = -\frac{3}{\alpha} \frac{\dot{a}}{a}$ ,

$$\frac{dv_c}{dt} = 3\alpha f(\alpha) \frac{\dot{a}}{a^2} - \alpha \frac{\dot{a}}{a^2} , \quad (4.96)$$

in order for the velocity to remain finite, one imposes

$$\begin{aligned} 3\alpha f(\alpha) \frac{\dot{a}}{a^2} - \alpha \frac{\dot{a}}{a^2} &\leq 0 \\ f(\alpha) &\leq 1/3 . \end{aligned} \quad (4.97)$$

Note that the geodesic slicing corresponds to  $f = 0$  which implies

$$-\frac{\dot{a}}{a^2} \leq 0 . \quad (4.98)$$

This is verified as long as expansion is assumed ( $\dot{a} \geq 0$ ).

The choice of the Bona-Masso slicing for the entire domain also fixes the gauge of the cosmological background dynamics through

$$\dot{\alpha}_{\text{bkg}} = 3\alpha_{\text{bkg}}f(\alpha_{\text{bkg}})\frac{\dot{a}}{a} . \quad (4.99)$$

The only two independent variables for the background are  $a$  and  $\alpha_{\text{bkg}}$ . We choose to solve Eqs. (4.68) and (4.99) which upon inserting Eq. (4.83) become

$$\dot{\alpha}_{\text{bkg}} = \alpha_{\text{bkg}}^2 f(\alpha_{\text{bkg}}) H_i \quad (4.100)$$

$$\frac{\ddot{a}}{a} = 4\alpha_{\text{bkg}}^2 H_i . \quad (4.101)$$

We then use Eq. (4.67) as a constraint equation to monitor the error.

In order to witness a significant departure from flat space-time, we set  $H_i = 0.02$  as the initial Hubble factor. The expansion is then exponential for time scales beyond order  $t \sim 10$ .

Working in the harmonic gauge ( $f = 1$ ) imposes to reduce the value of the Courant-Friedrichs-Lewy factor (CFL) to  $\Delta t/\Delta r = 0.25$  for stability (Requier et al. 2015). Choosing  $f \leq \frac{1}{3}$  allows to use large values of the CFL factor. In what follows, we have set  $f = 0.333$  and  $\Delta t/\Delta r = 0.5$ . The dynamics of the lapse is that of a travelling wave. Fig. 4.1 shows the radial profile of  $\alpha$  at different times. As expected from the initial data, the initial pulse splits into two parts moving in opposite directions. The homogeneous part of the solution follows the evolution of  $\alpha_{\text{bkg}}$  imposed at the outer boundary which is plotted on Fig. 4.2 along with the scale factor  $a(t)$ . The two curves are very similar as they should be. Indeed, from Eq. (4.99) with  $f = 1/3$ , one gets  $\alpha_{\text{bkg}} = Ca$ . Imposing  $\alpha_{\text{bkg}}(t = 0) = a(t = 0) = 1$  sets the constant of integration  $C = 1$  and the two functions are equal. So far as the background is concerned, the gauge condition  $f = 1/3$  is thus equivalent to the cosmological *conformal gauge* in which the time coordinate  $\eta$  is linked to the synchronous time  $t$  through  $dt = ad\eta$ .

Figure 4.3 shows the  $L^2$ -norm of the Hamiltonian and momentum constraints as functions of time. These indicate that the error is maximal when the inward moving pulse hits the left boundary ( $r=0$ ). It then goes down to its minimal value as the two pulses travel outward.

The above results were obtained with a spatial resolution of  $\Delta r = 0.05$ . In order to prove the reliability of our method, we have plotted the Hamiltonian constraint violation for three values of the spatial resolution on Fig. 4.4. The similarity in the shapes of the curves and the way the error is rescaled when the resolution is doubled indicate stability and better than second-order convergence. The error is maximal at the centre of coordinates yet remains controlled throughout the integration. The maximum violation of the Hamiltonian constraint is due to a remanent of the initial gauge pulse around  $r = 5$ . The above-second-order convergence at this point indicates that the dominant part of the error should be due to the numerical discretisation of spatial derivatives which is 4th-order. The violation around the travelling pulses at late time

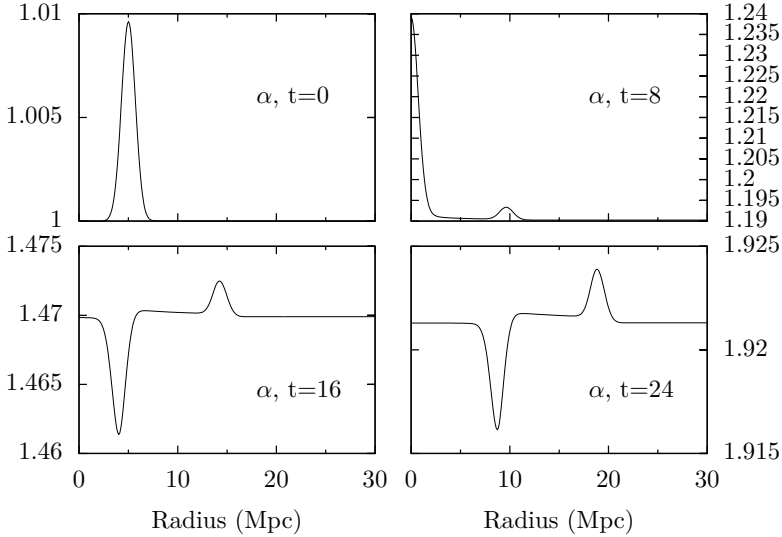


Figure 4.1 – Time evolution of the radial profile of the lapse  $\alpha$ .

is shown on the inner plot of Fig. 4.4. The order of convergence is closer yet still above second order.

### 4.2.5 Spherical collapse of dust matter

We now apply the method to the study of spherical collapse of pressure-less matter and confront the results to the LTB solutions. In order to allow direct comparison, we use the geodesic slicing  $\alpha = 1$ .

It is useful for us to rewrite the LTB line-element, Eq. (4.39) as

$$ds^2 = -dt^2 + \frac{a_{\perp}^2(t, r)}{1 + 2E_{1tb}(r)} + a_{\perp}^2(t, r)r^2 d\Omega^2, \quad (4.102)$$

with  $a_{\parallel} := \partial_r(ra_{\perp})$ .

One of the main interests of the geodesic slicing resides in the simplicity of the evolution equation for the energy density. Eq. (2.31) for the conservation of energy reduces to

$$\begin{aligned} \partial_t \rho - K\rho &= 0 \\ \partial_t \rho + \frac{1}{2}(\gamma^{rr} \partial_t \gamma_{rr} + 2\gamma^{\theta\theta} \partial_t \gamma_{\theta\theta}) &= 0. \end{aligned} \quad (4.103)$$

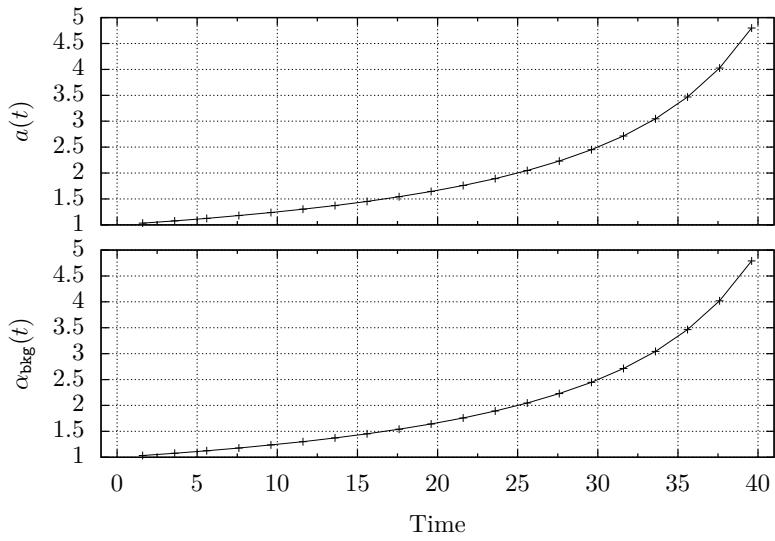


Figure 4.2 – Evolution of the homogeneous lapse and scale factor  $\alpha_{\text{bkg}}(t)$  and  $a(t)$ .

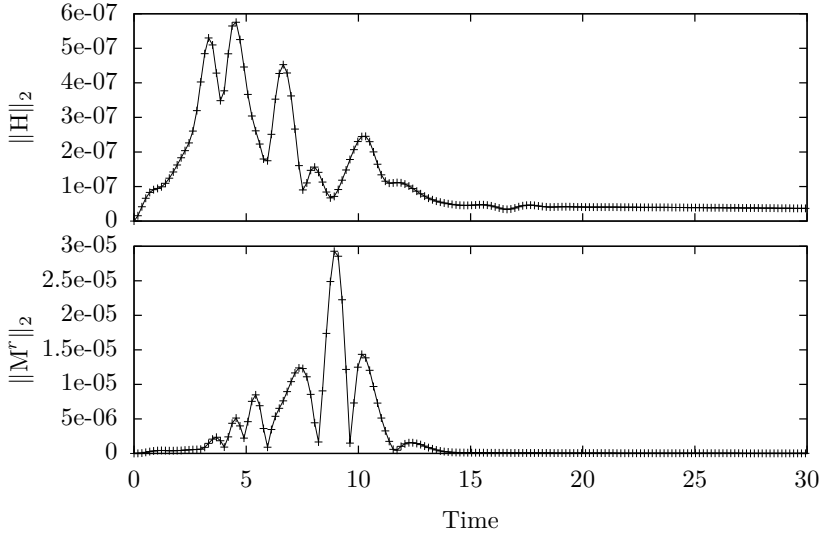


Figure 4.3 –  $L^2$ -norm of the Hamiltonian and momentum constraints.

Plugging in the expression of the metric components read from Eq. (4.54), the solution of the above is simply

$$\rho = \rho_0 \left( \frac{a_0^3 \psi_0^6}{a^3 \psi^6} \right), \quad (4.104)$$

where  $\rho_0$ ,  $a_0$  and  $\psi_0$  are initial values and we have used  $\hat{a}b^2 = 1$ . This solution generalises the rescaling equation for dust densities in cosmology to the case of non-homogeneous space-time. In the LTB coordinates, the rescaling equation reads

$$\rho = \rho_0 \frac{a_{\parallel}^0 a_{\perp}^0{}^2}{a_{\parallel} a_{\perp}^2}. \quad (4.105)$$

It can be shown that this is equivalent to Eq. (4.43) at all time which, in the coordinates of Eq. (4.102) reads

$$\rho = \frac{\partial_r M}{4\pi a_{\parallel} a_{\perp}^2 r^2}, \quad (4.106)$$

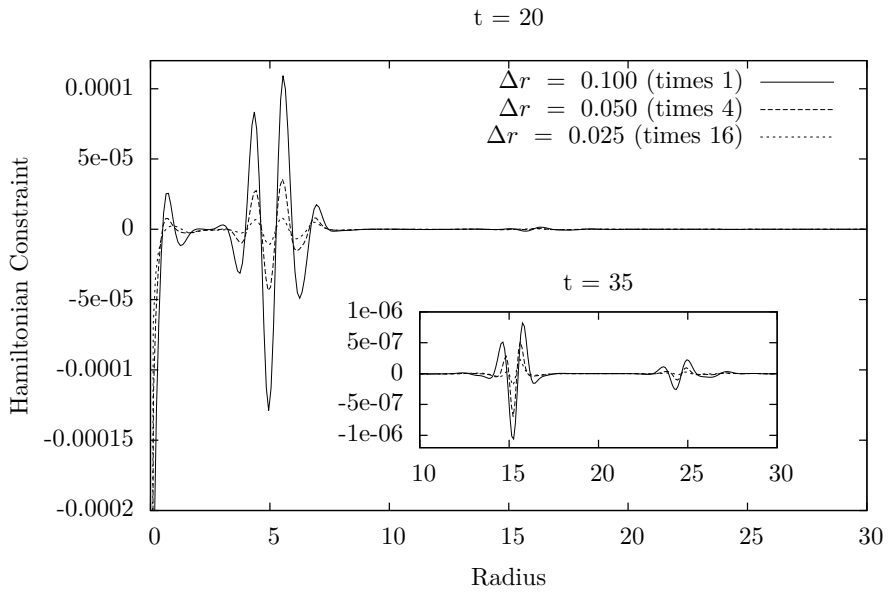


Figure 4.4 – Radial profile of the absolute violation of the Hamiltonian constraint for 3 values of the spatial resolution.

whereas the evolution equations read

$$\frac{\dot{a}_\perp^2}{a_\perp^2} = \frac{2M(r)}{a_\perp^3 r^3} + \frac{2}{r^2} \frac{E_{1\text{tb}}}{a_\perp^2} \quad (4.107)$$

$$\frac{\ddot{a}_\perp}{a_\perp} = -\frac{M(r)}{a_\perp^3 r^3} . \quad (4.108)$$

### 4.2.6 Initial data

Building the initial data for the evolution of the LTB solution involves to specify the initial profiles of 3 functions among  $a_\perp$ ,  $\dot{a}_\perp$ ,  $E_{1\text{tb}}$ ,  $\rho$  and  $M$ . The remaining variables can then be inferred from Eqs. (4.107) and (4.108). For the purpose of comparing the results in the LTB and BSSN coordinates, it is arguably easier to build the initial data in the BSSN coordinates as the constraint equations are clearly separate from the evolution equations.

$$\begin{aligned} \hat{a}(t=0, r) &= \hat{b}(t=0, r) = 1 , \\ E(t=0, r) &= [1 + \delta_m^i(r)] \rho_{\text{bkg}}^i , \end{aligned} \quad (4.109)$$

where  $\rho_{\text{bkg}}^i := \rho_{\text{bkg}}(t=0)$  and  $\delta_m^i(r) := \delta_m(t=0, r)$ . The choice of the initial curvature fixes the cosmological expansion factor for the whole domain. We set it to the homogeneous background value so that

$$K(t=0) = -3H_i ; A_a(t=0) = A_b(t=0) = 0 . \quad (4.110)$$

This imposes

$$H_i = \frac{\dot{a}_i}{a_i} = \gamma^{rr} \partial_t \gamma_{rr} |_{t=0} = \gamma^{\theta\theta} \partial_t \gamma_{\theta\theta} |_{t=0} . \quad (4.111)$$

The equation for the initial value of the conformal factor is found by plugging the above conditions into the Hamiltonian constraint which then reduces to

$$a^{-2} \psi^{-5} (\partial_r^2 \psi + \frac{2}{r} \partial_r \psi) + 6H_i^2 = 16\pi \rho_{\text{bkg}}^i (1 + \delta_m^i(r)) . \quad (4.112)$$

By virtue of the Friedmann equation, this becomes

$$\partial_r \psi + \frac{2}{r} \partial_r \psi = 16\pi \rho_{\text{bkg}}^i \delta_m^i(r) a_i^2 \psi^5 . \quad (4.113)$$

Following Shibata et al., this equation is solved numerically as a boundary value problem with the conditions

$$\partial_r \psi \rightarrow 0, \quad \text{for } r \rightarrow 0 ; \quad (4.114)$$

$$\psi \rightarrow 1 + \frac{C_\psi}{2r}, \quad \text{for } r \rightarrow \infty . \quad (4.115)$$

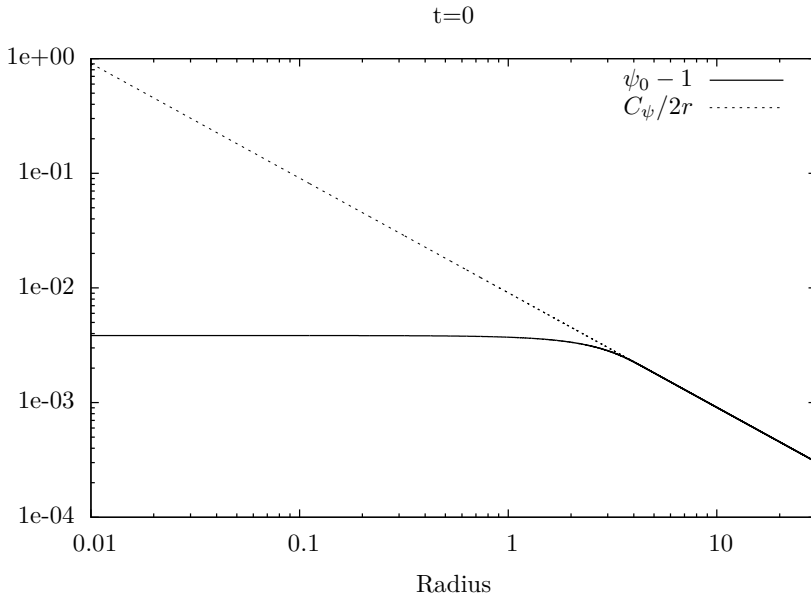


Figure 4.5 – Initial conformal factor and asymptotical value at infinity.

The first condition ensures regularity at the centre of coordinates, the second ensures asymptotic homogeneity. The parameter  $C_\psi$  is adjusted by specifying the following additional outer boundary condition:

$$\partial_r \psi \rightarrow \frac{-C_\psi}{2r^2}, \quad \text{for } r \rightarrow \infty. \quad (4.116)$$

In this section, we use an initial density contrast function of the form

$$\delta_m^i(r) = \delta_m^i \exp\left(-\frac{r^2}{r_{\text{span}}^2 - r^2}\right), \quad (4.117)$$

where  $\delta_m^i$  and  $r_{\text{span}} > 0$  are constants. This profile has the property of being smooth and to have a compact support spanning the region  $[0, r_{\text{span}}]$ . We use different profiles later in this work leading to similar successes.

The solution to the initial boundary value problem is shown on Fig. 4.5 for  $\delta_m^i = 0.1$  and  $r_{\text{span}} = 5$  (plain line). Its behaviour agrees well with the imposed asymptotical solution (dashed line). The initial data for the BSSN metric functions can easily be translated into the LTB variables. Since the analysis is performed in the zero shift gauge, it can be assumed that the radius coordinate in both systems should only differ up to a constant factor throughout the integration. Setting this equal to one in the initial data allows to compare the metric components from both sets directly.

Direct comparison of Eq. (4.54) and Eq. (4.102) gives

$$a_{\perp}^i = \psi_i^2 a_i, \quad (4.118)$$

$$a_{\parallel}^i = \psi_i^2 a_i + 2\psi_i \frac{d\psi_i}{dr} a_i r. \quad (4.119)$$

By identifying  $\gamma_{rr}$  from both coordinates systems, one then finds the value of the energy function  $E_{\text{1tb}}$ . In agreement with Eq. (4.111), the initial time derivatives are

$$\dot{a}_{\perp}^i = a_{\perp}^i H_i, \quad \dot{a}_{\parallel}^i = a_{\parallel}^i H_i. \quad (4.120)$$

The function  $M(r)$  is deduced from Eq. (4.107).

### 4.2.7 Comparison with LTB

The background space-time is evolved numerically using the acceleration equation which here reduces to

$$\frac{\ddot{a}}{a} = -\frac{8\pi}{6} \rho_{\text{bkg}}. \quad (4.121)$$

The dust energy density is evolved by means of Eq. (4.103). Fig. 4.6 shows the result of the evolution of  $\gamma_{rr}$  and  $\gamma_{\theta\theta}$  solving the LTB system of ODEs (lines) and the general system of PDEs of BSSN (markers) up to  $t = 15$ . The shapes of the curves undergo a rapid change at the beginning of integration. These then remain unchanged for subsequent time values and simply get rescaled. The curves from both BSSN and LTB agree very well at all time and the maximum of the relative difference between these is of the order  $\sim 10^{-5}$ .

### 4.2.8 Long time evolution

We now wish to move on to considering long time evolution dynamics. In order to look for results that would be of practical use to the cosmologist, we have disposed of the usual units of Numerical Relativity in favour of others more suited about which we ought to say a few words.

We work in natural units with  $G = c = 1$ . In order to fully define the system, one needs to set the value of some other constant (see Appendix A). We have chosen this to be the Hubble factor measured today,

$$H_0 = x t_{\text{scale}}^{-1}, \quad (4.122)$$

with  $x$ , some adjustable parameters. Comparison with the experimental value of  $\sim 70\text{km/s/Mpc}$  sets the time scale  $t_{\text{scale}}$ . The length and mass scales are then obtained from  $l_{\text{scale}} = ct_{\text{scale}}$  and  $m_{\text{scale}} = (c^3/G)t_{\text{scale}}$ . One can dispose of the need to specify the particular set of scales employed within a computation by expressing these in terms of  $H_0$ .

Fig. 4.7 shows the evolution of the background scale factor as well as the local central scale factor defined as the product  $a^2(t)\psi(t, r = 0)$ . The code proceeds until the collapse without difficulty. The initial Hubble factor is  $H_i =$

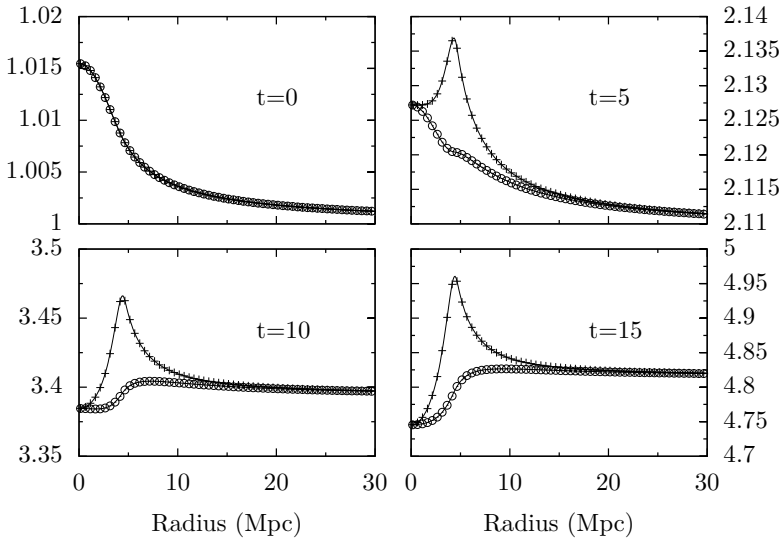


Figure 4.6 – Spatial metric functions in the BSSN and LTB variables at early time. The top curves of each plot correspond to  $\gamma_{rr}$ , the bottom curves correspond to  $\gamma_{\theta\theta}/r^2$ .

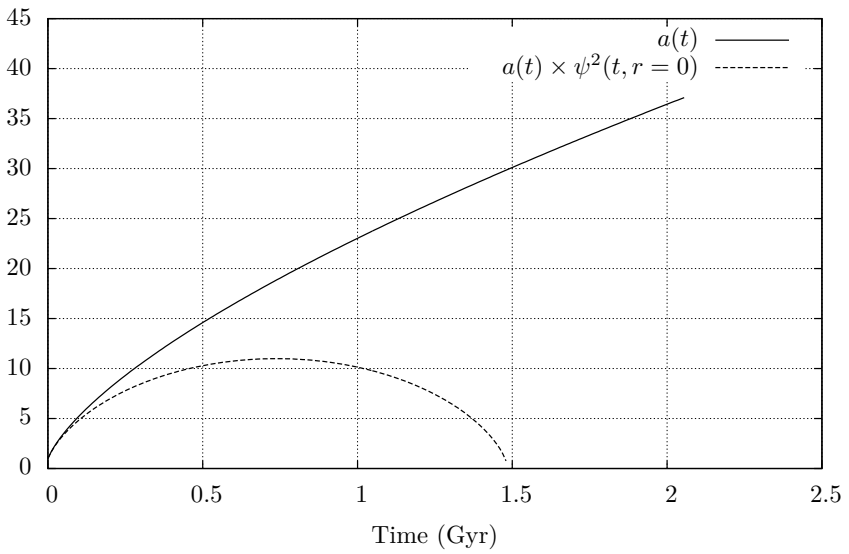


Figure 4.7 – Background and the central scale factors for a Universe full of dust.

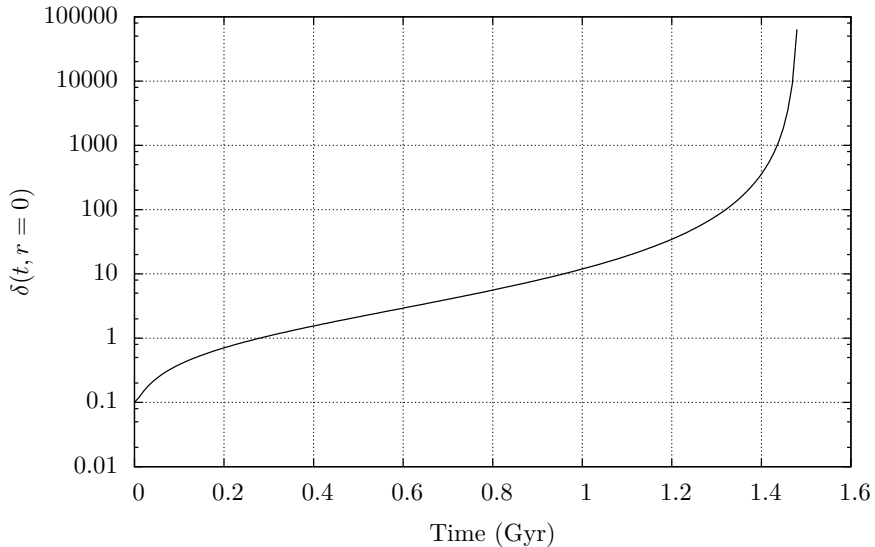


Figure 4.8 – Central value of the density contrast for a Universe full of dust.

$10^3 H_0$  and the initial density contrast  $\delta_m^i = 0.1$ . The structure collapse on time scales of the order  $t \sim 1$  Gyr. The initial span of the over-density is  $r_{\text{span}} = \frac{5 \times 10^{-4}}{H_0} \sim 10$  Mpc. The evolution of the central value of the density contrast is shown on Fig. 4.8. It grows rapidly into its non-linear regime. The complete density contrast profile is shown on Fig. 4.9. Its amplitude grows exponentially as its shape departs from the initial bump function. It is however interesting to notice that the profile does not spread outward. The stability of the method is best analysed by inspection of the  $L^2$ -norm of the Hamiltonian constraint shown on Fig. 4.10. The rescaling following the increase in the resolution indicates above second-order convergence. Its steep increase at the end of the numerical integration corresponds to the time of the collapse.

### 4.2.9 Spherical Collapse of a scalar field

We now turn to the case mentioned in the beginning of this chapter where the Universe is not simply filled with dust matter but also contains a quintessence scalar field. In such case, the shape of the stress-energy tensor, in particular, the presence of momentum transfer renders the LTB solution invalid.

We start by giving the evolution equations for the scalar field and the energy source terms induced. The conservation law  $\nabla_\mu T_\nu^\mu = 0$  leads to the Klein-

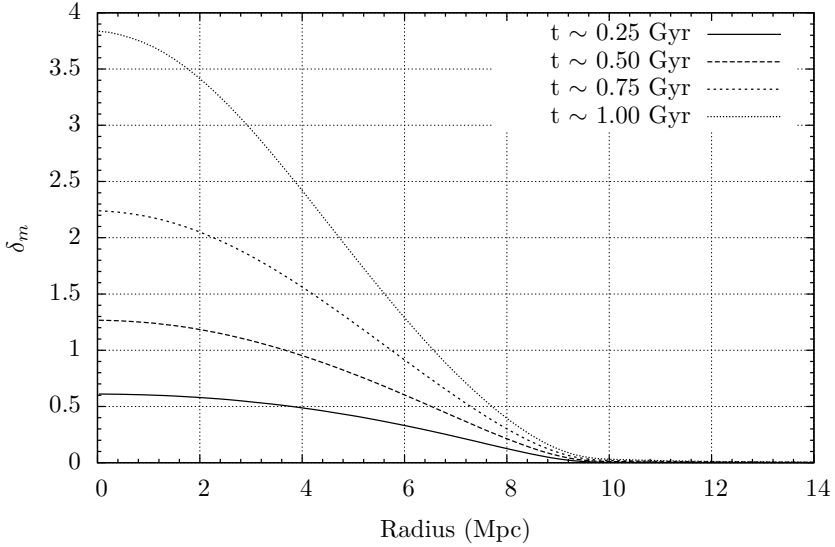


Figure 4.9 – Evolution of the density contrast profile for a Universe full of dust.

Gordon equation:

$$\partial_\mu \left( (-g)^{1/2} \partial^\mu \phi \right) = (-g)^{1/2} \partial_\phi V . \quad (4.123)$$

In order to write this as a first order system, one defines (Torres et al. 2014)

$$\Pi := n^\mu \partial_\mu \phi , \quad (4.124)$$

$$\Psi_i := \partial_i \phi . \quad (4.125)$$

Assuming spherical symmetry, the evolution equation can be written as (using the short-hand  $\Psi \equiv \Psi_r$ )

$$\mathcal{L}_n \phi = \Pi , \quad (4.126)$$

$$\mathcal{L}_n \Psi = \frac{1}{\alpha} \partial_r (\alpha \Pi) , \quad (4.127)$$

$$\mathcal{L}_n \Pi = K \Pi + \frac{1}{\alpha} D_r (\alpha \Psi) - \frac{dV}{d\phi} . \quad (4.128)$$

In presence of both matter and scalar field, the energy source functions have

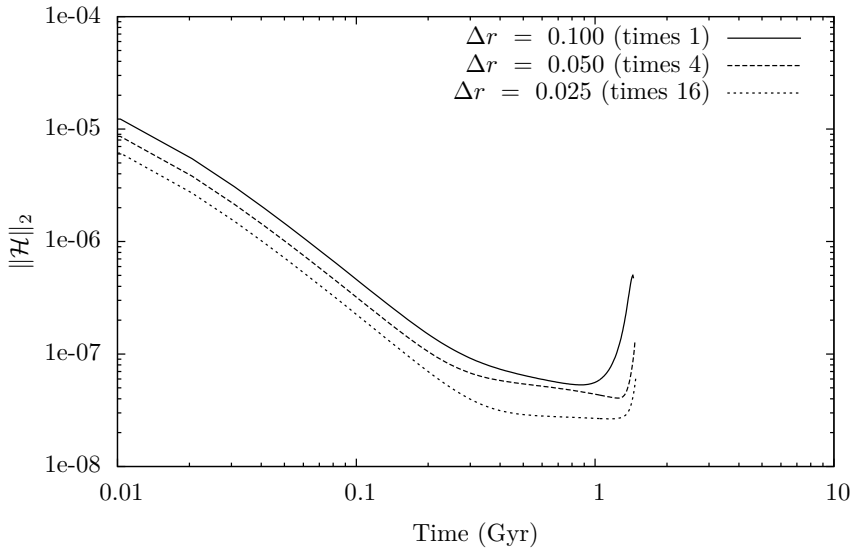


Figure 4.10 –  $L^2$ -norm of the Hamiltonian constraint violation in time following the evolution of a dust matter over-density.

two components

$$E = E_m + E_\phi , \quad (4.129)$$

$$S_a = S_a^m + S_a^\phi , \quad (4.130)$$

$$S_b = S_b^m + S_b^\phi , \quad (4.131)$$

$$j_r = j_r^m + j_r^\phi . \quad (4.132)$$

The expressions of the components associated with the scalar field read

$$E_\phi = \frac{1}{2} \left( \Pi^2 + \frac{\Psi^2}{\psi^4 a^2 \hat{a}} \right) + V , \quad (4.133)$$

$$S_a^\phi = \frac{1}{2} \left( \Pi^2 + \frac{\Psi^2}{\psi^4 a^2 \hat{a}} \right) - V , \quad (4.134)$$

$$S_b^\phi = \frac{1}{2} \left( \Pi^2 - \frac{\Psi^2}{\psi^4 a^2 \hat{a}} \right) - V , \quad (4.135)$$

$$j_r^\phi = -\Pi\Psi . \quad (4.136)$$

In the zero shift gauge, the evolution equations reduce to (using  $\hat{a}\hat{b}^2 = 1$ ).

$$\partial_t \Pi = \alpha K \Pi - \frac{1}{\psi^6 a^2 r^2} \partial_r \left( \alpha \frac{\psi^2 r^2}{\hat{a}} \Psi \right) - \alpha \frac{dV}{d\phi} , \quad (4.137)$$

$$\partial_t \Psi = \partial_r (\alpha \Pi) , \quad (4.138)$$

$$\partial_t \phi = \alpha \Pi . \quad (4.139)$$

Before we undertake the study of spherical collapse with quintessence, we want to investigate the dynamics of the scalar field when there is no dust matter.

The choice of the scalar potential is crucial in cosmology as its shape influences the background dynamics. In this section, we use the inverse power-law Ratra-Peebles model (Peebles and Ratra 2003)

$$V(\phi) = \frac{M^{4+n}}{\phi^n} . \quad (4.140)$$

This model is used to produce late-time cosmological acceleration. In the general case where the field is not initially at rest, the slow-roll conditions are not satisfied at initial time as the field starts with a small value corresponding to a steep region of the potential. When it is present, the dust matter density dominates over the energy density and the Universe assumes a power-law expansion in time  $a \sim t^{2/3}$  during which  $\phi$  rolls down its potential. The field eventually comes to the flat tail region of the potential where the slow-roll conditions are met leading to a de Sitter expansion phase. If the field is initially at rest, the evolution proceeds in the same way but starts with another de Sitter phase.

We start off by looking at the evolution of a spatial distribution of scalar field similar to the lapse profile of Sec. 4.2.4

$$\phi = \phi_{\text{bkg}}(1 + \delta\phi) , \quad (4.141)$$

$$\delta\phi(t = 0, r) = \frac{\delta\phi_0 r^2}{1 + r^2} \left[ e^{-\frac{(r-r_i)^2}{\sigma^2}} + e^{-\frac{-(r+r_i)^2}{\sigma^2}} \right] . \quad (4.142)$$

The background field is chosen as the solution to

$$H_i^2 = \frac{8\pi}{3} V(\phi_{\text{bkg}}) \quad (4.143)$$

which is just the Friedmann equation with  $\alpha = 1$ . Once the  $\phi$  distribution is known, the initial data are set after imposing

$$\hat{a}(t = 0) = \hat{b}(t = 0) = 1 , \quad (4.144)$$

$$K(t = 0) = -3H_i ; A_a(t = 0) = A_b(t = 0) = 0 . \quad (4.145)$$

This reduces the Hamiltonian constraint to

$$a^{-2}\psi^{-5}(\partial_r^2\psi + \frac{2}{r}\partial_r\psi) + 6H_i^2 = 16\pi E_\phi . \quad (4.146)$$

This is solved by imposing the same conditions as in Sec. 4.2.6.

We perform two simulations each one corresponding to a different value of the initial expansion factor. The potential parameters are chosen in order for the field to reproduce the behaviour of a cosmological constant when the field has a value around  $\phi_0 \sim \sqrt{8\pi}$  (Amendola and Tsujikawa 2010).

$$8\pi V(\phi_0) = \Lambda . \quad (4.147)$$

The initial amplitude of the scalar field inhomogeneity parameters are  $\delta\phi_0 = 5 \times 10^{-4}$ ,  $\sigma = 2$  and  $r_i = 20$ . The field is assumed to be initially at rest ( $\dot{\phi}(t = 0) = \Pi(t = 0) = 0$ ). Eq. (4.146) then turns into

$$a^{-2}\psi^{-5}(\partial_r^2\psi + \frac{2}{r}\partial_r\psi) + 6H_i^2 = 8\pi \left( \frac{\Psi^2}{\psi^4 a^2 \hat{a}} \right) + 16\pi V(\phi) . \quad (4.148)$$

We first study the evolution of the field in the case where the initial expansion factor is of the order of the present day Hubble factor ( $H_i = 5H_0$ ). The evolution of the scale factor and the homogeneous part of the scalar field are shown on Fig. 4.11. The Universe starts off in a phase of de Sitter expansion as the slow-roll conditions are met at initial time. The field rapidly unfreezes as it rolls down its potential leading to a milder expansion rate before eventually freezing out again in the tail of its potential. The scalar pulse propagation happens within the early de Sitter phase. The potential part of the field energy density dominates over the term proportional to  $\Psi$  at initial time. The evolution of the scalar field profile in the geodesic slicing is shown on Fig. 4.12.

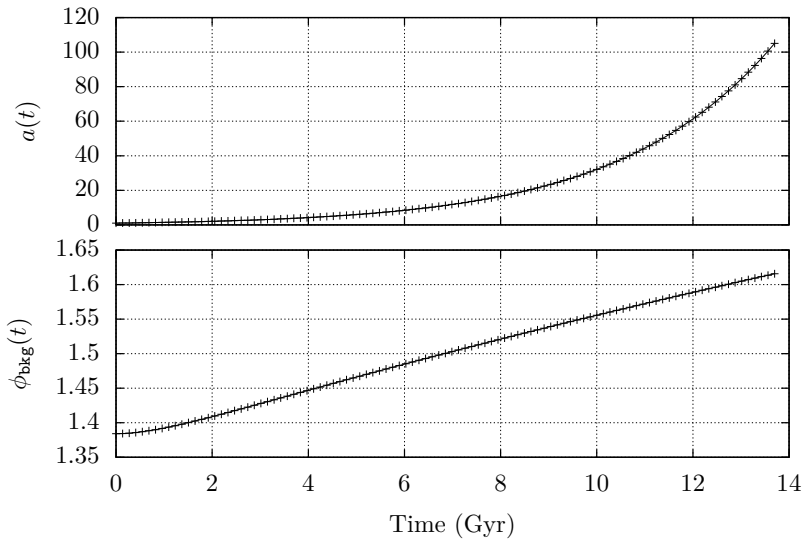


Figure 4.11 – Long-term cosmological evolution of the scale factor and background scalar field for a Universe filled with quintessence ( $H_i = 5H_0$ ).

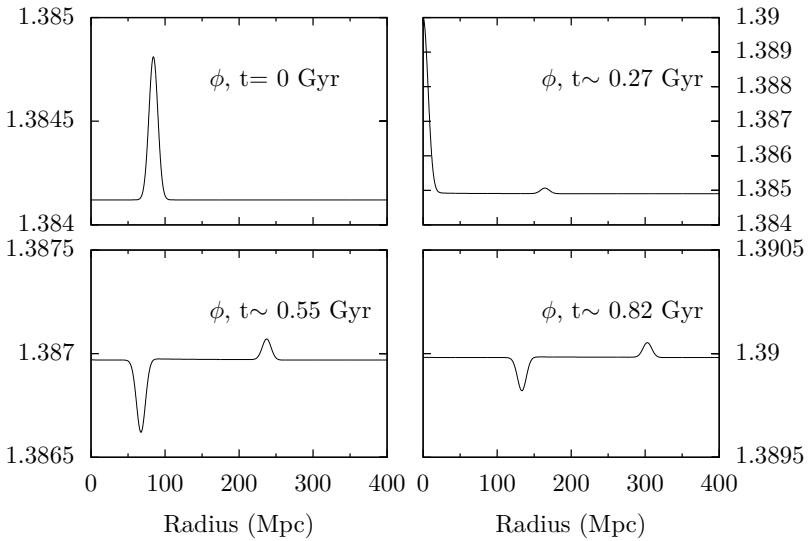


Figure 4.12 – Evolution of a Gaussian quintessence scalar pulse profile on a de Sitter background ( $H_i = 5H_0$ ).

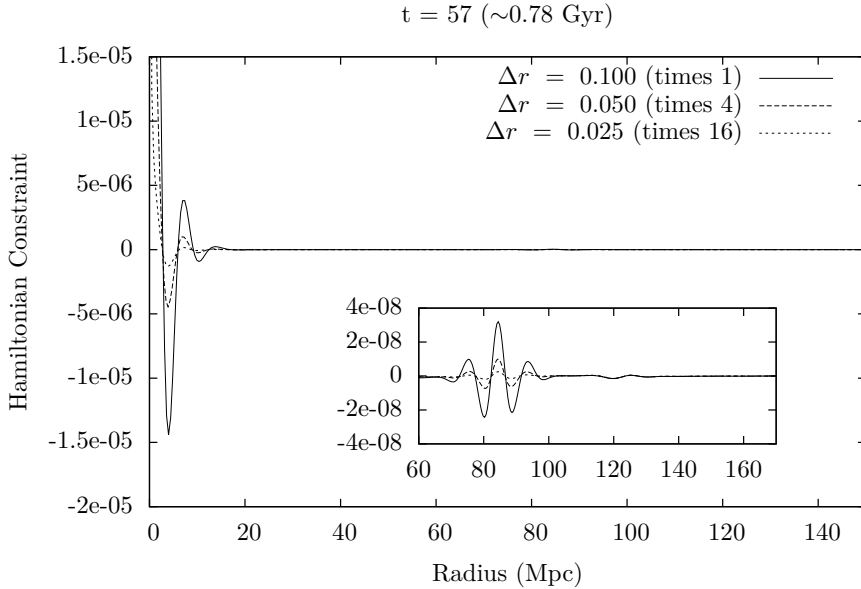


Figure 4.13 – Hamiltonian constraint absolute violation profile resulting from the propagation of a gaussian pulse in geodesic slicing ( $H_i = 5H_0$ ).

The scalar pulse separates into two parts. The inward travelling pulse gets reflected at the origin of coordinates and then travels outward. The apparent dynamics is very similar to what we encountered in the study of a gauge pulse. However, the physical situation here is very different as we are now dealing with a non-null distribution of energy. The situation here can be seen as the evolution of a spherical shell initially placed at a radius  $r_i$ . After the shell has bounced from the origin, the central value of the field returns to its homogeneous asymptotical value leaving no apparent effect on the local expansion. The violation of the Hamiltonian constraint profile is shown on Fig. 4.13 for the evolution in the geodesic slicing gauge and for 3 values of the resolution. A similar plot is shown for the result of the evolution in the Bona-Masso slicing with  $f = 0.333$  on Fig. 4.14. In both gauge, the convergence of the method is beyond second-order.

We now study the case where the initial expansion factor is  $H_i = 20H_0$ , that is one order of magnitude larger than the Hubble factor today. The evolution of the scale factor and the homogeneous asymptotical value of the scalar field are shown on Fig. 4.15. The milder expansion between the two de Sitter phases happens earlier. As opposed to the previous case, the dominant part of the initial energy density is proportional to  $\Psi$  which in fact leads to a value of the density smaller than its asymptotical value around the initial pulse. Figure 4.16

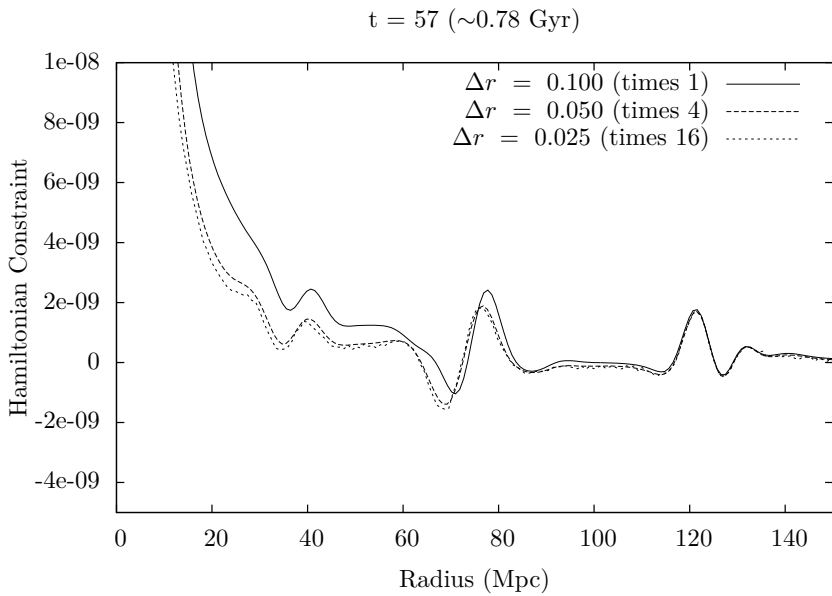


Figure 4.14 – Hamiltonian constraint absolute violation profile resulting from the propagation of a gaussian pulse in Bona-Masso slicing ( $H_i = 5H_0$ ).

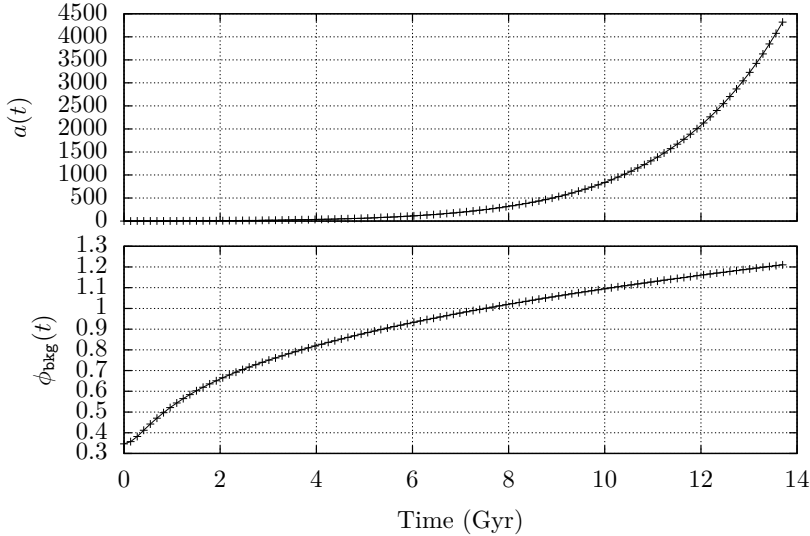


Figure 4.15 – Long-term cosmological evolution of the scale factor and background scalar field for a Universe filled with quintessence ( $H_i = 20H_0$ ).

shows the evolution of the pulse on the spatial domain. The central value of the field does not return to its asymptotical value after the pulse is reflected.

Our interpretation for this is that when the field has a larger value at the centre due to the passing of the pulse, this decreases the energy density of quintessence leading to a temporarily reduced expansion rate.

The Hamiltonian violation profile is shown on Fig. 4.17. The convergence is again above second-order.

The fact that the central value of the field is different to the asymptotical value at late time as an impact on the local expansion around the centre of coordinates. This can be seen from Fig. 4.18 which shows the difference between the background and central values of the scale factor  $a(t) - a(t)\psi^2(t, r = 0)$ . The time of the passage of the scalar pulse at the centre of coordinates is clearly identified from the picture. After that time, the local scale factor decreases monotonically compared to the asymptotical scale factor.

More insight can be brought regarding this matter by considering Fig. 4.19 showing the profile of the trace of the extrinsic curvature tensor. A larger value corresponds to a smaller expansion of space-time. The expansion is initially homogeneous then is inversely proportional to the value of the field when the pulse hits the centre of coordinates, the expansion is thus smaller than that of the background for a short period. This causes the expansion at the centre

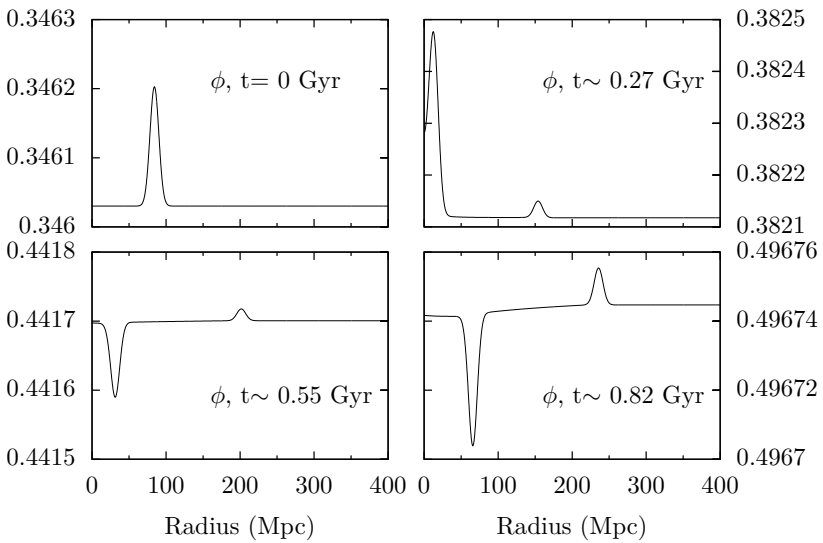


Figure 4.16 – Evolution of a Gaussian quintessence scalar pulse profile on a de Sitter background ( $H_i = 20H_0$ ).

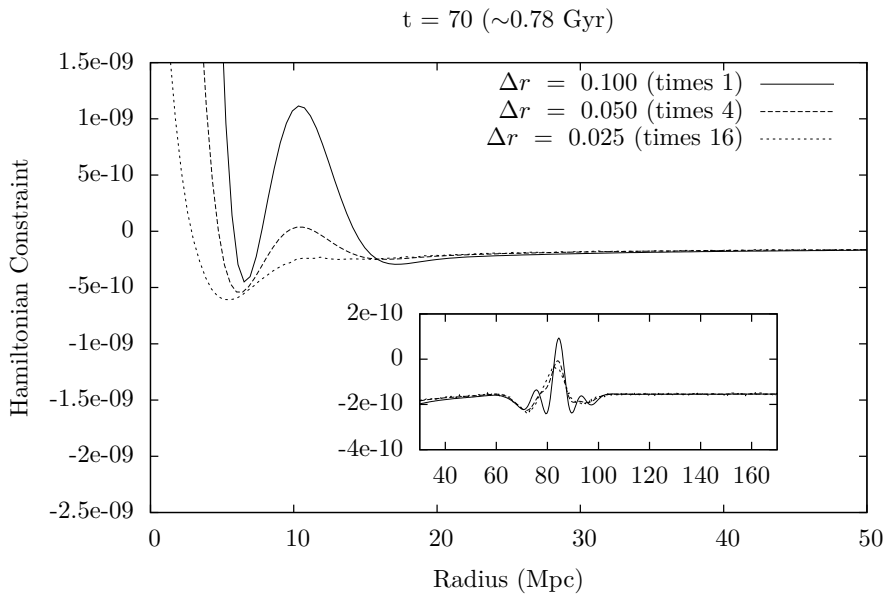


Figure 4.17 – Hamiltonian constraint violation profile resulting from the propagation of a gaussian pulse in geodesic slicing ( $H_i = 20H_0$ ).

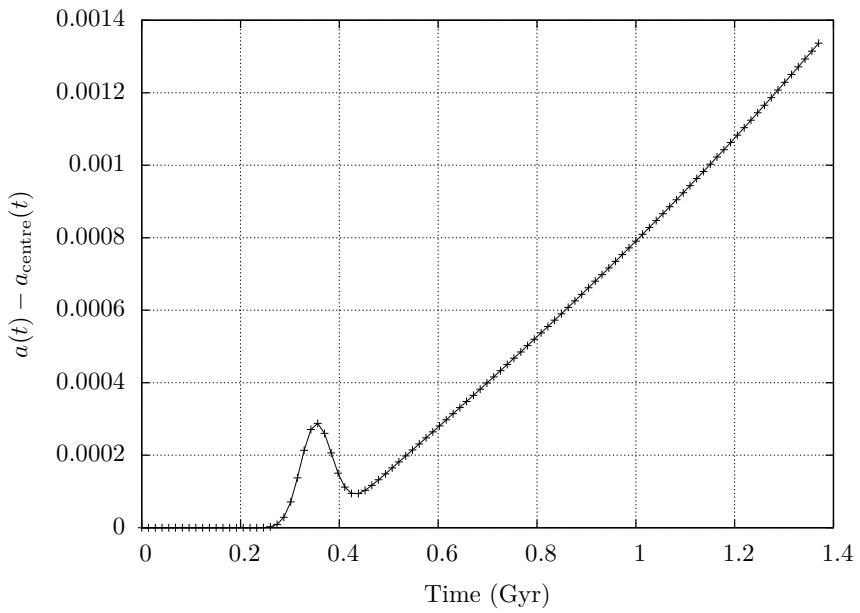


Figure 4.18 – Difference between the background and local expansion factors as a result of the passage of a scalar pulse ( $H_i = 20H_0$ ).

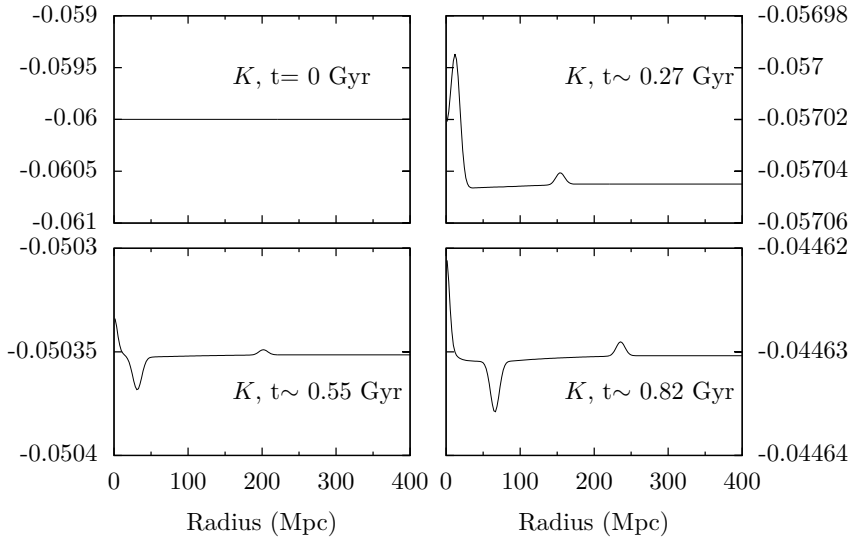


Figure 4.19 – Trace of the extrinsic curvature resulting from the propagation of a gaussian pulse in geodesic slicing ( $H_i = 20H_0$ ).

of the coordinates to fall back behind that of the background. An effect that remains visible after the pulse has been reflected.

## 4.3 Spherical collapse of matter overdensities with quintessence

We now want to investigate the process of formation of large scale structure in a Universe with quintessence dark energy present. This study is performed in two steps. We start by comparing the fully relativistic solution to the top-hat solution then we explore the features of the relativistic solution that are not present within the top-hat model.

### 4.3.1 Background evolution

We consider three different cosmological background models. The first is the simple  $\Lambda$ CDM, the other two are quintessence models with different properties. One is the above-mentioned Ratra-Peebles model, the other is the so-called *Pseudo-Nambu-Goldstone Boson* model (PNGB). While the former is an example of *freezing* model where the violation of the weak energy condition hap-

pens at late time, the latter is classified within the set of *thawing* models with this violation happening at early times (Amendola and Tsujikawa 2010). The analytical expression of the PNGB potential is (Frieman, Hill, Stebbins and Waga 1995)

$$V(\phi) = \mu^4 \cos(1 + \phi/f) . \quad (4.149)$$

The scale factor evolution in these three cosmological models are shown in the left column plots of Fig. 4.20. The middle column shows the rescaling of the matter and quintessence energy densities in natural units in which  $H_0 = 10^{-3}$ . The last column shows the evolution of the equation of state parameter defined, for a perfect fluid as

$$w := \frac{p}{\rho} . \quad (4.150)$$

The density and pressure associated to a scalar field in an homogeneous Universe is read from Eq. (2.41). When the equation of state parameter of the energy component that dominates the overall energy content of the Universe satisfies  $w < -1/3$ , the weak energy condition is violated and the expansion is accelerated. The equation of state associated to a cosmological constant is  $w_\Lambda = -1$ . It varies in time for quintessence models ( $w_\phi \neq cst$ ).

The numerical value of the parameters of each background model are chosen in order for the cosmological evolution to be *qualitatively* close to our own Universe yet in order to deviate sufficiently from one another.

The value of the scale factor is set to one at the beginning of the integration. The time of zero redshift is defined as the time at which the Hubble factor has the observed present day value ( $H = H_0$ ). The redshift corresponding to the epoch of scale factor value  $a$  is then

$$z = \frac{a|_{H=H_0}}{a} - 1 \quad (4.151)$$

This is different to the usual convention which sets today's value of the scale factor to unity. The regions of negative redshift corresponding events in the future are shaded on Fig. 4.20 and subsequent figures. The intermediate dashed line corresponds to the moment of zero redshift (today). These models are qualitatively realistic as they do reproduce an expansion era dominated by dust followed by a vacuum dominated accelerated expansion era.

The cosmological parameters for each background model are given in Table 4.1.

The initial value of the background scalar field is fixed by imposing the initial values of  $\Omega_\phi$  and  $w_\phi$  and imposing that the spatial part of the background Universe is flat so that

$$\rho_\phi^i = \Omega_\phi^i \frac{3H_i^2}{8\pi} . \quad (4.152)$$

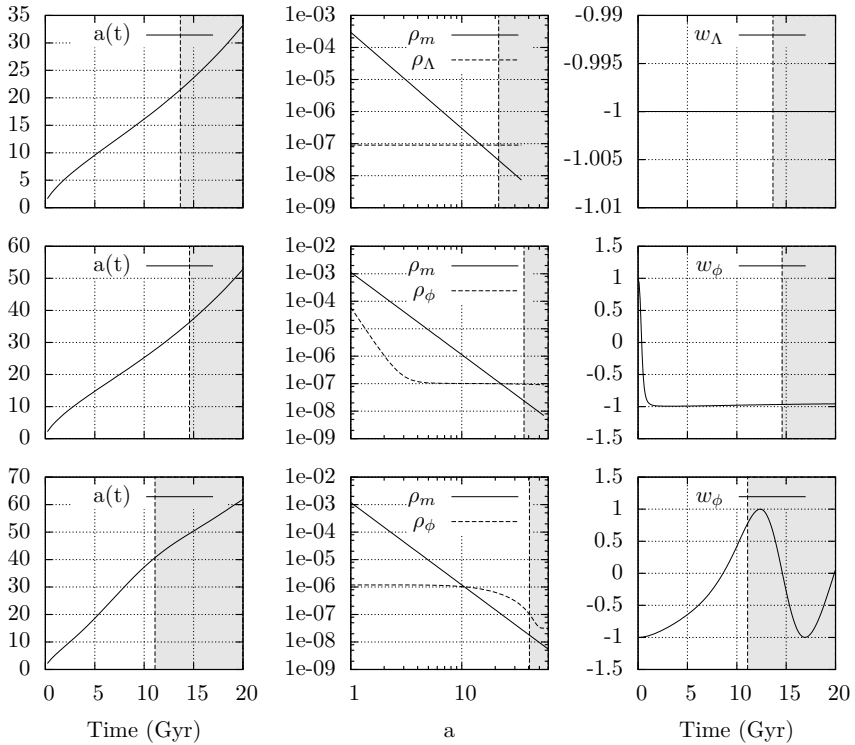


Figure 4.20 – Evolution of the three background models considered for the study of spherical collapse in presence of quintessence.

<i>Model</i>	$\Omega_m^i$	$\Omega_\Lambda^i$	$\Omega_\phi^i$	$H_i$	$w_{\Lambda/\phi}^i$	$\Omega_m^0$	$\Omega_\Lambda^0$	$\Omega_\phi^0$	$w_{\Lambda/\phi}^0$
$\Lambda$ CDM	0.9997	$1 - \Omega_m^i$	0	$50H_0$	-1	0.25	0.75	0	-1
RP	0.9999	0	$1 - \Omega_m^i$	$100H_0$	0.996	0.34	0	0.66	-0.9
PNGB	0.999	0	$1 - \Omega_m^i$	$100H_0$	-1	0.15	0	0.85	0.78

Table 4.1 – Cosmological parameters employed to produce the simulations of Fig. 4.20. Quantities labelled with an “i” correspond to initial values, quantities labelled with an “o” correspond to the values that they have today.

The values of the potential parameters for the RP model are

$$\begin{aligned} n &= 2, \\ M &= \frac{1}{2} \left( \frac{3H_0^2}{8\pi} \right)^{1/(4+n)} (8\pi)^{\frac{n}{8+n}}. \end{aligned} \quad (4.153)$$

The parameters of the PNGB model are

$$\begin{aligned} f &= 15\pi/\sqrt{8\pi}, \\ \mu &= 6 \left( \frac{3H_0^2}{8\pi} \right)^{1/4}. \end{aligned} \quad (4.154)$$

These are chosen in order to produce acceleration at a time close to the present day (Amendola and Tsujikawa 2010).

Before going to the comparison of the relativistic solution with the top-hat, we ought to give some precisions regarding the use of this model in the study of the collapse with quintessence.

### 4.3.2 The top-hat model with a scalar field

One should remain cautious when mentioning the top-hat model in presence of quintessence as this raises some issues.

As we have seen in a previous section, the top-hat model can only be somewhat justified under some very special hypotheses. In particular, the anisotropies linked to a general scalar field should prevent its strictest use altogether. There is however one argument regarding the quintessence field based on the theory of cosmological perturbations which has led some to reconsider it in a modified form.

From cosmological perturbations theory, a scalar field perturbation of scale  $k$  grows following a perturbed Klein-Gordon equation (Hwang and Noh 2001),

$$\delta\ddot{\phi} + 3H\delta\dot{\phi} + (k^2/a^2 + V_{,\phi\phi})\delta\phi = \dot{\phi}\delta_m. \quad (4.155)$$

Where  $V_{,\phi\phi} := \frac{d^2V}{d\phi^2}$ . This equation has the shape of a damped wave equation with effective wavelength roughly given by

$$\lambda_J \sim 1/\sqrt{V_{,\phi\phi}}. \quad (4.156)$$

This is referred to as the *Jeans length* of the scalar field and typically comes out as very large for most quintessence models, usually being of the same order as the cosmic horizon. This would tend to prove that the fluctuations in the scalar field should be unimportant on scales smaller than the horizon. This has led many researchers to assume that the quintessence field should be evenly spread over the Universe and remain rather unaffected by the formation of large scales structures.

In order to account for this, the equation for the evolution of the energy density associated to the scalar field is often cast into the form of Eq. (4.4) which reduces to

$$\ddot{\phi}_{1\text{oc}} + 3\frac{\dot{R}}{R}\dot{\phi}_{1\text{oc}} + \frac{dV}{d\phi} = \Gamma/\dot{\phi}_{1\text{oc}}, \quad (4.157)$$

where  $\phi_{1\text{oc}}$  stands for the local value of the field within the over-dense region. To prevent the field from collapsing, the phenomenological functional parameter  $\Gamma$  is set equal to (Mota and van de Bruck 2004)

$$\Gamma = -3\left(\frac{\dot{a}}{a} - \frac{\dot{R}}{R}\right)\dot{\phi}_{1\text{oc}}^2. \quad (4.158)$$

This makes the equation for the field inside the over-dense region strictly equivalent to that for the outside region thus ensuring  $\phi = \phi_{1\text{oc}}$ . In practice, this amounts to demand that the field within the region couples to the value taken by the expansion factor outside the region rather than the local  $\frac{\dot{R}}{R}$ . While the fact that the field should remain homogeneous is given tentative physical motivations, this last fact seems unnatural.

In the following subsection, we compare the fully relativistic solution with two different top-hat models respectively corresponding to the cases where the quintessence field is coupled to its direct surrounding and is thus allowed to cluster (simply referred to as “top-hat”) and when it is instead coupled solely to the background expansion (referred to as “top-hat n.c” for “no-clustering”).

### 4.3.3 Comparison with the top-hat

The comparison between the fully relativistic solution obtained by solving the complete set of BSSN equations and the top-hat solution is first studied by looking at the central value of the local scale factor defined as  $a\psi^2(t, r = 0)$  in the BSSN coordinates. The quintessence field is assumed to be homogeneous at initial time. The only departure from the homogeneous background comes from the matter energy density. We write the initial matter density contrast as a step-like function in order to be close to the distribution of matter in the top-hat model.

$$\delta_m(t = 0, r) = \delta_m^0 \left( \frac{1}{2} - \frac{1}{2} \tanh(k(r - r_{\text{span}})) \right), \quad (4.159)$$

where  $\delta_m^0$  is the value of the contrast at the centre of coordinates and  $r_{\text{span}}$  is the radius at which the contrast drops to half of its maximum value. The parameter  $k$  adjusts the steepness of the profile. Other profiles were also considered leading to similar results.

The evolution of the background and central values of the scale factor for the  $\Lambda$ CDM model are shown on Fig. 4.21 along with the density contrast at the centre of coordinates. The initial value of the latter being fixed to  $\delta_m^i(r =$

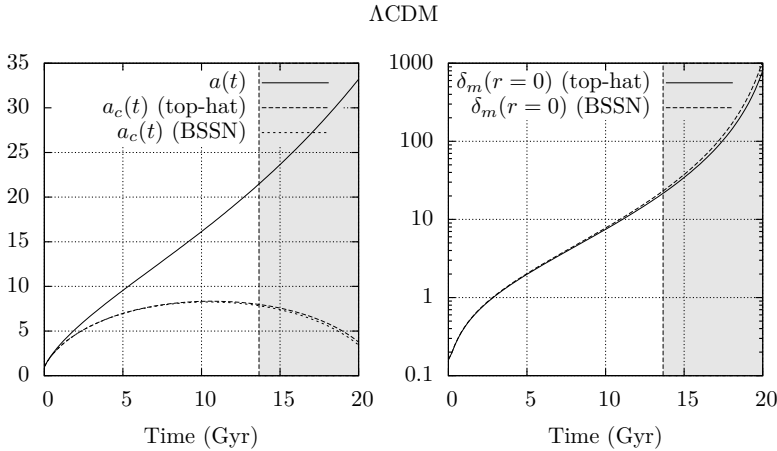


Figure 4.21 – Evolution of the scale factor and the density contrast for the fully relativistic solution and the top-hat solution in the  $\Lambda$ CDM model.

$0) = 0.16$ . It is striking to see how, in spite of all the theoretical limitations of the top-hat model, this reproduces the correct relativistic predictions quite remarkably as far as the scale factor and contrast density are concerned. The correspondance is close to being exact up to very deep within the non-linear growth regime of  $\delta_m$ . The same quantities are shown on Fig. 4.22 for the Ratra-Peebles model with an initial density contrast  $\delta_m^i = 0.12$ . Surprisingly, the solution is again very close to the top-hat solution, regardless of whether the quintessence is allowed to cluster or not, and it looks as if the collapse proceeds in a way very similar to the  $\Lambda$ CDM case. The situation is however very different in the PNGB model as can be seen on Fig. 4.23 obtained with  $\delta_m^i = 0.15$ . The collapse happens too quickly in the top-hat model where the quintessence can cluster. The time when the solutions start to differ lies around  $a \sim 10 - 20$ . Looking back at the evolution of the energy densities, one sees that this corresponds to the time where the quintessence starts to dominate over the dust energy density. The top-hat model with non-clustering quintessence agrees quite well with the general relativistic solution up to very late-times.

Our hypothesis is that the observed significant departure from the top-hat predictions with clustering quintessence is to be expected whenever the quintessence energy density differs from that of a cosmological constant at times when it dominates over the total energy density.

In order to test this hypothesis, we have computed the same quantities in the case of a RP model with different potential parameters leading to a non-constant background energy density throughout all of the integration. The

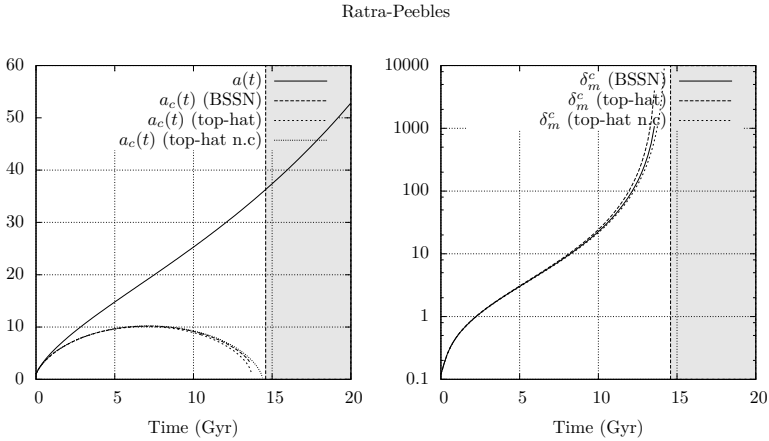


Figure 4.22 – Evolution of the scale factor and the density contrast for the fully relativistic solution and the top-hat solution in the Ratra-Peebles model.

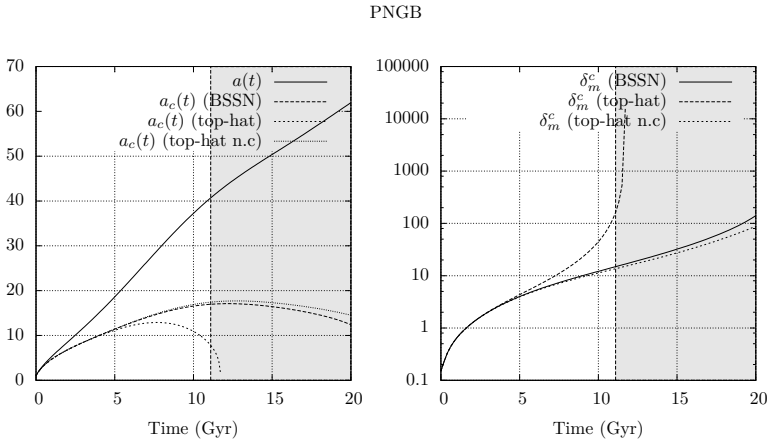


Figure 4.23 – Evolution of the scale factor and the density contrast for the fully relativistic solution and the top-hat solution in the PNGB model.

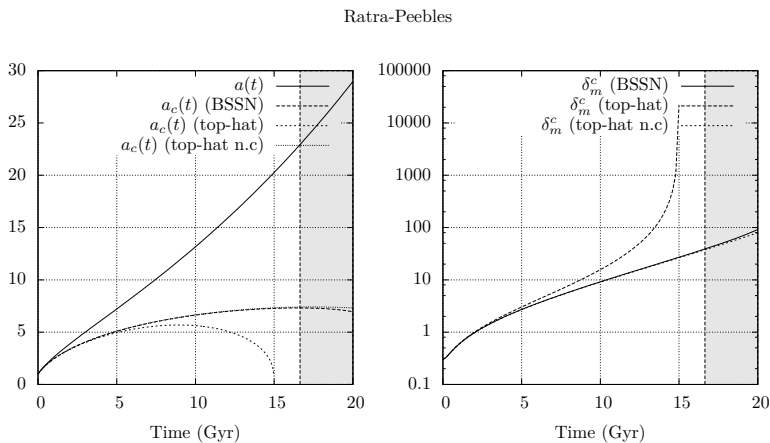


Figure 4.24 – Evolution of the scale factor and the density contrast for the fully relativistic solution and the top-hat solution in the Ratra-Peebles model with parameters leading to a non-constant quintessence energy density at late-time.

cosmological parameters are  $H_i = 30H_0$ ,  $\Omega_m^i = 0.9$ ,  $\Omega_\phi^i = 1 - \Omega_m^i$ ,  $\Omega_\Lambda^i = 0$  and  $w_\phi^i = 0.8$ . The initial density contrast is  $\delta_m^i = 0.3$ . The potential parameter  $M$  is changed to

$$M = \frac{2}{5} \left( \frac{3H_0^2}{8\pi} \right)^{1/(4+n)} (8\pi)^{\frac{n}{8+n}}. \quad (4.160)$$

The result is shown on Fig. 4.24. The evolutions of the background densities are shown on Fig. 4.25. Similarly to the PNGB case, the collapse happens too quickly in the simple top-hat model. The predictions of the top-hat model with non-clustering quintessence agrees even better to the complete solution than before.

So far, we have purposely neglected to discuss the size of the fluctuations used in the above simulations. This is usually what is done in the top-hat approach as the only requirement is for the scale of the homogeneous background to be much larger than the scale of the fluctuation. However, the top-hat model also advocates that the interior region should be sufficiently homogeneous to apply the Friedmann equations. In order to meet both these requirements, we have used  $r_{\text{span}} \sim 20\text{Mpc}$  as the size of the fluctuation. This choice makes even more sense in view of the result of this section.

The scale of 20Mpc corresponds to the size of large clusters of galaxies which formed at late-time in the History of the Universe but, as we have seen, late-time is also when the effects of quintessence become important. The study of the effect of the initial size of the fluctuation would be an interesting task that we choose to postpone for now.

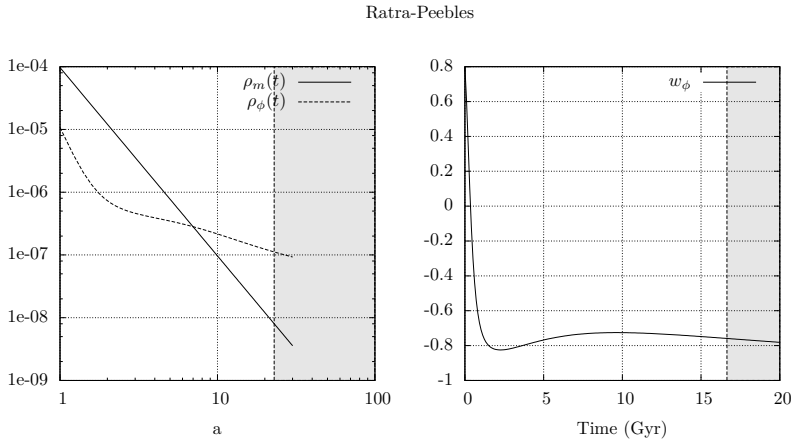


Figure 4.25 – Evolution of the background energy densities and quintessence equation of state parameter in a Ratra-Peebles Universe with non-constant quintessence energy density at late-time.

The framework that we have developed for the study of the collapse allows us to verify the assumption that the scalar field should not cluster on scales much smaller than the Horizon. The quintessence density contrast is defined as

$$\delta_\phi := \left( \frac{E_\phi}{\rho_{\text{bkg}}^\phi} - 1 \right). \tag{4.161}$$

The central value of this quantity is shown for the top-hat model with clustering of quintessence and for the BSSN simulation on Fig. 4.26 for the 3 quintessence models explored so far. The top row corresponds to PNGB, the second and third rows correspond to a Ratra-Peebles model where the field is respectively frozen and not-frozen at late-time. No ad hoc assumption is made regarding the Jeans wavelength of the scalar field. The contrast energy density does evolve in time yet only very weakly contrarily to what is expected from the simple top-hat model. The fact that the contrast energy density remains very small explains the remarkable agreement between the BSSN solution and the top-hat model without clustering of quintessence. The larger growth in the PNGB model probably explains the slightly larger departure observed on Fig. 4.23.

It is quite remarkable that the top-hat model without clustering should reproduce the predictions of the complete solution regarding the local scale factor and evolution of the matter density contrast in spite of its simplicity. However, the  $\Gamma$  term that allows this equivalence to happen is phenomenological and lacks to provide a sensible physical understanding of the local effects that prevent the field to build up energy within the over-dense region. This is what

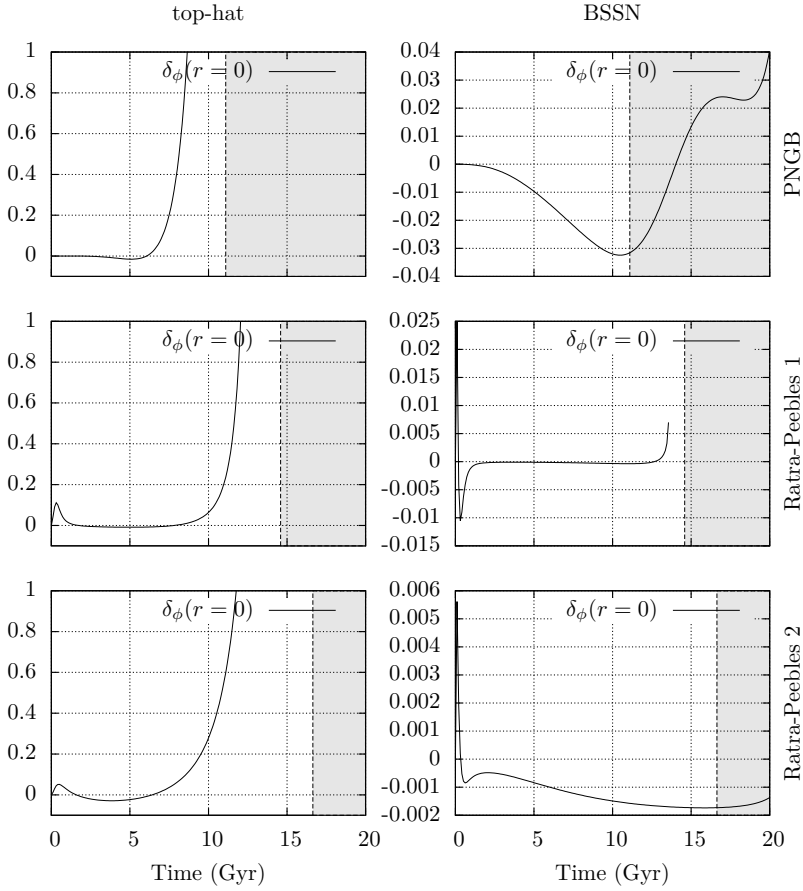


Figure 4.26 – Evolution of the central value of the quintessence energy density during the collapse for 3 models of quintessence.

we intend to provide in the next section.

### 4.3.4 Beyond the top-hat model

The method that we have developed allows to explore the physical reasons behind the fact that quintessence clusters very little. The top-hat model, regardless of whether it allows quintessence to cluster, assumes that the over-dense region has the symmetries of the FLRW space-time. This forbids, in particular, the existence of anisotropic pressures and momentum transfers. While this is not a problem when only dust matter is present, this is rather arbitrary in presence of quintessence. In the latter case, anisotropic pressure terms do build up values that are comparable to the inhomogeneous part of their isotropic counterparts. The isotropic pressure terms are themselves kept very small however for other reasons.

In this section, we investigate the evolution of anisotropies during the collapse process for the PNGB model and the Ratra-Peebles model with a non-constant energy density at late-time as we reckon that these are the most interesting ones when the study of the effect of quintessence on the collapse is concerned.

Spherical symmetry forbids any anisotropic quantities to point along directions other than the radial one. The momentum transfer associated to a scalar field is given by Eq. (4.136). It is useful to think of the scalar field as a non-perfect fluid in order to identify the radial anisotropic pressure term as

$$\pi_\phi := \pi_{rr}^\phi = (S_a^\phi - S_b^\phi). \quad (4.162)$$

This comes out as  $\pi_\phi = \frac{\Psi^2}{\psi^4 a^2 \dot{a}}$ . It is zero in the background space-time, as it should be.

In order to understand why the field does not cluster, it is best to consider why it should collapse in the naive top-hat model in the first place. As it turns out, most of the difference in the energy density of the field comes from a difference in kinetic energy. Fig. 4.27 shows the evolution of the field inside and outside of the over-dense region in the naive top-hat for both the RP and PNGB models. In both case, the field starts by growing very quickly building up kinetic energy. This causes the equation of state parameter to raise quickly as shown on Fig. 4.28. At this point, the impact of the field on the collapse is still limited as dust matter remains the dominant component of the energy density. The increase in the kinetic energy is reinforced at the turnover when the over-dense region stops expanding and starts to collapse. The kinetic energy of the field is proportional to the square of its momentum  $\Pi$ , the dynamics of which is given by Eq. (4.137) which, in the spatially homogeneous case and setting  $\alpha = 1$ , reduces to

$$\partial_t \Pi = K \Pi - \frac{dV}{d\phi}. \quad (4.163)$$

A collapsing space corresponds to  $K > 0$ . Leading to a positive feedback on

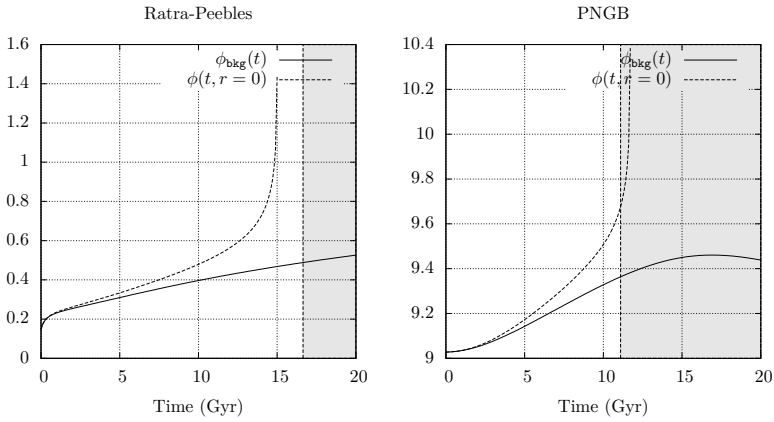


Figure 4.27 – Evolution of the central and background values of the field in the Ratra-Peebles and PNGB models in the naive top-hat picture in which quintessence fully clusters.

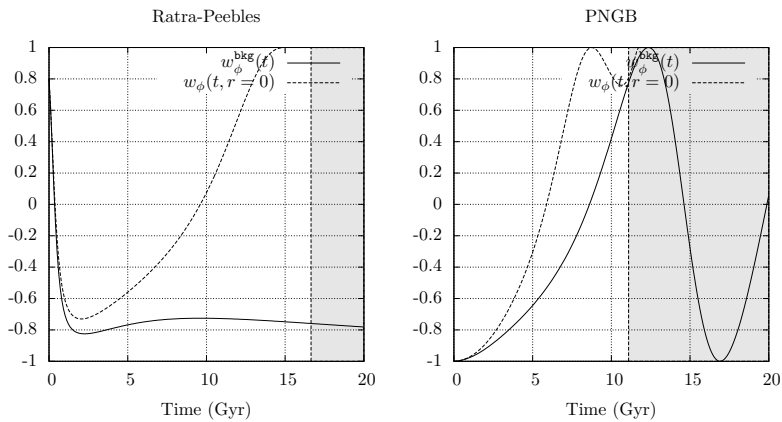


Figure 4.28 – Evolution of the central and background values of the equation of state parameter in the Ratra-Peebles and PNGB models in the naive top-hat picture in which quintessence fully clusters.

the growth of  $\Pi$  which can hardly be counterbalanced by the gradient of the potential, especially when the latter is very flat.

The amount of field kinetic energy built up within the over-dense region causes the equation of state parameter to retain a high value. The field energy inside the region thus has a positive pressure that adds up to the amount of dust energy density to facilitate the collapse.

The faulty part of this picture lies in the fact that the two regions of space-time are completely disjointed and there is no possibility of momentum transfer between both regions. This transfer is made possible in the complete picture through the second term of Eq. (4.137). The modified top-hat model with no clustering reproduces this coupling artificially through the  $\Gamma$  term of Eq. (4.157). This induces a loss of momentum proportional to the difference between the extrinsic curvatures of the inner and outer regions of space that effectively compensates the positive feedback effect described above. This term is purely phenomenological but is also non-local.

The method that we have developed to solve for the complete relativistic dynamics allows to investigate what is actually going on at the local scale.

The upper rows of Fig. 4.29 and Fig. 4.30 show the evolution of the field density contrast profile as a function of time along with the radial momentum transfer from the stress-energy tensor  $j_r^\phi$  respectively for the Ratra-Peebles and the PNGB models. These figures were obtained with the same parameters as in the previous section. The results are presented in natural units with the Hubble constant value set to  $H_0 = 0.001$ . As the over-dense region gets closer to the turn-over, the momentum transfer raises to a large positive value which corresponds to an outward transfer. This is responsible for balancing the kinetic energy inside and outside of the over-dense region. This transfer is maximal around the boundary of the over-dense region which is the place where the gradients of the scalar field and metric variables are maximal.

The decrease in the momentum of the field adjusts the equation of state parameter at the centre of coordinates to its background value. As the Universe draws more into the vacuum dominated era, this may either result in a more rapid or delayed collapse depending on the shape of the potential. The PNGB model displays a positive equation of state parameter at late-time resulting in a facilitated collapse which in turns increases the small value of the quintessence density contrast. In both models, this small yet non-zero density contrast induces a small difference of pressure inside the over-dense region. The bottom rows of Fig. 4.29 and Fig. 4.30 show the evolutions of the gradient of isotropic pressure between the over-dense and background regions (left pannel) and the anisotropic pressure profile (right pannel). One sees that the isotropic pressure dominates over the anisotropic pressure. The latter is of the order of less than 10 times smaller than the former around the boundary of the over-dense region where it is maximal.

For completeness, we ought to provide an explanation for the values in the plots of Fig. 4.29 at early time. These are a consequence of the transient behaviour following the evolution of the particular set of chosen initial conditions.

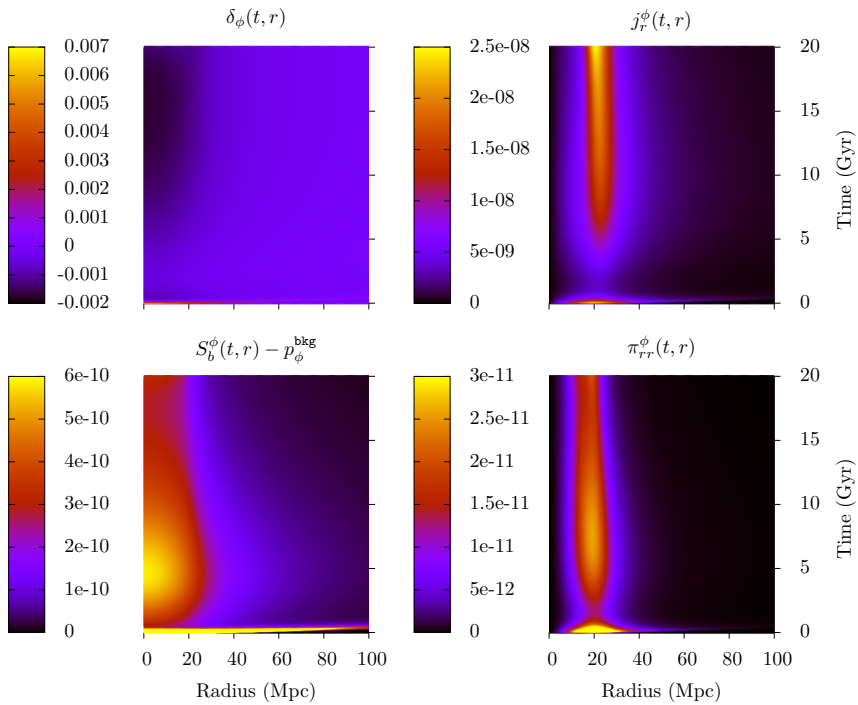


Figure 4.29 – Evolution of the anisotropies in the Ratra-Peebles model in natural units with  $H_0 = 0.001$ .

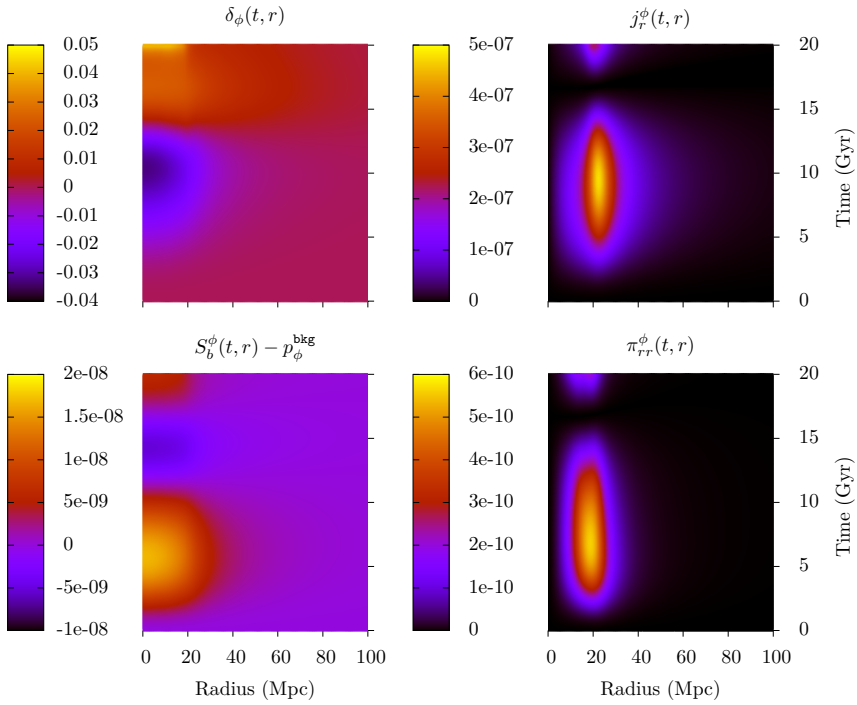


Figure 4.30 – Evolution of the anisotropies in the PNGB model in natural units with  $H_0 = 0.001$ .

At initial time, the field starts off in a very steep region of its potential, this results in a large gain of momentum at the centre of coordinates which is not yet counterbalanced by the negative feedback of expansion nor the momentum transfer that is initially null. The small increase in  $\delta_\phi$  that results, along with a positive equation of state  $w_\phi \sim 1$  leads to a temporary high pressure difference that overshoots the colour scale of the plot. The effect is rapidly counterbalanced by expansion and momentum transfer. The small initial “jump” in the contrast density is perceivable on the two bottom plots of Fig. 4.26. One sees how the contrast density gets down slower in the top-hat picture with clustering as the only effect is the negative feedback from expansion. These transient behaviours have little effect on the overall evolution as these happen at a time when the matter energy density is dominant. These however encourage us to look for more general initial conditions, a task that we count among the perspectives of the present work.

## 4.4 Conclusion

In this chapter, we have shown how the top-hat collapse model can originate as an approximation of a complex relativistic situation. We have provided our own model for the collapse based on the (3+1) formalism and numerical relativity, the validity of which we have demonstrated in a series of numerical tests among which we have recovered the known LTB solution for the collapse of dust matter.

We have applied our method to the study of the collapse in presence of quintessence and we have performed a comparison with the naive top-hat model in which the quintessence field fully clusters and the one in which it is kept homogeneous at all time. The latter shows the best agreement with the fully relativistic solution and predicts a delayed collapse compared to the naive model. As we have shown, the fast collapse of the naive model is a result of the field building up a lot of kinetic energy within the over-dense region. This is prohibited in the more complete picture as the over-dense region loses momentum to the surrounding background greatly limiting the growth of the field density contrast. This is manually set to zero in the top-hat model without collapse by directly coupling the field inside the over-dense region to the outer extrinsic curvature. We have argued that, even though this seems a relevant approximation, this lacks a sensible physical motivation on the local scale.

The numerical framework that we have built allows to derive the fact that the quintessence field clusters very little. This also provides a way to compute the evolution of the profiles of anisotropic pressures and momentum transfer throughout the process. These are maximal on the boundary of the over-dense region and the latter is responsible for keeping the growth of scalar field inhomogeneities very mild. The anisotropic pressures have a magnitude of the order of the difference of their isotropic counterparts with their background values at the boundary.

We are confident that the methods of numerical relativity still have much to teach us about the cosmological spherical collapse. We discuss the possibilities to elaborate from our work in the closing word of this manuscript.



# Conclusion

We have now reached the end of this manuscript and it is time to conclude on our work. We start by confronting the endeavours that was ours at the beginning of our project and the outcomes reached at the end of it. We then proceed to discuss the perspectives regarding the work performed in the fields of inflation and structures formation.

This thesis had the initial project to study the formation of large scale structures in presence of quintessence and how it depends on the choice of the particular model used for its analysis. In the end, our main focus was put on the particular study of the spherical collapse leading us to build a more elaborate fully relativistic cosmological model than we had expected. Along the way, we seized the opportunity to contribute to the field of inflation cosmology at a time when the announcement of the discovery of the primordial gravitational waves by the BICEP2 experiment caused quite a tumult within the cosmology community. Following these projects and opportunities has allowed us to learn more about many different aspects of cosmology ranging from the analysis of the dynamics behind the equations of General Relativity to the applications of these in many different situations.

In case the tensor to scalar ratio is indeed close to the upper bound set to the joint analysis of BICEP2, Keck Array and Planck data, the hybrid model would remain a valid candidate for inflation. The refined analysis of the parameter space that we have performed has shown how the model can be in excellent agreement with the data from both the Planck and BICEP2 collaborations due to a non-trivial mechanism of violation of the slow-roll conditions.

The principal contribution of the present work is arguably the one made to the study of the formation of large scale structures. We have provided the first fully relativistic treatment of the evolution of the cosmological space-time during the collapse in presence of a quintessence scalar field. This was made possible through the use of Numerical Relativity techniques. Our work is complementary to the work by Torres et al. (Torres et al. 2014) in which the growth of scalar perturbations is studied for a massive quadratic potential.

The top-hat model is usually seen as a functioning tool for the study of large scale structures through N-body simulations which has the merit of having a simple Newtonian interpretation. We showed how this model is conceptually limited from the point of view of General Relativity. Our results have shown

how the knowledge of the behaviour of quintessence is essential to provide accurate predictions on the time of the collapse and the non-linear evolution of the density contrast. We have recovered the result from the theory of cosmological perturbations which predicts that quintessence should not cluster much on scales smaller than the horizon and we have provided a local physical explanation of the phenomena. Our analysis shows how the top-hat model in which the quintessence field is kept homogeneous leads to predictions sufficiently accurate to be used when a fully relativistic computation is not practically possible as far as only the local scale factor and non-linear density contrast are needed. However, it also reveals the importance of quantities that are overlooked in this model such as the momentum transfer through the boundary of the over-dense region outward and the building of anisotropic pressures. Even though this remains very mild, a small clustering of the scalar field can also be observed depending on the shape of the potential and its late-time behaviour.

The use of numerical relativity techniques applied to cosmology is at an early stage of its development. With the research presented in this work, we wish to contribute to initiate a rapprochement between the two fields by demonstrating how the former can shed light on the physical phenomena of the latter. We foresee numerous perspectives to pursue our research.

The initial conditions that we have employed are of practical interest as long as a comparison with the top-hat model is concerned. However, the density profile of a forming cluster does not simply follow a step-like distribution. The choice of setting the initial extrinsic curvature as a constant traceless diagonal tensor is also made for the sake of simplicity. We have had a glimpse of the effects that the initial conditions can have on the overall evolution as we dealt with the collapse in the Ratra-Peebles model of quintessence in which forcing the momentum transfer to zero at initial time leads to transient behaviours that are very likely to be unnatural. One important future task is therefore to generalise the computation of the initial conditions. We have chosen to leave this generalisation for later as we felt it was not primordial to the understanding of the results exposed here.

In most treatments, the top-hat model is assumed to hold up to a time when the density contrast reaches a value above which the spherical object is assumed reaches a dynamical equilibrium between its mean kinetic and potential energies. This is referred to as *virialisation*. The features of the top-hat model do not allow to account for this process as it is only concerned with pressureless matter and makes use of the virialisation argument as a workaround and not as a prediction. We are confident that our method would be a very good starting point for the development of a more complete study of what happens just before the collapse. This would imply to solve the full set of relativistic fluid dynamics equations resulting from the energy and momentum conservation conditions. A task which we already have started to undertake in the making of this work using the well-known Valencia formulation (Ibáñez, Aloy, Font, Martí, Miralles and Pons 2001). We have chosen not to mention the preliminary results obtained following this track in the present work for the sake

of clarity as we judged these are not sufficiently mature. Once the complete dynamics of fluid matter is known, the virialisation process can be studied via appropriate statistical mechanics techniques yet to be added to our framework.

For reasons of simplicity and for the sake of easy comparison with the top-hat model, most of the simulations presented in this work involving a blend of dust matter and quintessence were made in the geodesic slicing gauge which is notoriously bad for the study of collapsing space-times. Changing to another gauge could lead to even better stability of the method for long-term evolutions perhaps even allowing to follow the evolution of space-time beyond the time of collapse. Another gauge choice would imply a more complex dynamics of even simple dust matter which is another very good reason to pursue the work done on the hydrodynamics in our code.

The numerical framework that we have built also has more straightforward possible applications that we wish to investigate in the near future. We want to use it in order to derive geometrical observables in the hope of finding a novel way to discriminate between quintessence models through the observation of the formation of clusters of galaxies. Our analysis has allowed to get a glimpse of the influence of scalar field perturbations on matter and the evolution of the local space-time. This is a most interesting issue and another application of our work. In the foreseeable future, we want to investigate the behaviour of light geodesics passing near the boundary of the over-dense region as this is where the anisotropic pressures and momentum transfer are the largest. We could do so in real-time as the structure collapses using the GYOTO code (Vincent, Paumard, Gourgoulhon and Perrin 2011).

The deviations from homogeneity of the scalar field in the fully relativistic solution are very small in comparison with the inhomogeneities in the matter distribution. Though the effects of these field inhomogeneities might be very limited in “ordinary” General Relativity, these might be more vivid in modified theories in which the field is non-minimally coupled to gravity. These effect could readily be investigated using our method to solve for the space-time dynamics in the Einstein frame in which the equations for the evolution of the metric variables are unaltered and the modifications of the theory of gravity are contained within the potential of the scalar field.

Finally, the code which we have produced might be of certain use for the analysis of the stability of new mathematical solutions of General Relativity to cosmology.



# List of Tables

3.1	Best fit, mean likelihood and $1\sigma$ and $2\sigma$ intervals for hybrid model parameters (in units of reduced Planck mass), for Planck+BAO (upper part) and Planck+BAO+BICEP2 (lower part). A star denotes bounds outside of the prior limits. . . . .	53
4.1	Cosmological parameters employed to produce the simulations of Fig. 4.20. Quantities labelled with an “i” correspond to initial values, quantities labelled with an “o” correspond to the values that they have today. . . . .	99



# List of Figures

1.1	The action of the Lorentz transformation is pictured on a space-time diagramme by a rotation by an imaginary angle with $\tanh \eta = v$ . . . . .	7
1.2	The actual path between two events si the one that maximises the proper time of the moving object. . . . .	8
2.1	Foliation of space-time in the (3+1)-formalism. $\alpha dt$ is the lapse of proper time measured by an Eulerian observer. $\beta^i$ is the shift displacement between this observer and the point of constant spatial coordinates $x^i$ . . . . .	19
3.1	Logarithm of the original two-fields hybrid potential. The almost flat valley lies in the direction $\psi = 0$ . . . . .	43
3.2	Evolution of the first Hubble-flow parameter $\epsilon_1$ as a function of $\phi/\mu$ . The complete solution differs greatly from the slow-roll solution at small values of $\mu$ . . . . .	45
3.3	Evolution of the second Hubble-flow parameter $\epsilon_2$ as a function of $\phi/\mu$ . As in Fig. 3.2 the complete solution differs from the slow-roll approximation for small values of $\mu$ . . . . .	46
3.4	Number of e-folds produced after reaching the maximum of $\epsilon_1$ as a function of $\mu$ . Below the threshold value $\mu_{\text{thr}} \sim 1.6M_{pl}$ , only a few e-folds are realised at small field values in contradiction with slow-roll predictions. . . . .	47
3.5	$\phi_*$ (top) and corresponding $n_s$ (central) and $r$ (bottom) plotted as a function of $\phi_{\text{end}} = \phi_c$ using Eq. (3.70), for $\mu = 1M_{pl}$ (blue), $\mu = 5M_{pl}$ (red), $\mu = 10M_{pl}$ (yellow) and $\mu = 15M_{pl}$ (green), assuming $N_* = 60$ . The horizontal dotted lines in the central and bottom panels represent respectively the $2\sigma$ regions of Planck and BICEP2. The dotted line in the top panel is obtained by using the approximation of Eq. (3.74). . . . .	49
3.6	Contour plot of the spectral index $n_s$ in the plane $(\log_{10} \phi_c, \log_{10} \mu)$ , using the exact background dynamics and assuming $N_* = 60$ . The red dashed contours represent the $2\sigma$ confidence interval for Planck. . . . .	50

3.7	Contour plot of the tensor to scalar ratio $r$ in the plane $(\log_{10} \phi_c, \log_{10} \mu)$ , using the exact background dynamics and assuming $N_* = 60$ . The red dashed contours represent the $2\sigma$ confidence interval for BICEP2. . . . .	51
3.8	Marginalised one-dimensional and two-dimensional posterior probabilities for the hybrid model parameters (in reduced Planck mass units) in the large field regime, for Planck+BICEP2. The red contours are the $1\sigma$ and $2\sigma$ regions of confidence. The black contours are the $1\sigma$ and $2\sigma$ regions for Planck only. In the 1D plots, the black/red solid lines show the marginalised posterior distributions of the parameters respectively for Planck and Planck+BICEP2. The dotted lines represent the mean likelihoods. . . . .	56
3.9	Two-dimensional marginalised posterior probabilities for the hybrid model parameters (in reduced Planck mass units) as well as the derived parameters $n_s$ , $r$ and $\rho_{\text{end}}$ for Planck+BICEP2. The red contours are the $1\sigma$ and $2\sigma$ regions of confidence. The black contours are the $1\sigma$ and $2\sigma$ regions for Planck only. . . .	57
3.10	Distribution of 3000 points within the Markov chains in the plane $(\log_{10} \mu, \log_{10} \phi_c)$ . In the upper panel, the colour scale represents the corresponding spectral index value, in the lower panel it represents the corresponding tensor to scalar ratio. . . . .	58
4.1	Time evolution of the radial profile of the lapse $\alpha$ . . . . .	75
4.2	Evolution of the homogeneous lapse and scale factor $\alpha_{\text{bkg}}(t)$ and $a(t)$ . . . . .	76
4.3	$L^2$ -norm of the Hamiltonian and momentum constraints. . . . .	77
4.4	Radial profile of the absolute violation of the Hamiltonian constraint for 3 values of the spatial resolution. . . . .	78
4.5	Initial conformal factor and asymptotical value at infinity. . . .	80
4.6	Spatial metric functions in the BSSN and LTB variables at early time. The top curves of each plot correspond to $\gamma_{rr}$ , the bottom curves correspond to $\gamma_{\theta\theta}/r^2$ . . . . .	82
4.7	Background and the central scale factors for a Universe full of dust. . . . .	83
4.8	Central value of the density contrast for a Universe full of dust. . . .	84
4.9	Evolution of the density contrast profile for a Universe full of dust. . . .	85
4.10	$L^2$ -norm of the Hamiltonian constraint violation in time following the evolution of a dust matter over-density. . . . .	86
4.11	Long-term cosmological evolution of the scale factor and background scalar field for a Universe filled with quintessence ( $H_i = 5H_0$ ). . . . .	89
4.12	Evolution of a gaussian quintessence scalar pulse profile on a de Sitter background ( $H_i = 5H_0$ ). . . . .	90

4.13	Hamiltonian constraint absolute violation profile resulting from the propagation of a gaussian pulse in geodesic slicing ( $H_i = 5H_0$ ).	91
4.14	Hamiltonian constraint absolute violation profile resulting from the propagation of a gaussian pulse in Bona-Masso slicing ( $H_i = 5H_0$ ).	92
4.15	Long-term cosmological evolution of the scale factor and background scalar field for a Universe filled with quintessence ( $H_i = 20H_0$ ).	93
4.16	Evolution of a gaussian quintessence scalar pulse profile on a de Sitter background ( $H_i = 20H_0$ ).	94
4.17	Hamiltonian constraint violation profile resulting from the propagation of a gaussian pulse in geodesic slicing ( $H_i = 20H_0$ ).	95
4.18	Difference between the background and local expansion factors as a result of the passage of a scalar pulse ( $H_i = 20H_0$ ).	96
4.19	Trace of the extrinsic curvature resulting from the propagation of a gaussian pulse in geodesic slicing ( $H_i = 20H_0$ ).	97
4.20	Evolution of the three background models considered for the study of spherical collapse in presence of quintessence.	99
4.21	Evolution of the scale factor and the density contrast for the fully relativistic solution and the top-hat solution in the $\Lambda$ CDM model.	102
4.22	Evolution of the scale factor and the density contrast for the fully relativistic solution and the top-hat solution in the Ratra-Peebles model.	103
4.23	Evolution of the scale factor and the density contrast for the fully relativistic solution and the top-hat solution in the PNGB model.	103
4.24	Evolution of the scale factor and the density contrast for the fully relativistic solution and the top-hat solution in the Ratra-Peebles model with parameters leading to a non-constant quintessence energy density at late-time.	104
4.25	Evolution of the background energy densities and quintessence equation of state parameter in a Ratra-Peebles Universe with non-constant quintessence energy density at late-time.	105
4.26	Evolution of the central value of the quintessence energy density during the collapse for 3 models of quintessence.	106
4.27	Evolution of the central and background values of the field in the Ratra-Peebles and PNGB models in the naive top-hat picture in which quintessence fully clusters.	108
4.28	Evolution of the central and background values of the equation of state parameter in the Ratra-Peebles and PNGB models in the naive top-hat picture in which quintessence fully clusters.	108
4.29	Evolution of the anisotropies in the Ratra-Peebles model in natural units with $H_0 = 0.001$ .	110

4.30	Evolution of the anisotropies in the PNGB model in natural units with $H_0 = 0.001$ . . . . .	111
C.1	A heuristic representation of FORTCosmoSS . . . . .	133
C.2	Tree of dependencies of the FORTCosmoSS project . . . . .	142

# Appendix



# Appendix A

## Natural units

Many physical quantities are expressed solely in terms of units of length, mass and time.

In inflationary cosmology, Newton's constant  $G$ , Planck's constant  $\hbar$  and the speed of light  $c$  are often encountered. The natural Planck scales can be derived by appropriate combinations of these constants.

$$m_{\text{pl}} = \sqrt{\frac{\hbar c}{G}}, \quad l_{\text{pl}} = \sqrt{\frac{G\hbar}{c^3}}, \quad t_{\text{pl}} = \sqrt{\frac{G\hbar}{c^5}}. \quad (\text{A.1})$$

One can then work in units in which these scales are all equal to one. The result of any computation can be converted back to its value in the international system of units by inspection of its dimensions and subsequent multiplication by appropriate powers of the above scales values in the international system of units.

Other choices of units are also possible. In theoretical astrophysics, it is useful to set the scales

$$m_s = M_{\odot}, \quad l_s = \frac{GM_{\odot}}{c^2}, \quad t_s = \frac{GM_{\odot}}{c^3}, \quad (\text{A.2})$$

equal to one.  $M_{\odot}$  is the solar mass. The numerical value of the length scale in meters is then  $l_s \sim 1.5 \times 10^3 m$ . This is equal to half the Schwarzschild radius of the sun.



## Appendix B

# Operator Splitting for PIRK

The use of the PIRK method described in chapter 4 requires to write the system of dynamical equations in the form of Eq. (4.77). We have applied this method to the coupled set of BSSN space-time, matter and quintessence scalar field.

In the first step, the matter variables are evolved along with  $\hat{a}, \hat{b}, \psi, \alpha$  and the scalar field functions  $\phi$  and  $\Psi$ . These are all included with in the  $L_1$  operator. In the second step, the extrinsic curvature components  $K$  and  $A_a$  are evolved along with the scalar field function  $\Pi$  using the updated values form step 1. The  $L_2$  and  $L_3$  operators are :

$$L_{2(A_a)} = - \left( \nabla^r \nabla_r \alpha - \frac{1}{3} \nabla^2 \alpha \right) + \alpha \left( R_r^r - \frac{1}{3} R \right) \quad (1) \quad (B.1)$$

$$L_{3(A_a)} = \alpha K A_a - 16\pi\alpha(S_a - S_b) \quad (B.2)$$

$$L_{2(K)} = -\nabla^2 \alpha \quad (B.3)$$

$$L_{3(K)} = \alpha(A_a^2 + 2A_b^2 + \frac{1}{3}K^2) + 4\pi\alpha(E + S_a + 2S_b) \quad (B.4)$$

$$L_{2(\Pi)} = \frac{\alpha}{a^2\psi^4\hat{a}}\Psi \left( \frac{2}{r} - \frac{\partial_r \hat{a}}{\hat{a}} + \frac{\partial_r \alpha}{\alpha} + 2\frac{\partial_r \psi}{\psi} \right) \quad (B.5)$$

$$L_{3(\Pi)} = \alpha K \Pi + \frac{\alpha}{a^2\psi^4\hat{a}}\partial_r \Psi - \alpha \frac{dV}{d\phi} \quad (B.6)$$

---

<sup>(1)</sup>The expression of  $R_r^r$  and  $R$  both involve terms proportional to  $\hat{\Delta}^r$  and  $\partial_r \hat{\Delta}^r$ . These are in fact included in the corresponding  $L_3(A_a)$  operator. The above notation is a short-hand.

Finally,  $\hat{\Delta}^r$  is evolved partially implicitly using:

$$L_{2(\hat{\Delta}^r)} = -\frac{2}{a}(A_a \partial_r \alpha + \alpha \partial_r A_a) - \frac{4\alpha}{r\hat{b}}(A_a - A_b) \\ + \frac{\xi\alpha}{a} \left[ \partial_r A_a - \frac{2}{3} \partial_r K + 6A_a \partial_r \chi + (A_a - A_b) \left( \frac{2}{r} + \frac{\partial_r \hat{b}}{\hat{b}} \right) \right], \quad (\text{B.7})$$

$$L_{3(\hat{\Delta}^r)} = 2\alpha A_a \hat{\Delta}^r - 8\pi j_r \frac{\xi\alpha}{\hat{a}}. \quad (\text{B.8})$$

The generalised above expression to the case of  $\beta_\mu \neq 0$  is given in (Montero and Cordero-Carrión 2012).

# Appendix C

## The code

### C.1 Introduction

In this section, we give some details regarding the code used in the present work. This has been released as an open-source participative project and is available at

```
http://github.com/jrekier/FORTCosmoSS
```

### C.2 Downloading and compiling

The source code can be directly downloaded in a compressed format from the project's main page. It can also be retrieved using git and the command

```
git clone http://github.com/jrekier/FORTCosmoSS
```

Building from source requires the GNU Fortran compiler which is part of the GNU Compiler Collection (GCC). The code is built simply by issuing the command

```
make(1) .
```

### C.3 First run

The code is simply run via

```
./main
```

---

<sup>(1)</sup>any subsequent compilation following a change in the source file `./src/grid.f90` should be done by using instead `make clean all`.

The default input parameters corresponds to the spherical collapse of a matter profile in presence of quintessence subjected to a Ratra-Peebles potential (see Sect.4.3.3). These can be changed in files `./input.ini` and `./Ratra_Peebles.ini`. These files are abundantly commented and can be easily understood.

Upon start-up, the code produces the following screen output

```
#####
" Spherically Symmetric BSSN code by Jeremy Requier "
" - contact: jrequier@gmail.com "
#####

Initialising...
-----
Staggered Grid layout :

    -0.0250  0.  0.0250    0.0750    0.1250
... --x----|----x-----x-----x--- ...
                < dx=0.05 >

Output list:
-----
profiles          cosmo. var.
--> x              --> t
--> x_Mpc          --> t_sync
--> Del_H          --> a
--> phi           --> a_centre
--> del_m         --> H
                  --> phi_hom
                  --> delta_m_c
                  --> delta_phi_c

Background is Friedmann,
initial scale factor ai = 1.0E+00
initial expansion factor Hi = 3.0E-02
initial energy density parameters:
    Om_m_i = 0.9000
    Om_phi_i = 0.1000
    Om_Lamb_i = 0.0000

unit scales for this run (adjust by changing H0) :
    t_scale = 4.3E+14 s
    l_scale = 1.3E+23 m
    m_scale = 1.7E+50 kg

scalar potential for this run (from file 'Ratra_Peebles.ini') :
    V(phi) = M**(4+n)/phi**n
    --      n = 2.000E+00 = ( 2 )
    --      M = 5.349E-02 = ( 0.4*(3*H0**2/8/pi)**(1/(4+n))*(8*pi)**(n/(8+n)) )

*Message : using geodesic slicing

*Message : using step-like matter distribution
    - central overdensity, del_m_c = 3.0E-01
    - support size, x_max          = 5.0E+00
    - steepness, k                  = 1.0E+00

*Message : using sym. gaussian phi distribution
    - central overdensity, del_phi_c = 0.0E+00
    - variance, sig_delta            = 2.0E+00

Solving Hamiltonian constraint for conformal factor "psi" ...
...done!
The ajustement of the right boundary (see Shibata) gives C_psi = 1.7E-02

/ 0% |                               |
```

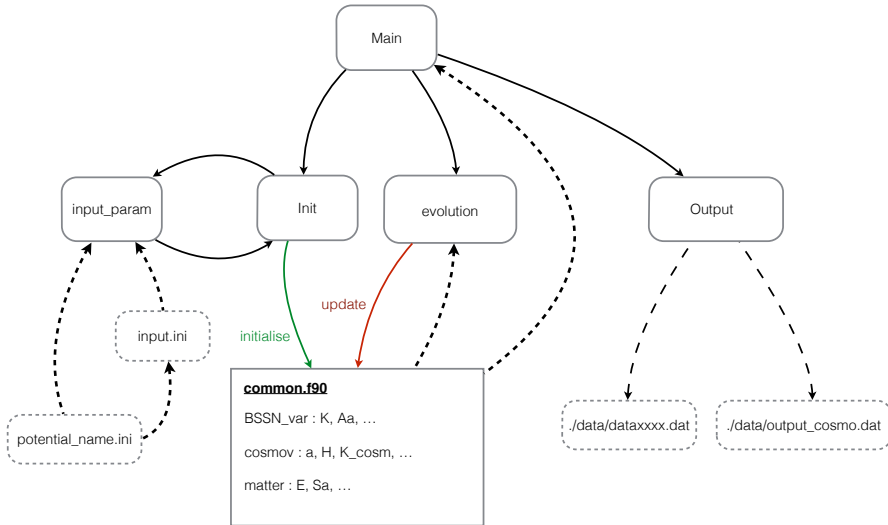


Figure C.1 – A heuristic representation of FORTCosmoSS

## C.4 Directory listing

After building the project consists in the following set of directories

./	main executable, MakeFile and init. files (.ini)
./data/	outputs
./doc/	the code documentation
./licenses/	FORTCosmoSS License file
./scripts/	scripts for output processing
./obj/	object files

## C.5 Simplified project structure

After the first test run is performed, one will want to adapt the code to specific problems. The core structure of the code is shown on Fig. C.1. It revolves around 4 principal modules that are linked together by the main programme.

At initialisation, the programme runs module `init` which calls the procedures contained in module `input_param` to read inputs from predefined files. These are used to initialise the global variables declared in the modules from

file `common.f90`. Module `evolution` is then called to initiate the main loop for the numerical integration of the dynamical equations. At each preset time interval, the programme calls module `output` to produce formatted outputs in directory `./data/`.

## C.6 Running and input parameters

The main programme starts by calling procedure `init_data` from module `init` in file `./src/init.f90`. This computes the initial data after calling procedures from file `./src/input.f90`. This file must contain the declarations of every input parameters in the preamble of its main module `input_param`. Input values are read from file with default name `./input.ini`. This is facilitated by the use of routines from module `IniFile` in file `./src/inifile.f90`. Procedure `read_input` processes the whole input file and produces a buffer list of all that is found in it that has the format

```
label value_1 [ value_2 value_3 ... ]
```

Procedures `assign_real`, `assign_integer` and `assign_str` are then used to scan through the buffer for a given label and to assign the corresponding value(s) to some variable. A typical call reads

```
assign_type(var,array,label)
```

where “`type`” is either “`real`”, “`integer`” or “`str`”, “`var`” and “`array`” are respectively a variable and an allocatable array of the corresponding type and “`label`” is a string corresponding to the label as it appears in the input file. For technical reasons, both `var` and `array` must be provided. In case an input consists in a single value, the size of `array` is set to 0. It must then be deallocated for subsequent use.

The parsing of a scalar potential function can be done by means of an additional use of `read_input`. A dedicated input file must contain all the information regarding the potential in the form of the sample file `Ratra_Peebles.ini`. This includes

- the name of the potential
- its analytical expression
- its first derivative
- its inverse function
- a set of its parameters
- an analytical expression of its parameters

- the complete set of its variables including the above parameters. The first two must always be “V” and “phi”. The code has naturally access to variables “H0”, “Hi” and “pi”.

The analytical expressions provided can then be evaluated within module `potential` (in `./src/potential.f90`) by means of the procedures from module `fparser` (in `./src/fparser.f90`).

The case of the scalar potential can be taken as an example to easily adapt this method of parsing analytical expressions as input to any other case that could be of interest.

The programme prints a summary of the input parameters on start-up and proceeds to initialise all global variables. The BSSN conformal factor is computed by solving the reduced Hamiltonian constraint as a BVP (see Chapter 4).

The programme then initiates the main loop by calling procedure `PIRK` from module `evolution` (in file `./src/evolution.f90`). This implements the numerical integration of the dynamical equations using the second order `PIRK` scheme. The global variables are updated during each call and outputs are generated at a rate specified by the user.

## C.7 Output format

The outputs that consist in simple numbers varying in time are stored into `./data/output_cosmo.dat`. The outputs that consist in time varying arrays are stored into files with names following the pattern `./data/dataxxxx.dat`, where `xxxx` is a 4 digit integer index. Each of these files feature the value of the computational time in its header.

## C.8 Scripts and tools

Folders `./scripts/` is meant to contain all the scripts for output processing. All files provided therein requires `Python` and have been tested with `Python 2.7`. Each file features its own guidelines for proper use which can be accessed by using the command line argument `-h`. The list of these files is given below

<code>compute_redshift.py</code>	rearranges the columns of file containing the cosmological outputs including the scale factor $a$ and the Hubble factor $H$ and adds a column giving the corresponding redshift as a function of time.
<code>plot.py</code>	plots a series of array outputs as a function of another array from a given file.
<code>anim.py</code>	generates a .mp4 film from a collection frames showing the evolution of the spatial profiles of a given series of array outputs from files <code>./data/dataxxxx.dat</code> .

## C.9 Files structure

In this last section, we list the modules and procedures contained within each file from the project. This is followed by Fig. C.2 showing tree of dependencies of the programme and its modules.

```

* main.f90
  |
  - program main
    |
    - subroutine write_output
    |
    - subroutine write_in_log

* common.f90
  |
  - module gauge_choice
    |
    - function f_alpha
    |
  - module matter
  |
  - module BSSN_var
    |
    - subroutine update_derivatives
    |
  - module cosmov
    |
    - subroutine update_cosmov

```

```
    |
    - module metric
      |
      - subroutine update_metric

* constraints.f90
  |
  - module constraints
    |
    - subroutine H_cons
    |
    - subroutine M_cons
    |
    - subroutine L2_norm
    |
    - subroutine H_cons_cosm

* evolution.f90
  |
  - module evolution
    |
    - subroutine PIRK
    |
    - subroutine make_L1_cosmo
    |
    - subroutine make_L2_cosmo
    |
    - subroutine make_L3_cosmo
    |
    - subroutine make_L1
    |
    - subroutine make_L2
    |
    - subroutine make_L3
    |
    - subroutine make_L2bar
    |
    - subroutine make_L3bar

* fparser.f90 (public parts only)
  |
  - module fparser
    |
    - subroutine initf
    |
```

```
    - subroutine parsef
    |
    - subroutine evalf
    |
    - subroutine EvalErrMsg
    |
    - subroutine EvalErrType

* grid.f90
  |
  - module grid

* hydro.f90
  |
  - module hydro
    |
    - subroutine buildlr
    |
    - subroutine hlle
    |
    - subroutine eigenvalue
    |
    - subroutine cons2prim

* inifile.f90
  |
  - module IniFile
    |
    - subroutine read_input
    |
    - subroutine assign_real
    |
    - subroutine assign_integer
    |
    - subroutine assign_str
    |
    - function isthere

* init.f90
  |
  - module init
    |
    - subroutine init_data
    |
    - subroutine fsub
```

```
    |
    - subroutine bcsub

* initial_profiles.f90
  |
  - module initial_profiles
    |
    - function rho_mix
    |
    - function phi_ix
    |
    - function Psi_phiix
    |
    - function V_phi_ix

* input.f90
  |
  - module input_param
    |
    - subroutine input_list
    |
    - subroutine input_potential_list

* math_lib.f90
  |
  - module profiles
    |
    - function logistic
    |
    - function bump
    |
    - function dxbump
    |
    - function sym_gaussian
    |
    - function dxsym_gaussian
    |
  - module root_finding
    |
    - function root
    |
  - module derivatives_fcn
    |
    - function dxf
    |
```

```
- function d2xf
|
- function Delta4_x
|
- function Delta4_x_i
|
- module boundaries
|
- subroutine symmetrise
|
- subroutine anti_symmetrise
|
- subroutine symmetrise_centred
|
- subroutine sommerfeld
|
- module num_integration
|
- function integral
|
- module find_value
|
- subroutine find_closest
|
- module interpolation
|
- subroutine POLINT

* output.f90
|
- module outputs
|
- subroutine output_list
|
- subroutine append_to_list
|
- subroutine print_list
|
- subroutine progress

* potential.f90
|
- module potential
|
- subroutine init_potential
```

```
    |
    - subroutine V_phi
    |
    - function phi_V

* scales.f90
  |
  - module constants

* sources.f90
  |
  - module sources
    |
    - subroutine build_hydro_sources
    |
    - subroutine build_matter_sources
```

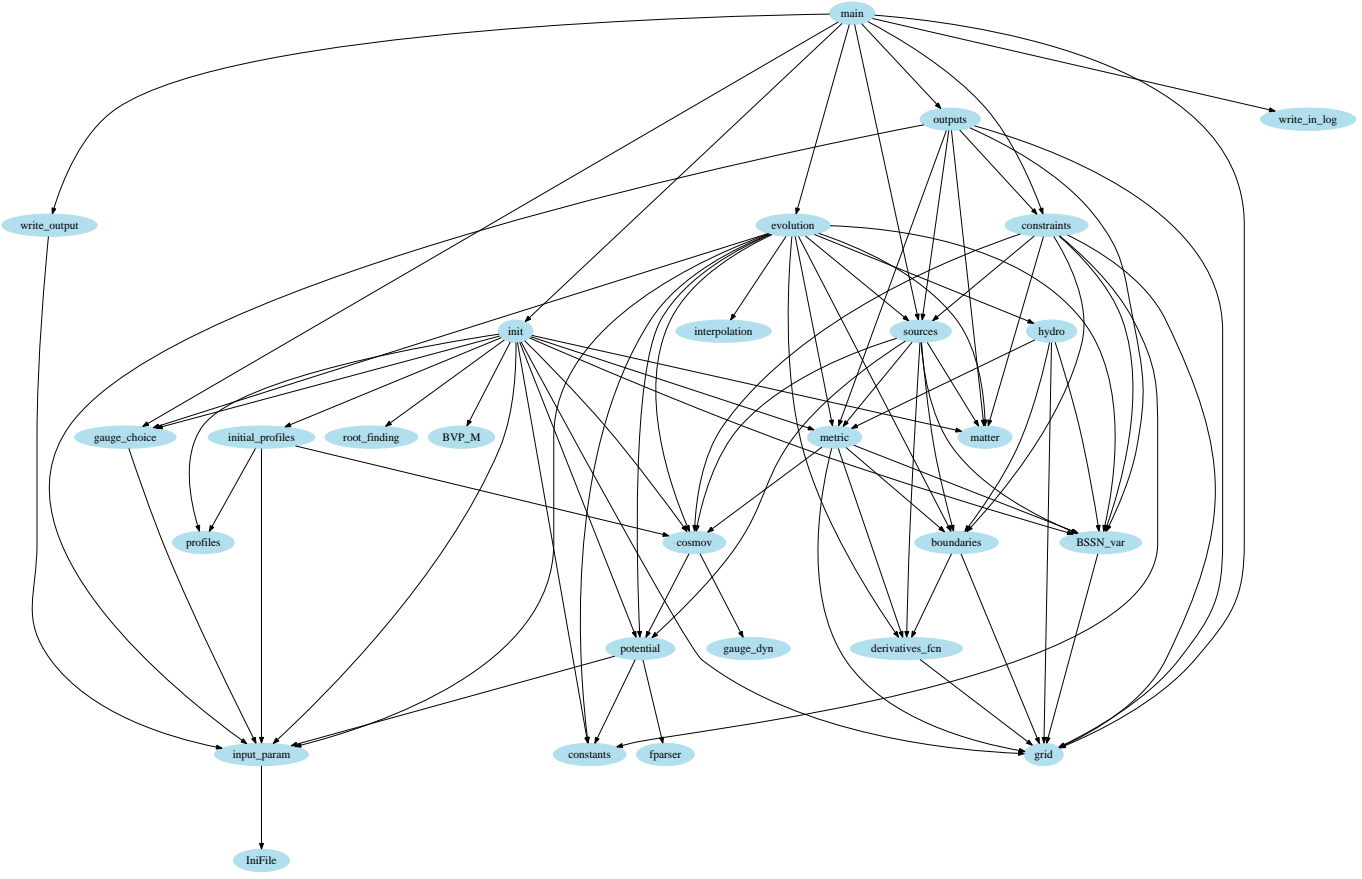


Figure C.2 – Tree of dependencies of the FORTCosmoSS project

# Bibliography

- L. R. Abramo, R. C. Batista, L. Liberato, and R. Rosenfeld. Physical approximations for the nonlinear evolution of perturbations in inhomogeneous dark energy scenarios. *Physical Review D*, **023516**, 1–9, 2009.
- P.A.R. Ade et al. Detection of  $B$ -Mode Polarization at Degree Angular Scales by BICEP2. *Phys. Rev. Lett.*, **112**(24), 241101, 2014a.
- P.A.R. Ade et al. Planck 2013 results. I. Overview of products and scientific results. *Astron.Astrophys.*, **571**, A1, 2014b.
- P.A.R. Ade et al. Planck 2013 results. XV. CMB power spectra and likelihood. *Astron.Astrophys.*, **571**, A15, 2014c.
- P.A.R. Ade et al. Planck 2013 results. XVI. Cosmological parameters. *Astron.Astrophys.*, **571**, A16, 2014d.
- P.A.R. Ade et al. Joint Analysis of BICEP2/*KeckArray* and *Planck* Data. *Phys.Rev.Lett.*, **114**, 101301, 2015.
- M. Alcubierre. *Introduction to 3+1 Numerical Relativity*. International Series of Monographs on Physics. OUP Oxford, 2008.
- M. Alcubierre and M. D. Mendez. Formulations of the 3+1 evolution equations in curvilinear coordinates. *Gen.Rel.Grav.*, **43**, 2769–2806, 2011.
- M. Alcubierre, A. de la Macorra, A. Diez-Tejedor, and J. M. Torres. Cosmological scalar field perturbations can grow. 2015.
- J.-M. Alimi et al. First-ever full observable universe simulation. *in* ‘High Performance Computing, Networking, Storage and Analysis (SC), 2012 International Conference for’, pp. 1–11, Nov 2012.
- L. Amendola and S. Tsujikawa. *Dark Energy: Theory and Observations*. Cambridge University Press, 2010.
- R. Arnowitt, S. Deser, and C W. Misner. The dynamics of general relativity. *in* L. Witten, ed., ‘Gravitation, An Introduction to Current Research’, pp. 227–264. John Wiley, New York, 1962.

- T. W. Baumgarte and S.L. Shapiro. *Numerical Relativity: Solving Einstein's Equations on the Computer*. Cambridge University Press, 2010.
- T. W. Baumgarte and S. L. Shapiro. Numerical integration of einstein's field equations. *Phys. Rev. D*, **59**, 024007, Dec 1998.
- C. L. Bennett et al. First year Wilkinson Microwave Anisotropy Probe (WMAP) observations: Preliminary maps and basic results. *Astrophys.J.Suppl.*, **148**, 1–27, 2003.
- P. Binétruy and G. R. Dvali. D-term inflation. *Phys. Lett.*, **B388**, 241–246, 1996.
- P. Binétruy, G. Dvali, R. Kallosh, and A. Van Proeyen. Fayet-Iliopoulos terms in supergravity and cosmology. *Class. Quant. Grav.*, **21**, 3137–3170, 2004.
- V. R. Bouillot et al. Probing dark energy models with extreme pairwise velocities of galaxy clusters from the DEUS-FUR simulations. *Mon. Not. Roy. Astron. Soc.*, **450**(1), 145–159, 2015.
- P. Brax et al. Moduli corrections to D-term inflation. *JCAP*, **0701**, 026, 2007.
- X. Chen, M.-X. Huang, S. Kachru, and G. Shiu. Observational signatures and non-Gaussianities of general single-field inflation. *Journal of Cosmology and Astroparticle Physics*, **2007**(01), 002–002, January 2007.
- B. Clauwens and R. Jeannerot. D-term inflation after spontaneous symmetry breaking. *JCAP*, **0803**, 016, 2008.
- S. Clesse. Hybrid inflation along waterfall trajectories. *Phys. Rev.*, **D83**, 063518, 2011.
- S Clesse and J Rekier. Updated constraints on large field hybrid inflation. *Phys. Rev. D*, **90**, 083527, Oct 2014.
- S. Clesse and J. Rocher. Avoiding the blue spectrum and the fine-tuning of initial conditions in hybrid inflation. *Phys.Rev.*, **D79**, 103507, 2009.
- I. Cordero-Carrión and P. Cerdá-Durán. Partially implicit runge-kutta methods for wave-like equations. *in* F. Casas and V. Martínez, eds, 'Advances in Differential Equations and Applications', Vol. 4 of *SEMA SIMAI Springer Series*, pp. 267–278. Springer International Publishing, 2014.
- G. D'Amico, M. Kamionkowski, and K. Sigurdson. Dark Matter Astrophysics. *ArXiv e-prints*, July 2009.
- S. C. Davis and M. Postma. Successfully combining SUGRA hybrid inflation and moduli stabilisation. *JCAP*, **0804**, 022, 2008.

- W. de Sitter. On the relativity of inertia. Remarks concerning Einstein's latest hypothesis. *Koninklijke Akademie van Wetenschappen. Section of Science*, **19**, 1217–1224, 1917.
- S. Dodelson. *Modern Cosmology*. Academic Press. Academic Press, 2003. ISBN: 9780122191411.
- A. Einstein. Cosmological Considerations in the General Theory of Relativity. *Sitzungsber. Preuss. Akad. Wiss. Berlin (Math. Phys.)*, pp. 142–152, 1917.
- G. F. R. Ellis and H. van Elst. Cosmological models (Cargèse lectures 1998). p. 87, December 1998.
- M. Fairbairn, Laura Lopez Honorez, and M. H. G. Tytgat. Radion assisted gauge inflation. *Phys. Rev.*, **D67**, 101302, 2003.
- R. a. a. Fernandes, J. P. M. de Carvalho, a. Yu. Kamenshchik, U. Moschella, and a. da Silva. Spherical “top-hat” collapse in general-Chaplygin-gas-dominated universes. *Physical Review D*, **85**(8), 083501, April 2012.
- A. Friedmann. Über die Krümmung des Raumes. *Zeitschrift für Physik*, **10**, 377–386, 1922.
- J. A. Frieman, C. T. Hill, A. Stebbins, and I. Waga. Cosmology with ultralight pseudo Nambu-Goldstone bosons. *Phys. Rev. Lett.*, **75**, 2077–2080, 1995.
- T. Fukuyama, N. Okada, and T. Osaka. Realistic Hybrid Inflation in 5D Orbifold SO(10) GUT. *JCAP*, **0809**, 024, 2008.
- D. S. Goldwirth and T. Piran. Spherical inhomogeneous cosmologies and inflation: Numerical methods. *Phys. Rev. D*, **40**, 3263–3279, Nov 1989.
- É.ourgoulhon. *3+1 Formalism in General Relativity: Bases of Numerical Relativity*. Lecture Notes in Physics. Springer, 2012.
- J. E. Gunn and J. R. Gott, III. On the Infall of Matter Into Clusters of Galaxies and Some Effects on Their Evolution. *Apj.*, **176**, 1, August 1972.
- E. Halyo. Hybrid inflation from supergravity D-terms. *Phys. Lett.*, **B387**, 43–47, 1996.
- D. W. Hogg. Distance measures in cosmology. 1999.
- C. Horellou and J. Berge. Dark energy and the evolution of spherical overdensities. *Monthly Notices of the Royal Astronomical Society*, **360**(4), 1393–1400, July 2005.
- E. Hubble. A Relation between Distance and Radial Velocity among Extra-Galactic Nebulae. *Proceedings of the National Academy of Science*, **15**, 168–173, March 1929.

- E. P. Hubble. Extragalactic nebulae. *ApJ.*, **64**, 321–369, December 1926.
- J. C. Hwang and H. Noh. Quintessential perturbations during scaling regime. *Phys. Rev. D*, **64**(103509), 2001.
- J. M Ibáñez, M.-A. Aloy, J. A. Font, J. M Martí, J. A. Miralles, and J. A. Pons. Riemann solvers in general relativistic hydrodynamics. *in* E. Toro, ed., ‘Proceedings of an International Conference on Godunov Methods: Theory and Applications, Held October 18-22, 1999, in Oxford, UK’, pp. 485–496. Kluwer Academic/Plenum Publishers, New York, 2001.
- R. Jeannerot, J. Rocher, and M. Sakellariadou. How generic is cosmic string formation in SUSY GUTs. *Phys. Rev.*, **D68**, 103514, 2003.
- R. Kallosh and A. Linde. P-term, D-term and F-term inflation. *JCAP*, **0310**, 008, 2003.
- M. Kamionkowski, A. Kosowsky, and A. Stebbins. A Probe of primordial gravity waves and vorticity. *Phys.Rev.Lett.*, **78**, 2058–2061, 1997.
- L. D. Landau and E. M. Lifshitz. *Fluid Mechanics, Second Edition*. Course of theoretical physics / by L. D. Landau and E. M. Lifshitz, Vol. 6. Butterworth-Heinemann, 2 edn, January 1987.
- P. D. Lasky and A. W.C. Lun. Generalized Lemaitre-Tolman-Bondi Solutions with Pressure. *Phys.Rev.*, **D74**, 084013, 2006.
- P. D. Lasky and A. W.C. Lun. Spherically Symmetric Gravitational Collapse of General Fluids. *Phys.Rev.*, **D75**, 024031, 2007.
- G. Lazarides and A. Vamvasakis. New smooth hybrid inflation. *Phys. Rev.*, **D76**, 083507, 2007.
- G. Lemaître. Un Univers homogène de masse constante et de rayon croissant rendant compte de la vitesse radiale des nébuleuses extra-galactiques. *Annales de la Société Scientifique de Bruxelles*, **47**, 49–59, 1927.
- Antony Lewis and Sarah Bridle. Cosmological parameters from cmb and other data: a monte- carlo approach. *Phys. Rev.*, **D66**, 103511, 2002.
- W. Li and L. Xu. Spherical top-hat Collapse of a Viscous Unified Dark Fluid. *Eur. Phys. J.*, **C74**, 2870, 2014.
- C. Llinares and D. F. Mota. Releasing scalar fields: cosmological simulations of scalar-tensor theories for gravity beyond the static approximation. *Phys.Rev.Lett.*, **110**(16), 161101, 2013.
- J. Maldacena. Non-gaussian features of primordial fluctuations in single field inflationary models. *Journal of High Energy Physics*, **2003**(05), 013–013, May 2003.

- J. Martin and C. Ringeval. First CMB constraints on the inflationary reheating temperature. *Phys. Rev. D.*, **82**(2), 023511, July 2010.
- J. Martin, C. Ringeval, and V. Vennin. *Encyclopaedia Inflationaris*. 2013.
- J. Martin, C. Ringeval, R. Trotta, and V. Vennin. The Best Inflationary Models After Planck. *JCAP*, **1403**, 039, 2014.
- J. C. Mather et al. Measurement of the cosmic microwave background spectrum by the COBE FIRAS instrument. *ApJ.*, **420**, 439–444, January 1994.
- P. J. Montero and I. Cordero-Carrión. BSSN equations in spherical coordinates without regularization: vacuum and non-vacuum spherically symmetric spacetimes. *Phys.Rev.*, **D85**, 124037, 2012.
- D.F. Mota and C. van de Bruck. On the Spherical collapse model in dark energy cosmologies. *Astron.Astrophys.*, **421**, 71–81, 2004.
- V. Mukhanov and S. Winitzki. *Introduction to Quantum Effects in Gravity*. Cambridge University Press, 2007.
- T. Nakamura, K. Oohara, and Y. Kojima. General relativistic collapse to black holes and gravitational waves from black holes. *Prog. Theor. Phys. Suppl.*, **90**, 1, 1987.
- NASA will the universe expand forever? [http://map.gsfc.nasa.gov/universe/uni\\_shape.html](http://map.gsfc.nasa.gov/universe/uni_shape.html). Accessed: 2015-04-28.
- N. J. Nunes and D. F. Mota. Structure formation in inhomogeneous dark energy models. *Mon. Not. Roy. Astron. Soc.*, **368**, 751–758, 2006.
- T. Padmanabhan. *Structure Formation in the Universe*. Cambridge University Press, 1993.
- J.A. Peacock. *Cosmological Physics*. Cambridge Astrophysics. Cambridge University Press, 1999.
- P. J. E. Peebles. *The Large-scale Structure of the Universe*. Princeton series in physics. Princeton University Press, 1980.
- P. J. E. Peebles and Bharat Ratra. The Cosmological constant and dark energy. *Rev. Mod. Phys.*, **75**, 559–606, 2003.
- S. Perlmutter and Supernova Cosmology Project. Measurements of Omega and Lambda from 42 High-Redshift Supernovae. *Apj.*, **517**, 565–586, June 1999.
- T. Piran. NUMERICAL RELATIVITY FROM GRAVITATIONAL RADIATION TO COSMOLOGY. in ‘11th International Conference on General Relativity and Gravitation Stockholm, Sweden, July 6-11, 1986’, 1986.

- E. Poisson. *An advanced course in general relativity*. University of Guelph, draft edn, 2002.
- J. Requier, I. Cordero-Carrión, and A. Füzfa. Fully relativistic non-linear cosmological evolution in spherical symmetry using the bssn formalism. *Phys. Rev. D*, **91**, 024025, Jan 2015.
- L. Rezzolla and O. Zanotti. *Relativistic Hydrodynamics*. OUP Oxford, 2013.
- A. G. Riess, B. P. Schmidt, et al. Observational Evidence from Supernovae for an Accelerating Universe and a Cosmological Constant. *The Astronomical Journal*, **116**(3), 1009–1038, September 1998.
- J. Rocher and M. Sakellariadou. Supersymmetric grand unified theories and cosmology. *JCAP*, **0503**, 004, 2005.
- U. Seljak and M. Zaldarriaga. Signature of gravity waves in polarization of the microwave background. *Phys.Rev.Lett.*, **78**, 2054–2057, 1997.
- S. Serjeant. *Observational Cosmology*. The open university. Cambridge University Press, 2010.
- M. Shibata and M. Sasaki. Black hole formation in the Friedmann universe: Formulation and computation in numerical relativity. *Phys. Rev.*, **D60**, 084002, 1999a.
- M. Shibata and M. Sasaki. Black hole formation in the friedmann universe: Formulation and computation in numerical relativity. *Phys. Rev. D*, **60**, 084002, Sep 1999b.
- T. Shibata, M. and Nakamura. Evolution of three-dimensional gravitational waves: Harmonic slicing case. *Phys. Rev. D*, **52**, 5428–5444, Nov 1995.
- V. Springel et al. Simulations of the formation, evolution and clustering of galaxies and quasars. *Nature*, **435**, 629–636, June 2005.
- J. M. Torres, M. Alcubierre, A. Diez-Tejedor, and D. Núñez. Cosmological nonlinear structure formation in full general relativity. *Phys. Rev. D*, **90**, 123002, Dec 2014.
- F. H. Vincent, T. Paumard, E. Gourgoulhon, and G. Perrin. Gyoto: a new general relativistic ray-tracing code. *Classical Quantum Gravity*, **28**(22), 225011, 2011.
- G. M. Voit. Tracing cosmic evolution with clusters of galaxies. *Rev. Mod. Phys.*, **77**, 207–258, 2005.
- L.-M. Wang and P. J. Steinhardt. Cluster abundance constraints on quintessence models. *Astrophys. J.*, **508**, 483–490, 1998.

- S. Weinberg. *Cosmology*. Cosmology. OUP Oxford, 2008.
- C. M. Will. The Confrontation between General Relativity and Experiment. *Living Reviews in Relativity*, **17**, 2014.
- N. Wintergerst and V. Pettorino. Clarifying spherical collapse in coupled dark energy cosmologies. *Phys. Rev.*, **D82**, 103516, 2010.